NUMERICAL SIMULATION OF WATER-COOLED SAMPLE HOLDERS FOR HIGH-HEAT FLUX TESTING OF LOW-LEVEL IRRADIATED MATERIALS

A Dissertation
Presented to
The Academic Faculty

By

Carlos H. Charry León

In Partial Fulfillment
Of the Requirements for the Degree
Master of Science in the
G. W. Woodruff School of Mechanical Engineering

Georgia Institute of Technology

December, 2014

NUMERICAL SIMULATION OF WATER-COOLED SAMPLE HOLDERS FOR HIGH-HEAT FLUX TESTING OF LOW-LEVEL IRRADIATED MATERIALS

Approved By:

Dr. Said I. Abdel-Khalik, Co-Advisor
School of Mechanical Engineering
Georgia Institute of Technology

Dr. Minami Yoda, Co-Advisor
School of Mechanical Engineering
Georgia Institute of Technology

Dr. S. Mostafa Ghiaasiaan
School of Mechanical Engineering
Georgia Institute of Technology

Date Approved: December 3, 2014

ACKNOWLEDGEMENTS

I would like to thank my advisors Dr. Abdel-Khalik and Dr. Yoda for their guidance and support through this process. It has been an honor to be under the leadership of such brilliant scholars. Working with their research group has caused me to grow tremendously as an engineer and human. Their pursuit of excellence and knowledge are forever imprinted on my mind. I thank you both for inspiring me not to be conformed and giving my best. Also, I would like to thank Dr. Ghiaasiaan, his feedback and contributions were very beneficial to the completion of my thesis.

Additionally, I would like to thank my colleagues Bailey Zhao and Dr. Brantley Mills. Bailey was fundamental in the redaction and completion of my thesis by providing me with insightful feedback and knowledge throughout the whole process. Dr. Mills was essential throughout the development and consolidation of my research, his expertise proved to be an invaluable well of knowledge in the understanding of complex concepts. I would also like to thank my other colleagues: Ahmad Khayyat, Sterling Olson, Hannah Oermann, Vincent Nasri, and Christopher Fernandez. I will always treasure your friendship and help throughout this work.

Finally, I would like to thank my beautiful family who has consistently supported me throughout this whole process. My mother, Flor, my father, Humberto, my brother, Emerson, and my wife, Sheila, have always believed in me, and I would not be where I am today without them. I love you all dearly. My final thanks are to God, for He is my source of strength and encouragement daily. Thank God for the many blessings and for enabling me to worship you through my work.

TABLE OF CONTENTS

LIST OF TABLES

LIST OF FIGURES

NOMENCLATURE

Variable	Definition	Units
V_n	Nozzle velocity	m/s
$V_{j,s}$	Impingement surface velocity	m/s
V_j	Jet velocity at the nozzle exit	m/s
h	Convection heat transfer coefficient	$W/m^2 \cdot K$
ζ_{max}	Radius of the largest active sites	m
q''_{ONB}	Heat flux related to the onset of significant boiling	W/m^2
$T_{w_{ONB}}$	Wall temperature related to the onset of significant boiling	W/m^2
ΔT_{sat}	Wall superheat	K
T_{sat}	Saturation temperature	K
q''_{FNB}	Heat flux for the fully developed nucleate boiling	W/m^2
q''_{CHF}	Critical heat flux	W/m^2
$q''_{CHF_{pool}}$	Critical heat flux for pool boiling	W/m^2
ε_{sub}	Correction factor for the effect of sub-cooling	-
σ	Surface tension	N/m
P_s	Stagnation Pressure	Pa
P_∞	Pressure in the test section	Pa
α	Phase volume fraction	-
q	A given phase (i.e. liquid, vapor)	-
ρ	Density	kg/m^3
$\vec{v}$	Velocity vector	m/s
$\dot{m}$	Volumetric mass exchange rate	kg/s
h_{ls}	Liquid side interfacial heat transfer coefficient	W/m^2

h_{vs}	Vapor side interfacial heat transfer coefficient	W/m^2·K
$q_E^{''}$	Evaporative heat flux	W/m^2
H	Latent heat per unit mass	J/kg
A_w	Interfacial area density	m^2
d_v	Diameter of the vapor bubble	mm
$\bar{\bar{\tau}}_q$	Shear stress	Pa
$\vec{R}$	Interfacial drag force	N
$\vec{F}_q$	Turbulent diffusion rate for phase q	N
$\vec{F}_{lift,q}$	Lift force	N
P	Pressure	Pa
$\vec{g}$	Gravitational acceleration vector	m/s^2
C_d	Drag coefficient	-
C_d^{dis}	Distorded drag coefficient	-
C_d^{vis}	Viscous drag coefficient	-
Re	Reynolds number	-
Re_b	Bubble Reynolds number	-
Re_v	Bubble shear Reynolds number	-
C_{TD}	Turbulent dispersion coefficient	-
$\vec{q}$	Heat flux vector	W/m^2
S	Source term	-
Q	Energy exchange between the different phases	J
h_{pq}^o	Formation enthalpies of phases p and q	J/kg
T_{sol}^{cell}	Solid cell temperature	K
$q_l^{"}$	Liquid convective heat flux	W/m^2
$q_Q^{"}$	Quenching heat flux	W/m^2

Ω	Area of influence	m^2
T_w	Wall temperature	K
T_l	Liquid temperature	K
k	Thermal Conductivity	W/m·K
T	Periodic time	s
λ_l	Thermal diffusivity	m^2/s
V_d	Volume of bubble	m^3
N_w	Nucleation site density	m^{-3}
ρ_v	Vapor density	kg/m^3
U_b	Near wall bulk velocity	m/s
ΔT_{sub}	Sub-cooling temperature differential	K
k_i	Turbulent kinetic energy	-
ε	Dissipation rate	-
μ	Viscosity	P·s
G	Turbulence production rate	-
S_k	Bubble induced turbulence	-
$C_{\varepsilon 1}$	1st Constant for dissipation rate equation	-
$C_{\varepsilon 2}$	2nd Constant for dissipation rate equation	-
$C_{\varepsilon 3}$	3rd Constant for dissipation rate equation	-
S_ε	Bubble induced dissipation	-

SUMMARY

The promise of a vast source of energy to power the world and protect our planet using fusion technology has been the driving force for scientists and engineers around the globe for more than sixty years. Although the materialization of this ideal still in the distance, multiple scientific and technological advances have been accomplished, which have brought commercial fusion power closer to a reality than it has ever been. As part of the collaborative effort in the pursuit of realizable fusion energy, the International Thermonuclear Experimental Reactor (ITER) is being developed by a coalition of nations of which the United States is a part of. One critical technological challenge for ITER is the development of adequate plasma facing materials (PFMs) that can withstand the strenuous conditions of operation. To date, high heat flux (HHF) testing has been conducted mainly on non-irradiated specimens due to the difficulty of working with radioactive specimens, such as instrument contamination. In this thesis, the new Irradiated Material Target Station (IMTS) facility for fusion materials at Oak Ridge National Laboratory (ORNL), in which the HHFs are provided by water-wall plasma-arc lamps (PALs), is considered for neutron-irradiated specimens, especially tungsten. The facility is being used to test irradiated plasma-facing components materials for magnetic fusion reactors as part of the US-Japan plasma facing components evaluation by tritium plasma, heat and neutron irradiation experiments (PHENIX). In order to conduct HHF testing on the PFMs various sample holders designs were developed to accommodate radioactive specimens during HHF testing.

As part of the effort to design sample holders that are compatible with the IMTS facility, numerical simulations were performed for different water-cooled sample holder

designs with the commercial computational fluid dynamics (CFD) software package, ANSYS™ FLUENT®. The numerical models are validated against experimental temperature measurements obtained from the IMTS facility. These experimentally validated numerical models are used to assess the thermal performance of two sample holder designs and establish safe limits for HHF testing under various operating conditions. The limiting parameter for the current configuration was determined for each sample holder design. For the Gen 1 sample holder, the maximum temperature reached within the Copper rod limits the allowable incident heat flux to about 6 MW/m^2. In the case of the Gen 2 sample holder, the maximum temperature reached within the Molybdenum clamping disk limits the allowable incident heat flux to about 5 MW/m^2.

In addition, the numerical model are used to parametrically investigate the effect of the operating pressure, mass flow rate, and incident heat flux on the local heat flux distributions and peak surface temperatures. Finally, a comparative analysis is conducted to evaluate the advantages and disadvantages associated with the main design modifications between the two sample holder models as to evaluate their impact in the overall thermal performance of each sample holder in order to provide conclusive recommendations for future sample holder designs.

CHAPTER 1: INTRODUCTION

1.1 Introduction and Motivation

The world's demand for energy is continuously rising, calling for major advances in energy technology to meet the challenges that accompany such growth. The greatest increase in the demand for energy this century is envisaged to come from developing countries where rapid urbanization and large-scale electricity generation will be required. With environmental requirements for zero or low CO_2 emission sources and the need to invest in a sustainable energy infrastructure, new energy sources must be developed. Analysts are expecting a complete shift of the global energy system in the 21st century, by moving away from fossil fuels towards either renewable sources or new nuclear technologies [1]. The rationale behind the shift include: resource depletion and environmental concerns, with a major emphasis on global warming and unacceptable geo-political frictions. Fusion is hoped to become a corner stone of the future energy system. The construction and successful operation of the International Thermonuclear Experimental Reactor (ITER) is a critical milestone in reaching this goal. In the words of Osamu Motojima, the director general of ITER; "The use of fusion energy is a 'must' if we are serious about embarking on sustainable development for future generations." [2]

1.1.1 Magnetic Confinement Fusion Energy

Fusion is the process that powers the sun and the stars. In a fusion reaction, two light nuclear particles combine or "fuse" together, resulting in a product nuclei with less mass than the original particles. This mass difference is converted into energy as given by Einstein's mass-energy equivalence formula: $E = \Delta mc^2$. The possibility of releasing large

amounts of nuclear energy can be seen when comparing the masses of the nuclei of low atomic number. The most promising reaction makes use of the isotope deuterium (D) reacting with tritium (T). The D-T reaction yields a helium ion and a neutron with energies as indicated:

$$ {}_{1}^{2}D + {}_{1}^{3}T \rightarrow {}_{2}^{4}He(3.5MeV) + {}_{0}^{1}n(14.1MeV) \quad (1) $$

The cross section is large and the energy yield is favorable. The ideal ignition temperature for the D-T reaction is only 4.4 keV in contrast with the 48 keV for the D-D reaction, making the achievement of practical fusion with the former case far easier. In addition, deuterium is present in hydrogen, as in water, with an abundance of only 0.015%, but due to our planet having vast amounts of water, the fuel available is almost inexhaustible. One drawback, however, is that the artificial isotope tritium is required. Tritium can be generated by neutron absorption in lithium. The neutron can come from the D-T fusion process itself coupled with a breeding cycle similar to that in fission reactors.

The D-T reaction described does not occur by merely mixing the ingredients, because of the strong force of electrostatic repulsion between the charged nuclei. Only by providing a high amount of kinetic energy to one or both of the particles can they both be brought close enough to each other for the strong force to dominate the electrical force. The medium in which high particle energies are obtained is known as plasma. The plasma is often called “the fourth state of matter” and can be achieved through the injection of enough external energy to heat the atoms to temperatures exceeding 10^7 K, forming a highly ionized gas containing an equal number of electrons and positively charged ions, making the medium electrically neutral [3]. Progress towards practical fusion can be measured by the ratio of energy output to energy input. To attain a net positive energy

balance, the plasma must be confined at a high density such that the fusion reaction occurs at a high enough rate yielding net power. The two most promising plasma confinement methods are laser inertial confinement and magnetic confinement. Laser inertial confinement uses inertial forces to compress and heat the fuel target. Energy is delivered to the outer layer of the target using high-energy beams of laser light, resulting in the implosion of the fuel microcapsule so that a fusion reaction occurs. Though a favored technique at first, the high laser power input requirement has impeded its progress. As a result, the present leading plasma confinement technology is magnetic confinement. In magnetic confinement, the plasma is contained away from the walls by exploiting its properties. Like iron filings in the presence of a magnet, charged particles in the plasma will follow magnetic field lines. Thus, the plasma can be shaped and confined by the magnetic forces [2].

The "Tokamak" design shown in Figure 1 is the most advanced magnetic confinement system, in which the plasma is contained in a doughnut-shaped vacuum vessel. The magnetic confinement method has been chosen for ITER, the 500 MW experimental fusion reactor currently under construction in Cadarache, France, which is expected to be ready for operation in November 2020. The Tokamak design is also planned to be used for DEMO, the proposed fusion power plant that will follow ITER's expected success. One critical technological challenge for ITER is the development of adequate plasma facing materials (PFMs) that can withstand the strenuous conditions of operation.

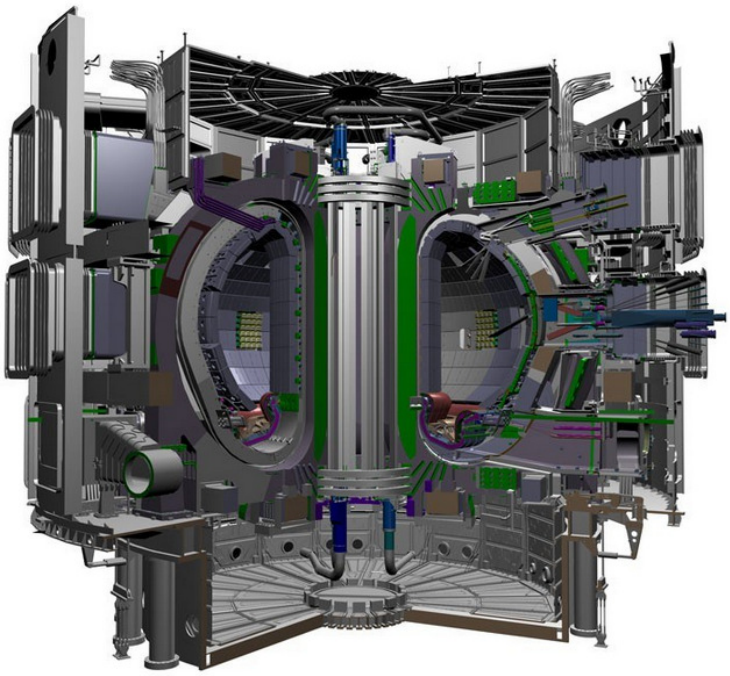

Figure 1. An example of a Tokamak fusion reactor design, ITER. [2]

1.1.2 Plasma Facing Materials and Components

Developing plasma facing materials (PFMs) is a key challenge to the realization of the steady state high power fusion that will be required in DEMO and future fusion power plants. The ITER design uses PFMs selected for their suitability to regions of the vacuum vessel with different power and particle loading characteristics. During operation, these materials are exposed to high heat fluxes; therefore, it is fundamental to perform high heat flux tests for R&D of ITER components. Specifically, the ITER blanket, first wall, and the divertor are some of the most critical and technically challenging components of ITER, since they directly face the hot plasma. Figure 2 shows the poloidal cross section of ITER. The ITER design employs beryllium, carbon fiber reinforced composites and tungsten as PFMs. Beryllium (Be) is the prime candidate material for the first wall, which covers the interior surfaces of the vacuum vessel, providing shielding to the vessel and the

superconducting magnets from the heat and neutron fluxes of the fusion reaction. Beryllium has been selected as the armor of the first wall since it is a low Z material making it less harmful to the fusion plasma and a good oxygen getter [4]. Tungsten (W) is the preferred material for the divertor, except for the area near the strike points where carbon fiber reinforced composites (CFCs) are to be used. The divertor is one of the key components of the ITER machine. Situated along the bottom of the vacuum vessel, its function is to extract heat and helium ash, both products of the fusion reaction, including other impurities from the plasma, overall acting similar to a giant exhaust system [2]. Tungsten has advantages because of its high melting point, longer lifetime and low erosion rate under high flux hydrogen isotope bombardment in the divertor. CFCs are advantageous primarily due to their good thermal and mechanical properties, resistance to melting at high temperatures, and low atomic number. Nevertheless, one of the most serious concerns about using CFCs is their chemical affinity to hydrogen isotopes, especially tritium (referred to as chemical erosion). Initially, ITER had planned to begin operations with a divertor target made of CFC to be followed by a second divertor with W targets. Currently, due to cost cutting considerations, the ITER management is investigating the feasibility of implementing tungsten from start of operations [2].

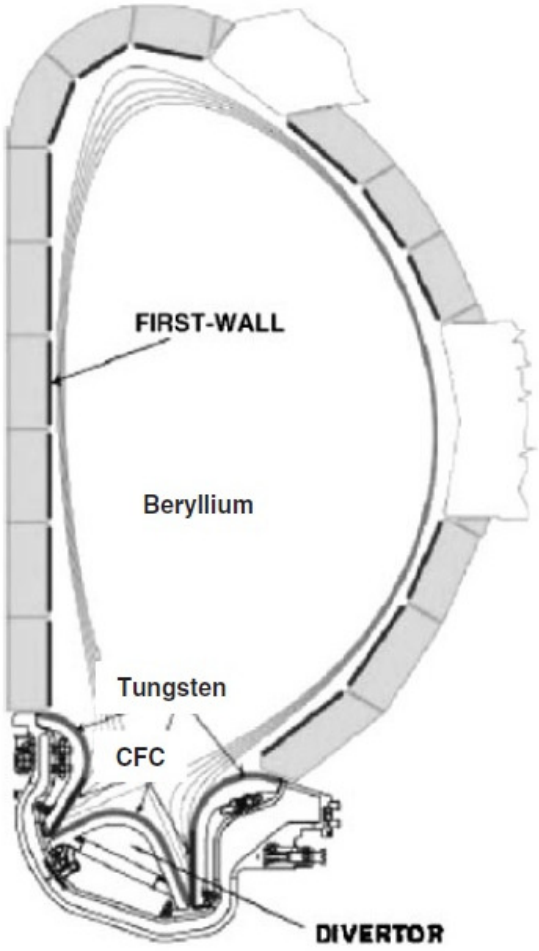

Figure 2. Poloidal cross section showing the layout of PFCs in ITER with different armor materials. [4]

1.1.3 Irradiated Material Target Station Facility

Design studies for ITER are based on the technical feasibilities of PFCs that can guarantee a reasonable lifetime from a safety and economical points of view. This lifetime is limited mainly by thermal loads and by thermally induced mechanical stresses to these components. Here, the thermal fatigue during the cyclic plasma operation at a power density of 5 to 20 MW/m^2 for the divertor targets (~0,5 MW/m^2 for the first wall) are a serious concern, specifically for intermittently operating Tokamak devices [4]. Thus, it is essential to study the performances of materials and components under these conditions.

The simulation of ITER-relevant high heat fluxes (HHFs) have been conducted using a number of different types of heat sources, e.g. electron beam facilities, particle beam facilities, IR heaters, and plasma guns. Each source has different specifications, which are associated with the advantages and disadvantages. To date, high heat flux testing (HHFT) has been conducted mainly on non-irradiated specimens due to the difficulty of working with radioactive specimens, such as instrument contamination. In this thesis, the new Irradiated Material Target Station (IMTS) facility for fusion materials at Oak Ridge National Laboratory (ORNL), in which the HHFs are provided by water-wall plasma-arc lamps (PALs), is considered for neutron-irradiated specimens, especially tungsten. The facility is being used to test irradiated plasma-facing components materials for magnetic fusion reactors as part of the US-Japan plasma facing components evaluation by tritium plasma, heat and neutron irradiation experiments (PHENIX). Two PALs currently available at ORNL provide fusion-prototypical steady state heat flux conditions; one produces a maximum incident heat flux of 27 MW/m^2 over a heated area of 1 × 10 cm^2; the other produces 4.2 MW/m^2 over an area up to 9×12 cm^2. Currently, the duration of the HHFT is limited to 30 seconds by the electrode and reflector coolant; however, with the additional in-progress expansion, the duration of HHFT will be increased to 450 seconds [SABAU-2014]. In addition to the heat source, the IMTS facility consists of a test section and test chamber. The test section is a coupled configuration of a molybdenum sample holder attached to a water-cooled Copper rod. The test chamber has been designed to accommodate large samples required for the high heat flux prototype component testing anticipated in the fusion program. Components of the test chamber were designed to take into account both radiation safety and materials compatibility requirements, to allow the

testing of low level irradiated tungsten articles. Table 1 shows a summary of design considerations and solutions adopted for handling irradiated materials.

Table 1. Design considerations and solutions adopted for IMTS facility [5].

Design Considerations	Adopted Solutions
IR heating	Large quartz window
Quartz window seal	High temperature o-ring
Enclosure overheating	• Enclosure size larger than peak power • Water cooled enclosure
W testing: No O_2 at high temperature	Evacuate enclosure air and backfill with Ar
Quartz window integrity during air evacuation	Secondary chamber on top of quartz window for equalizing pressure on both sides of quartz window
Liftoff of quartz window	Vent and automatic pressure valve and controller
Avoid overheating and cracking of quartz during HHF	Air knife to cool the quartz window
HHF	Impingement water cooling
Temperature measurements	K, S, R thermocouples; pyrometer
Containment of volatilized radioactive compounds	1 HEPA filter vent for Ar bleeding during experiment 1 HEPA filter canister for evacuation of Ar after experiment 2 Testing section enclosed in quartz cylinder 3 Vacuum tight thermocouples feedthroughs 4 No water connections within enclosure

Test sections were assembled and proof-of-principle HHFT was conducted, demonstrating the readiness of the new facility. The HHFT facility using PALs demonstrated, with W samples, the advantages of continuous as well as pulsed uniform heating over a significant sample area. The irradiated samples are mounted on molybdenum sample holders attached to a water-cooled cooper rod. A variety of sample

holders and copper rod configurations have recently been fabricated and tested for different sample sizes and geometries. Trial runs conducted at ORNL demonstrated that the new facility is appropriate for the HHFT of tungsten and other materials intended for use in fusion systems, especially for divertor and other high-heat load applications. The facility is capable of working with low activity radioactive specimens and/or mock-up components to relevant ITER/DEMO exposure times [5]. Future efforts will be dedicated to assessing the effect of HHF exposures of neutron irradiated tungsten.

1.1.4 Objectives

This Masters thesis aims to numerically characterize the heat flux limits for safe operation of the IMTS facility during testing and to analyze the thermal performance of various water-cooled sample holders for future design configurations. A significant concern in water-cooled devices is departure from nucleate boiling exceeding the burnout limit for sub-cooled or saturated flow boiling conditions.

As part of the effort to design sample holders that are compatible with the IMTS facility, numerical simulations were performed for different water-cooled sample holder designs with the commercial computational fluid dynamics (CFD) software package, ANSYS™ FLUENT®. The numerical models are validated against experimental temperature measurements obtained from the IMTS facility. These experimentally validated numerical models were used to parametrically investigate the effect of the operating pressure, coolant mass flow rate, incident heat flux, and length of irradiation periods on the local heat flux distributions and peak surface temperatures. The results from these parametric analyses were then used to estimate the range of operating conditions appropriate for the different sample holders.

CHAPTER 2: LITERATURE REVIEW

This chapter reviews heat transfer concepts, numerical models, and experimental work relevant to the characterization of the sample holder designs considered in this thesis. The discussion begins with an in depth review of previous research conducted on jet impingement cooling and the basic criteria used to evaluate their thermal performance. The main goal is to provide basic understanding of the mechanisms involved in jet impingement cooling and the effects of geometry, specifically for a sub-cooled, confined-circular water jet impinging on a flat and concave heated surfaces. This discussion is followed by a review of previous research conducted on numerical modeling of two-phase flow, specifically the implementation of the Rensselaer Polytechnic Institute (RPI) model, within the context of the Eulerian multiphase model, for wall boiling characterization.

2.1 Jet Impingement Cooling

In the sample holder designs examined in this thesis, the primary cooling mechanism is a turbulent circular jet of sub-cooled water flowing upwards and impinging upon the underside of a concave heated surface. Although the application studied here involves jet impingement on a concave surface, there are far more studies of impingement upon a flat surface. Therefore, this section reviews the hydrodynamics characteristics of both confined and submerged jets impinging and stagnating on a flat plate.

2.1.1 Jet impingement hydrodynamics

This review focuses on two liquid jet configurations with continuous cross sections; confined jets and submerged jets. A schematic for these configurations is shown in Figure 3.

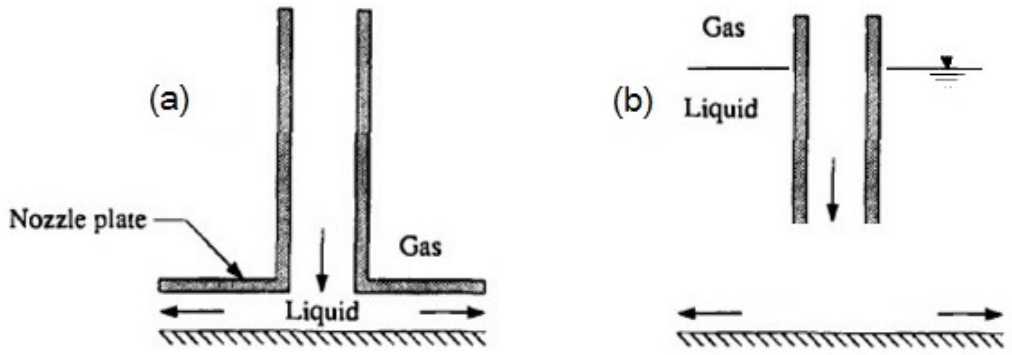

Figure 3. Schematic of (a) confined and (b) submerged jet configurations [6]

In the confined jet, the liquid travels into a region bounded by the impingement surface and nozzle plate, with a stagnation point occurring on the surface at the jet centerline. In submerged jets, the liquid is injected instead into a stagnant pool of fluid, and impinges upon a surface some distance away from the jet exit. According to Miyazaki and Siberman [8], for an impinging jet, the pressure is a maximum at the stagnation point and it reaches the ambient pressure with increasing distance. Conversely, the velocity is zero at the stagnation point and it increases to the velocity of the jet with increasing distance along the surface. As shown in Figure 4, the flow along the impingement surface can be divided into the stagnation, acceleration, and parallel-flow regions.

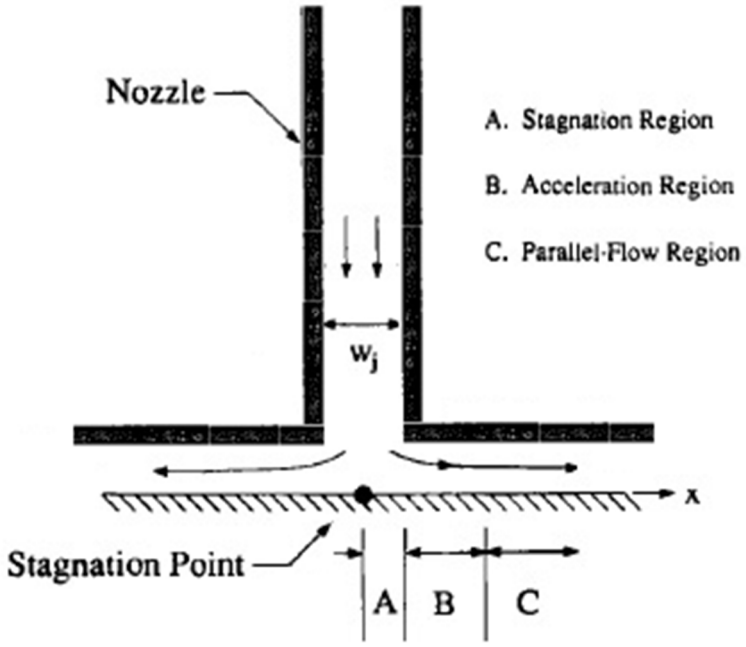

Figure 4. Demarcation of flow regions for a confined jet [6]

The stagnation region is essentially where the jet impinges on the surface with the velocity increasing nearly linearly from the stagnation point in the center. In the acceleration region, the velocity of the fluid continues to increase to a value close to the jet velocity. For the parallel-flow region, the nozzle-to-surface spacing reflects a significant decrease in cross-sectional flow area causing further acceleration of the fluid.

For the jet configurations considered, the nozzle and impingement surface velocities are related by the expression $V_{j,s} = (V_n^2 \pm 2gz)^{1/2}$, where the difference between these two velocities become negligible for large V_n or small nozzle-to-surface spacing (h). For confined and submerged jets, a decrease of the velocity at the jet centerline with increasing h is observed as the exchange in momentum, initially occurring at the perimeter of the jet, ultimately moves inward. The axial distance for which the centerline velocity remains equal usually ranges from 5 to 8 nozzle dimensions. Thus, impingement for nozzle-to-surface spacing above this range will cause $V_{j,s}$ to be lower than the

corresponding V_n [6]. In this literature review, the term jet velocity (V_j) will generally refer to the conditions of the jet at the nozzle exit.

In the following section the heat transfer regimes associated with boiling mechanisms are presented in the form of the boiling curve in order to present the relevant information associated to each regime. This information is especially relevant near the stagnation point as the highest wall temperatures are achieved in this region where the velocity of the coolant is approximately zero. A main concern in water-cooled devices is that the CHF is not exceeded in systems having imposed heat fluxes. At higher heat fluxes the separate vapor bubbles begin to aggregate into a continuous film on the heated surface. This phenomenon is known as boiling crisis, and it constitutes the maximum allowable heat flux before the failure of the system.

2.2 Boiling Heat Transfer

An appreciation for the underlying physical mechanisms involved in boiling heat transfer can be obtained by plotting the wall heat flux as a function of the wall superheat (ΔT_{sat}), that is, the temperature gradient between the wall and the saturation temperatures. This plot is commonly known as the boiling curve (Figure 5).

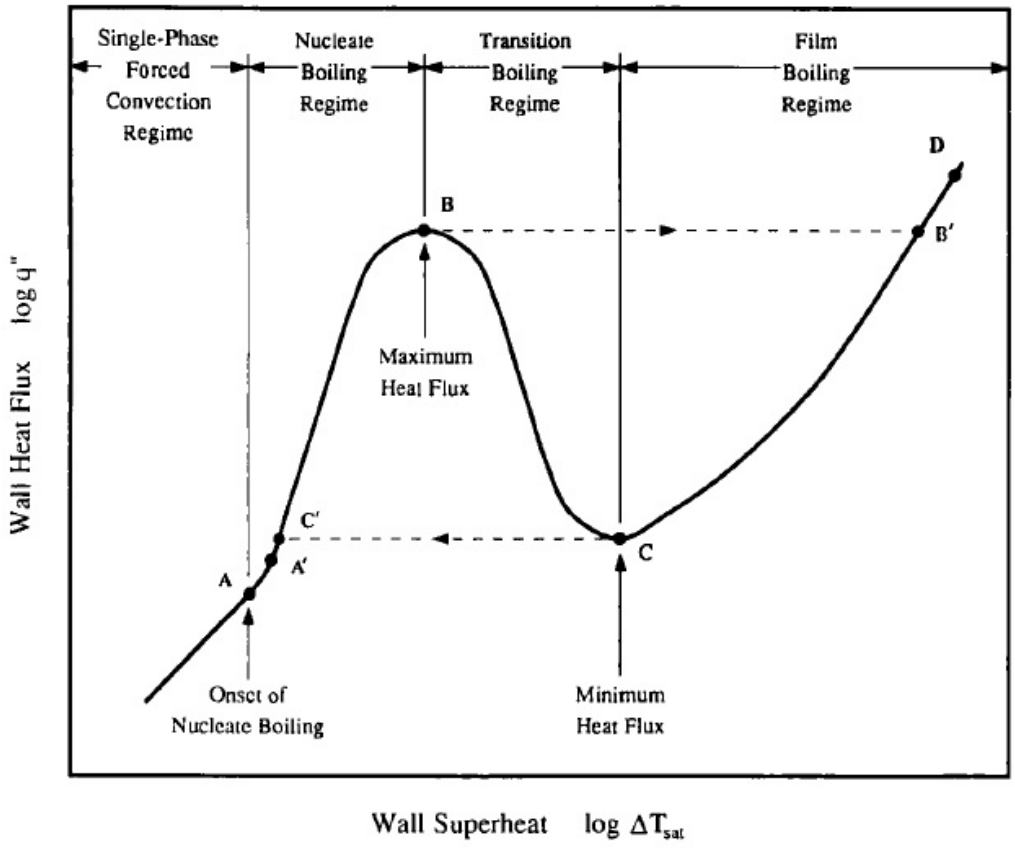

Figure 5. Typical boiling curve for a saturated liquid [6]

Different boiling regimes can be identified in the boiling curve based on the value of the wall superheat, $\Delta T_{sat} = T_{wall} - T_{sat}$. For each regime presented below, the temperature ranges are given for water at atmospheric pressure.

Single-phase force convection: When the wall superheat, $\Delta T_{sat} \leq 5$ °C, there is insufficient vapor in contact with the liquid phase to cause boiling at the saturation temperature. Therefore, single-phase forced convection is the mechanism for heat transfer in the absence of boiling. Newton's law of cooling, $q'' = h(\Delta T_{sat} + \Delta T_{sub})$, governs the relationship between the heat flux and the wall superheat. For jet impingement, the convection heat transfer coefficient (h) varies over the surface due to hydrodynamic variations on the streamwise direction. Moreover, the convection heat transfer coefficient distribution can be affected by the boundary layer development and transition [9]. Further

experimental and numerical discussions for single-phase jet impingement heat transfer can be found in the open literature [10, 11].

Nucleate boiling: When the wall superheat, ΔT_{sat} = 5~30 °C, nucleate boiling occurs. Point A (Figure 5) indicates the onset of nucleate boiling (ONB), where isolated bubbles begin to detach from the surface, prompting local fluid motion, causing the convection coefficient to increase. As the heat flux or wall temperatures increase beyond point A, the vapor bubbles leaving the surface change from small isolated bubbles to groups of many larger vapor bubbles, and these groups merge into slugs of vapor near B. The region between points A B is often called the fully developed nucleate boiling region, where the wall heat flux and $q'' \sim \Delta T^n_{sat}$, and the subscript n is defined empirically [6]. At point B, the heat flux reaches its maximum value, which is commonly called the critical heat flux (CHF). Nucleate boiling is attractive because of the large increases in heat transfer in this regime for moderate changes in surface temperature. As a result, it is the desired region of operation for many high-heat flux cooling applications. However, controlled cooling depends on accurate knowledge of the location of point B. In jet impingement cooling, both single-phase forced convection and nucleate boiling can be simultaneously observed at different locations of the impingement surface because of spatial variations in the wall temperature or heat flux, as reported by Vader et al. [12].

Transition Boiling: The regime corresponding to ΔT_{sat} = 30~120 °C is known as the transition boiling, unstable film boiling, or partial film boiling regimes. In this regime, bubble formation occurs at such a high rate that a vapor film or blanket start to form on the surface. The regime is bounded by point B, the critical heat flux, and point C, the minimum heat flux and temperature. At any point on the surface, conditions may oscillate between

film and nucleate boiling, but the fraction of the total surface covered by the film increases with increasing ΔT_{sat}.

Film Boiling: When ΔT_{sat} > 120 °C, the surface is completely covered by a vapor blanket (point C to beyond point D). The minimum heat flux point, represented in Figure 5 by point C, is known as the Leidenfrost point. The primary mechanism for heat transfer is the forced convection of the vapor, with radiation becoming dominant at (very) high temperatures. For impinging jets, film boiling can often be accompanied by other regimes of boiling on the same surface. At low sub-cooling and high surface temperature, the jet vapor is isolated by the vapor layer [13].

2.3 Jet Cooling Experimental Studies

This section surveys experimental studies of jet impingement cooling, focusing on the characteristics that are pertinent to this thesis. In all these studies, the effects of various flow parameters for confined or submerged circular jets are presented to provide a better understanding of the heat transfer mechanism involved in these configurations, focusing upon the nucleate boiling heat transfer (NB) regime and critical heat flux (CHF) for a single impinging jet.

Forced-convection boiling under sub-cooled and low quality conditions is a highly effective means of cooling with applications ranging from pressurized-water nuclear reactors to large scale digital computers. High heat fluxes can be accommodated with moderate temperature differences because of efficient nucleate boiling, particularly at high velocities and high sub-cooling for jet impingement cooling. Much of the literature available has focused on determining the CHF, and there has is less known about the jet

boiling heat transfer characteristics prior to CHF. Predicting nucleate boiling characteristics is particularly important in temperature-sensitive applications.

Ma and Bergles studied the nucleate boiling heat transfer characteristics of sub-cooled and saturated jets, and considered how certain parameters affected the CHF. Their experimental studies [14, 18] examined the NB regime and heat transfer at CHF in a circular, submerged R-113 impinging jet with 0 °C to 20.5 °C of sub-cooling at velocities ranging from 1.08 m/s to 2.71 m/s. The system pressure was approximately the atmospheric pressure. The jet was oriented normal to the heater, at a nozzle-to-surface spacing twice the jet tube's inner diameter. During the experiment, they evaluated primarily the effects of jet velocity and sub-cooling for jet cooling heat transfer.

When considering the effects of jet velocity, the authors reported that increasing the velocity from 1.08 m/s to 2.71 m/s does not appear to have any effect on the nucleate boiling heat transfer. In the experiments where the effects of sub-cooling on nucleate boiling heat transfer were considered, at a fixed jet velocity, the wall superheat was reduced when increasing the sub-cooling of R-113 from 0 °C to 11.5 °C [18] or to 20.5 °C [14]. In contrast, the effects of sub-cooling ($11.5 \leq \Delta T_{sub} \leq 20.5$ °C) had a marked effect on the CHF for a submerged, circular jet [18], with CHF values that were 30%-80% greater for nonzero subcooling compared with saturated conditions, admittedly for a limited set of three CHF data points. Hence, increasing the sub-cooling increases the CHF.

Two similar studies, Kamata et al. [20, 21] and Mode and Katto [19] performed, experiments on saturated jets focusing on characterization of the NB regime. The results found in these two studies confirm the heat transfer characteristics identified by Ma and Bergles [14, 18].

The experimental work conducted by Monde and Katto [19] also studied the effects of jet velocity, nozzle-to-surface spacing, and nozzle/heater dimensions on NB heat transfer. The experimental setup consisted of a highly confined, circular jet of saturated water impinging on circular heaters of diameter 11.2 mm and 20.2 mm. These two diameters were used to study the effects of varying the heater dimension. A glass plate was attached to the nozzle exit and parallel to the heated surface. Data were presented for confinement heights of 0.3 and 0.5 mm with a nozzle diameter of either 2.0 or 2.5 mm and jet velocities ranging from 8.0 m/s to 17.3 m/s.

The authors reported that the heat flux and surface temperature were seemingly unaffected by jet velocity. In addition, when examining the effects of both nozzle and heater diameters on nucleate boiling heat transfer, there appeared to be no effect on the fully developed nucleate boiling curve for nozzle diameters of 2.0 and 2.5 mm and heater diameters of 11.2 and 20.2 mm. Likewise, Monde and Katto studied the effects of nozzle-to-surface spacing on nucleate boiling heat transfer. For nozzle-to-surface ratios in the range from 4.0 to 8.3, their results showed no apparent effect of the separation distance over this limited range.

Kamata et al. [20, 21] reported experimental results analyzing the jet boiling heat transfer characteristics prior to CHF, that is, during NB where wall superheats are low, $\Delta T_{superheat} = T_{wall} - T_{sat}$. The experimental setup consisted of a circular, confined jet of saturated water with velocities ranging from 10 m/s to 20 m/s impinged upon a flat surface a short distance (from0.3 to 0.6 mm) away from the jet nozzle exit. They primarily examined the effects of jet velocity and nozzle-to-surface spacing.

Like reported by Ma and Bergles [14, 18], in the case of jet velocity, Kamata et al. concluded that the heat transfer coefficient near the stagnation point in the NB regime was independent of jet velocity. In addition, for spacing in the range 0.3 to 0.6 mm, no discernible effect of spacing on the stagnation point heat transfer, in the NB regime, was observed.

A main concern in water-cooled devices is reaching CHF, where dry-out and system failure can occur. At higher heat fluxes the separate vapor bubbles begin to aggregate into a continuous film on the heated surface. This phenomenon is known as boiling crisis, and it constitutes the maximum allowable heat flux before the failure of the system. The survey by Škéma and Šlančiauskas presents a correlation for predicting CHF for single jets taking into account rather extensive data. This study reflects closely the geometric parameters characteristics of the sample holder designs (jet velocity, nozzle-to-surface spacing, degree of sub-cooling, etc.). Therefore, the correlation developed by Škéma and Šlančiauskas is used in later chapters to provide a conservative estimate on the prediction of the CHF.

Škéma and Šlančiauskas [25] investigated the heat transfer characteristics related to CHF for a submerged, circular jet of highly sub-cooled water. The experimental setup consisted of a single sub-cooled jet of water ($85 \leq \Delta T_{sub} \leq 151$ °C) impinged over a heated surface made of copper sheet with diameter D ranging from 9 to 20 mm. Single axisymmetric jets were injected through converging nozzles with outlet diameters d = 3.0, 9.0, and 18.0 mm at jet velocities ranging from 1 to 35 m/s. The ratio of the heated part to the nozzle outlet diameter D/d was varied from 0.5 to 6.7. In order to achieve maximum

CHF densities, relative nozzle-to-surface distances *h/d* were varied from 2 to 4. The absolute pressure in the test section never exceeded 2×10^5 Pa.

The effects of jet velocity on the CHF were considered during the experiments conducted by Škéma and Šlančiauskas. For velocities ranging from 1 to 35 m/s, it was concluded that CHF increases with increasing velocity. Furthermore, the CHF data were fit to a correlation for the CHF q''_{CHF} when boiling occurs at the stagnation point as a function of jet velocity and sub-cooling rate.

$$q''_{CHF} = q''_{CHF_{pool}}[1 + 0.92V_j^{0.44}](1 + \varepsilon_{sub}) \tag{2}$$

Here $q''_{CHF\,pool}$ is the critical heat flux for pool boiling proposed by Kutateladze [26]:

$$q''_{CHF_{pool}} = 0.16\rho_v h_{fg}\left(\frac{\sigma g(\rho_f - \rho_v)}{\rho_v^2}\right)^{1/4} \tag{3}$$

and ε_{sub} is a correction factor for the effect of sub-cooling:

$$\varepsilon_{sub} = 0.112\left(\frac{\rho_f}{\rho_v}\right)^{0.8}\left(\frac{C_{Pf}\Delta T_{sub}}{h_{fv}}\right)^{1.13} \tag{4}$$

The properties are evaluated at the stagnation pressure, $P_s = P_\infty + \rho_l \cdot {V_j^2}/{2}$, where P_∞ is the pressure in test section. In a similar study, Miyasaki et al. [27] suggested that the correlation be used with the fluid properties at the saturation temperature corresponding to the stagnation pressure. The data of Škéma and Šlančiauskas were in reasonable agreement with those of Miyasaka et al. [27] for a planar, free-surface jet.

The effects of heater and nozzle diameters ($3 \le d \le 18$ mm and $9 \le D \le 20$ mm) on CHF for a submerged, circular jet of highly sub-cooled water were also considered. The authors reported that for a heater-to-nozzle diameter ratio of 0.5, the data was well

correlated by Equation 2, which is independent of any characteristic dimension. However, for ratios greater than 0.5, the data are only with about 20% of Equation 2.

In a similar investigation, Andrews and Rao [28] reported critical heat flux data for a submerged, planar jet of water at sub-coolings from 0 to 62 °C and a range of jet velocities from 0.3 to 2 m/s. Like Škéma and Šlančiauskas, Andrews and Rao observed evident trends of increasing CHF with increased sub-cooling. In addition, they reported that the degree of sub-cooling also affected the dependence of CHF on jet velocity. Under saturated jet conditions, the estimated dependence was $q''_{CHF} \sim V_n^{0.1}$, while for a sub-cooling of 33 °C, the estimated dependence was $q''_{CHF} \sim V_n^{0.3}$.

In the review by Katto and Kunihiro [17], trends identified in all of the previous studies discussed, for NB and CHF, are independently confirmed. In addition, an insightful discussion in the effects of nozzle-to-surface spacing and nozzle/heater dimensions on jet cooling performance is presented.

Katto and Kunihiro [17] studied the characteristics associated with fully developed nucleate boiling (FDNB) and critical heat flux (CHF) for a circular, submerged jet of saturated water. Specifically, they analyzed the effects of jet velocity, nozzle-to-surface spacing, and nozzle/heater dimensions on jet cooling performance. The experiment consisted of circular, submerged jet of saturated water with nozzle diameters varying between 0.71 mm to 1.60 mm, which was impinged at jet velocities ranging between 1 to 3 m/s over a circular heater plate of 10 mm in diameter. The nozzle-to-surface spacing was varied between 1 mm to 30 mm using a fine adjustment screw and the experiments were conducted at pool heights of 5 mm and 30 mm for the submerged jet configuration.

Jet velocity was found to have no effect on the FDNB regime. Although the range of nozzle velocities tested was relatively limited (2.04-2.64 m/s), the authors showed that the heat flux and surface temperature were unaffected by jet velocity and the results for pool boiling were extended to higher values of wall superheat, ranging from 18 to 38 °C. In contrast, when considering the effects of jet velocity on the CHF, Katto and Kunihiro concluded that for a jet velocity increasing from 1 to 3 m/s, the CHF increases significantly.

The results also suggested that for a nozzle-to–surface spacing ranging between 1 mm to 10 mm in a 30-mm-deep pool, the CHF increased with increasing jet velocity. Conversely, for a nozzle-to-surface spacing of 30 mm in a 30-mm-deep pool, the effects of velocity were negligible because the initial momentum was too small to affect conditions on the heater surface, and the value of CHF was approximately that of pool boiling.

Katto and Kunihiro [17] studied further the effects of nozzle-to-surface spacing on the CHF. The considered nozzle-to-surface spacing ranged from 1 to 30 mm ($0.6 \leq z/d \leq 42$). They observed significant effects of spacing, with the smallest spacing yielding the largest values of CHF. Moreover, as spacing was increased, the effects of jet velocity diminished. It was reported complete invariance when the separation distances reached 30 mm, for which the CHF is governed by pool boiling parameters. Results for 5 and 30 mm deep pools showed several relevant features concerning the effects of the jet configuration on CHF. It was concluded that the closest nozzle-to-surface spacing consistently yielded the highest values for CHF. It was also showed that nozzle-to-surface spacing 1 to 3 mm yielded larger values of CHF for a pool height of 5 mm than for a height of 30 mm. Similarly, the effects of nozzle diameter were studied by Katto and Kunihiro. They showed

that the nozzle diameter (0.71 - 1.60 mm) had no effect on the relationship between the surface temperature and heat flux.

Katto and Kunihiro also considered the effect of having a layer of bubbles blanketing the surface, and concluded that when an impinging jet near the heated surface supplies in the case of supplying liquid to the nucleate-boiling-liquid-layer, the obstacle to the supply of liquid caused by the vapor mass (bubble blanketing) can be suppressed by raising the velocity of the liquid jet.

Perhaps the most relevant investigation conducted for jet impingent on a concave, hemispherical surface, reflecting the geometry of the sample holders, was conducted by Aihara and his co-workers (Aihara et al. [22]; Ishimaru et al. [23]). The authors considered the effects of various parameters on the NB regime and CHF for this jet configuration.

Aihara et al. [22, 23] examined the heat transfer characteristics associated with NB and CHF for a circular, submerged jet of saturated liquid nitrogen impinged onto a concave, hemispherical surface and a flat surface (with and without a needle). The authors evaluated the effects of jet velocity, nozzle-to-surface spacing, and heater/target geometry for this jet configuration. The experimental setup consisted of a circular jet of saturated liquid nitrogen flowing out of an inner tube of 0.8 mm in diameter onto a concave, hemispherical target with 2.2 mm in diameter at a jet velocity ranging from 0.77 to 1.64 m/s. After cooling the area of impingement, the liquid nitrogen passed through the annular space between the outer and inner tube of about 0.6 mm, and was finally released into ambient air. Information concerning the operating pressure or saturation temperature was not provided in either investigation.

For a fixed heat flux, the authors reported that increasing jet velocity, from 0.77 to 1.64 m/s, caused a slight decrease in wall temperatures equivalent to ~ 15 % lower wall superheats, $\Delta T_{superheat} = T_{wall} - T_{sat}$, for NB. In contrast, when considering the effects of jet velocity on the CHF, Aihara et al. showed that the relationship between the CHF and jet velocity ($0.77 \leq V_n \leq 1.64$ m/s) was of the form $q''_{CHF} \sim V_n^{0.6}$. In this investigation, jet velocities above 1 m/s were able to sustain critical heat fluxes in excess of 1 MW/m^2.

Aihara et al. also studied the effects of the nozzle-to-surface spacing, also known as separation distance. The separation distance was varied from 0.5 to 2.2 mm for a given heat flux, while the nozzle diameter was 0.8 mm in all the experiments. The behavior exhibited in the NB and CHF can be explained by considering the effects of reducing the separation distance. As the distance is shortened, the apparent heat transfer coefficient increases $\dot{q}_a/\Delta T_{sat}$ and the apparent CHF $(\dot{q}_a)_{CHF}$ becomes high. The reason for this is as follows. Since the configuration was designed to be a boiling system of the impinging jet in an extremely confined space, a greater distance reduces the velocity (inertia force) of the coolant impinging onto the heat transfer surface; hence, the ability of removing vapor bubbles from the heated surface reduces significantly. In the case of a shorter separation distance, the velocity boundary layer in the wall-jet region, apart from the stagnation point, becomes thinner, and bubbles on the heat transfer surface are effectively removed; consequently, the apparent heat transfer coefficient can be improved. Therefore, it was found that decreasing nozzle-to-surface spacing ($0.65 \leq h/d \leq 2.75$) caused a resultant decrease in wall superheat of approximately 20 % over the entire range for the FDNB. Similarly, the authors reported that the CHF increases monotonically as the nozzle-to-surface spacing decreases for spacings ranging from 0.6 to 2.2 mm. In addition, it was

observed that CHF was increased by approximately 120% as the separation distance was reduced from 2.2 mm to 0.5 mm at a constant jet velocity of 1 m/s.

Aihara et al. also studied how the heater geometry affected NB and CHF heat transfer. The three radially confined heater surfaces considered were a flat surface (A_w = 4.15 mm^2), a concave hemispherical surface (A_w = 8.31 mm^2), and a flat surface with a small needle (A_w = 6.32 mm^2). For a fixed heat flux, the flat surface with a needle showed the best cooling performance because it had a relatively large surface for heat transfer, also, forced convection appeared favored by this geometry for the region of small ΔT_{sat} (NB), giving wall superheats that were approximately 30% lower than those for the flat and hemispherical surfaces. Nevertheless, at high ΔT_{sat}, the hemispherical surface showed the maximum cooling performance. The CHF for the hemispherical surface was approximately 70% and 90% greater than that for the flat surface with and without the needle, respectively. The improved performance was attributed to the hemispherical surface having the largest heat transfer area (A_w = 8.31 mm^2). In addition, the hemispherical surface offered the best inner shape as flow in the stagnation region made it less prone to induce burn-out, which was not the case for the flat surface with the needle where dry spots were observed in the stagnation zone.

2.4 Numerical Simulations

In order to assess the thermal performance for the different sample holder configurations, in this thesis, turbulent jet impingement as means of cooling is explored numerically. All of these simulations performed as part of this thesis utilized the commercial computational fluid dynamics software package, ANSYS™ FLUENT®.

The following sections provide a brief summary of the wall boiling model, namely Rensselaer Polytechnical Institute (RPI) model, implemented within ANSYS™ FLUENT® in order to provide a better understanding of the origin, validation, range of applicability, and limitations of this mechanistic model. Also, previous modeling works on jet impingement systems involving nucleate boiling are presented to provide some degree of confidence in the wall boiling model developed. However, it is important to note that CFD modeling of boiling jets and critical heat flux prediction is still in its infancy and it is far from close to state of the art in its modeling capabilities in this area [29, 30]. There are limited literature resources available demonstrating the capabilities of ANSYS™ FLUENT® in the characterization of jet impingement systems involving nucleate boiling; therefore, any simulation work conducted using this software should be considered preliminary and requires extensive experimental validation.

2.4.1 The RPI Model

The RPI model wall heat partitioning based on a mechanistic approach allows investigating a variety of cases of interest involving boiling heat transfer. Some of the current CFD codes, including ANSYS™ FLUENT®, simulate wall boiling by means of the RPI or wall heat flux partitioning model, which was originally formulated by Kurul and Podowski [33] at Rensselaer Polytechnical Institute. The model is based on the Bowring [7] scheme of accounting for the various boiling heat transfer mechanisms separately. It only considers three mechanisms to extract heat from a heated wall: the latent heat of evaporation to form the bubbles $q_e^{"}$, heat expended in re-formation of the thermal boundary layer following bubble departure known as quenching heat flux $q_q^{"}$, and heat transfer to the liquid phase outside of the zone of influence of the bubbles by convection $q_c^{"}$. Moreover, it

was designed to be applied in nucleate sub-cooled boiling applications and moderate gas volume fraction near the heated walls. However, if the amount of vapor evaporated near the wall is so high that vapor covers most of the wall surface, this vapor may isolate the wall from the sub-cooled fluid. In such situations, none of those three mechanisms are anymore taking place, or at least are not the main driving processes. Hence, improved versions of the RPI model have been implemented within ANSYS™ FLUENT® in order to extend the range of applicability of the RPI model past CHF into post dry-out conditions. The extended formulation for the departed nucleate boiling regime (DNB) was formulated according to Lavieville et al. [32]. Most of the ground work in the development of the wall boiling model, mechanistic as well as empirical, was conducted for simple geometries such as circular uniformly heated tubes and square ducts. None of the mechanistic nor empirical correlations have been developed for complex geometries. Therefore, careful attention must be given to the range of applicability of the RPI model (extended or not) for complex geometries such as the one presented by the sample holders. In the case where moderate volume fractions expected to be below 20 %, the ANSYS™ FLUENT® user manual recommends using the RPI model within its boiling model options [48]. Whenever the multiphase flow regime changes from a bubbly flow to a mist flow, the critical Heat Flux model (RPI-CHF model), an extended version of the RPI model, is recommended [48]. Nevertheless, the numerical instabilities associated with the non-equilibrium wall heat flux partition characteristic of the RPI-CHF model, in the case of complex flows and complex geometries, often present convergence problems [56].

The RPI boiling model (specially, for sub-cooled boiling) was originally validated by Podowski and co-workers against measurements for several different sets of data

demonstrating that CFD methods of multiphase flows can be successfully used to perform multidimensional simulations of boiling channels and systems (Kurul and Podowski, 1990 [33]), (Kurul and Podowski, 1991 [31]) , (Anglart, 1993 [15]), (Anglart et al., 1997 [16]), (Alajbegovic et al., 1997 [24]), (Podowski et al., 1997 [34]), (Podowski, 2008 [56]), (Podowski, M. Z. and Podowski, R. M., 2009 [57]). In all cases, the results of the numerical simulations have shown consistency of the proposed modeling concepts and good agreement with the experimental data. However, the accuracy of such simulations strongly depends on the availability of mechanistic closure laws of local boiling mechanisms, specially, inside the boundary layer near the heated wall.

In work presented by Kurul and Podowski (1990) [33], the proposed boiling model was validated against several experimental results for circular heated channel (Rouhani, 1966 [58]), (Bartolomei and Chanturia, 1967 [59]), (Hino and Ueda, 1984 [60]), (Saha, 1974 [61]). The data in the majority of the reviewed experimental works have been limited to the axial distribution of the channel-average void fraction. In most cases, which were tested, good agreement was found between the calculations and the measurements. The most consistent and extensive sets of data turned out to be those of Rouhani (1966) [58] and Bartolomei & Chanturia (1967) [59]. The results of the comparison between the latter experiments and the calculations using the proposed boiling model are shown in Figure 6. The 2-D model equations, pertinent to the boiling model, were solved using the PHOENICS code (Spalding, 1981 [62]) as a solver of the governing equations. In addition, 1-D calculations were performed for the same conditions with a drift-flux model similar to that used by Park et al. (1986) [63]. The wall temperature in the drift-flux model was calculated from the Jenns-Lottes correlation [7].

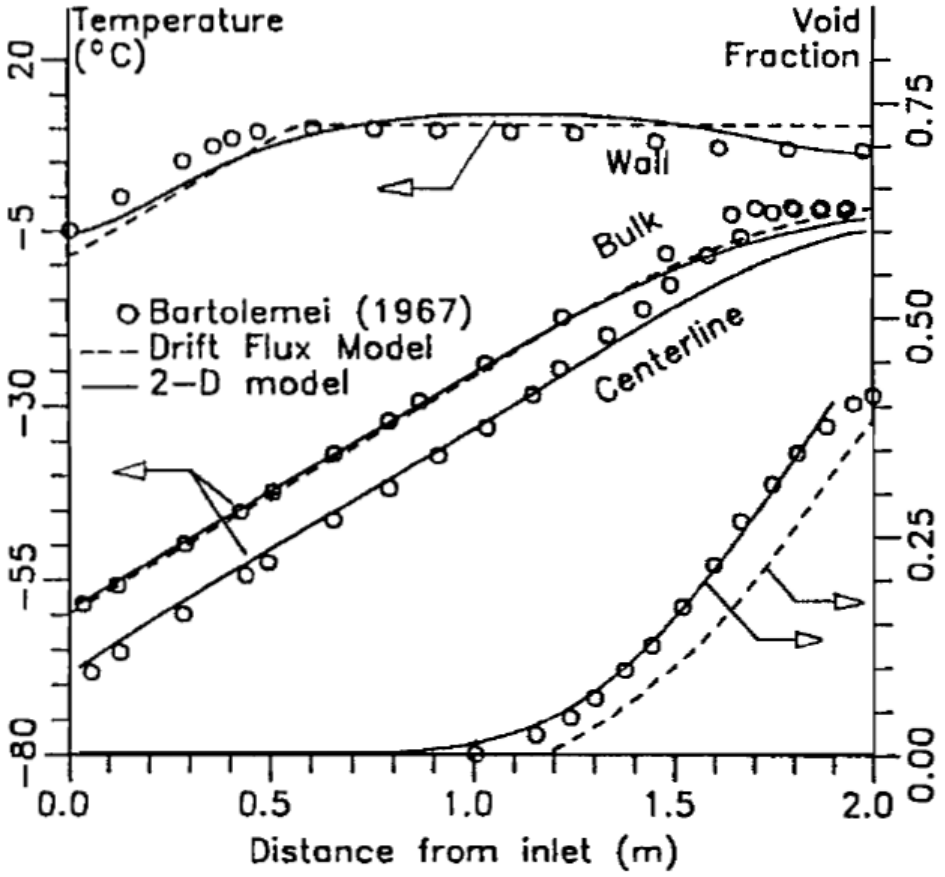

Figure 6. Axial steady-state distributions of temperature and void fraction in a vertical uniformly heated channel [33]

The resultant void fractions and temperature distributions are given in Figure 6. The diameter of the vertical test channel was 0.0154 m, the wall heat flux was 5.7×10^5 W/m^2, and the inlet mass flux was 900 kg/m^2-s at 4.5 MPa. As can be seen, good agreement was obtained between the model predictions and the experimental data hence indicating the capabilities of the wall boiling model. As previously indicated, further validation of the proposed boiling model have been conducted by Podowski and co-workers. [15, 16, 24, 31, 34, 56, 57]. Although a decent level of confidence in the characterization of boiling channels and systems has been acquired from some of the multidimensional simulation works conducted, the accuracy of such of simulations strongly depends on the availability

of mechanistic closure laws of local boiling mechanisms, specially, inside the boundary layer [51].

2.4.2 Wall Boiling Model Description

The physical scenario in which the wall temperature is high enough to cause boiling, even though the average bulk fluid temperature is below the corresponding saturation temperature, is referred to as sub-cooled boiling. Due to its inherent great improvement on the capacity for heat transfer, a lot of attention has been given to sub-cooled boiling over single phase convection. Hence, sub-cooled boiling is widely used in industrial applications. In ANSYS™ FLUENT®, the wall boiling models are developed in the context of the Eulerian multiphase model to simulate and characterize systems, such as the sample holders, where boiling heat transfer, sub-cooled boiling included, must be considered. The multiphase flows are governed by the conservation equations for mass, momentum, and energy given by Equations 5, 6, and 7, respectively.

$$\frac{\partial}{\partial t}\left(\alpha_q \rho_q\right) + \nabla \cdot \left(\alpha_q \rho_q \vec{v}_q\right) = \sum_{p=1}^{n} \dot{m}_{pq} \tag{5}$$

$$\begin{aligned} \frac{\partial}{\partial t}\left(\alpha_q \rho_q \vec{v}_q\right) + \nabla \cdot \left(\alpha_q \rho_q \vec{v}_q \vec{v}_q\right) & \\ = -\alpha_q \nabla \mathrm{P} + \nabla \cdot \bar{\bar{\tau}}_q + \alpha_q \rho_q \vec{g}_q & \\ + \sum_{p=1}^{n} \left(\vec{R}_{pq} + \dot{m}_{pq} \vec{v}_{pq}\right) + \alpha_q \rho_q \left(\vec{F}_q + \vec{F}_{lift,q} + \vec{F}_{vm,q}\right) & \end{aligned} \tag{6}$$

$$\frac{\partial}{\partial t}\left(\alpha_q \rho_q h_q\right) + \nabla \cdot \left(\alpha_q \rho_q \vec{v}_q h_q\right)$$

$$= -\alpha_q \frac{\partial p}{\partial t} + \bar{\bar{\tau}}_q : \nabla \vec{v}_q - \nabla \vec{q}_q + S_q + \sum_{p=1}^{n} \left(Q_{pq} + \dot{m}_{pq} h_{pq}\right) \tag{7}$$

where α is the phase volume fraction of phase q, ρ is the density, $\vec{v}$ is the velocity vector, and $\dot{m}$ is the volumetric mass exchange rate between phase p and q, $\dot{m}_{pq}$ is the rate of vapor per unit of volume. In Equation 6, $\bar{\bar{\tau}}_q$ is the shear stress, $\vec{R}$ is the interfacial drag force, $\vec{F}_q$ is the turbulent diffusion force, $\vec{F}_{lift,q}$ is the lift force, P is the pressure, and $\vec{g}$ is the gravitational acceleration vector. In Equation 7, h is the enthalpy, $\vec{q}$ is the heat flux vector, S is the source term, Q is the energy exchange term between the different phases, and h_{pq} is the difference in the formation enthalpies of the phases p and q. In general, the energy balance at the infinitely thin wall separating fluid and solid cells is given by Equation 8.

$$h_{sol,w}\left(T_{sol}^{cell} - T_w\right) = \alpha_l^{cell}\left[q_E^{"} + q_Q^{"} + q_C^{"}\right] + \alpha_v^{cell}\left[h_{vw}(T_w - T_v^{cell})\right] \tag{8}$$

where the left-hand side of Equation 8 represents the solid side heat flux due to conduction, the first and second terms on the right-hand side of Equation 8 denote parts of heat flux going into liquid and vapor phases, respectively.

As previously stated, the accuracy of the simulations strongly depends on the availability of mechanistic closure laws of local boiling mechanisms, specially, inside the boundary layer near the heated wall. To model the local near-wall heat transfer, Kurul and Podowski (1990) [33] proposed an approach based on partitioning the total wall heat flux into three terms, namely the RPI model, as shown in Equation 9.

$$q_w^{"} = q_C^{"} + q_Q^{"} + q_E^{"} \tag{9}$$

where $q_C^{"}$ is the liquid convective heat flux, $q_Q^{"}$ is the quenching heat flux, and $q_E^{"}$ is the evaporative heat flux. These values are weighted depending on the amount of vapor present at the wall. Under sub-cooled boiling conditions, the wall surface is subdivided into portion Ω ($0 \leq \Omega \leq 1$), covered by nucleating bubbles, and portion $1 - \Omega$, covered by fluid. Ω is referred to, in the RPI model, as the area of influence. The convective heat flux is related by Equation 10.

$$q_C^{"} = h_{lw}(T_w - T_l) \cdot (1 - \Omega) \tag{10}$$

where h_{lw}, the single-phase heat transfer coefficient, is derived from either the log law if flow is turbulent or Fourier law is flow is laminar. T_w and T_l are the wall and liquid temperatures, respectively. Liquid phase properties must be used while calculating h_{lw} for either turbulent or laminar flow. Del Valle and Kenning [36] assumed that as a bubble departs, it carries an area of the superheated thermal boundary layer with it in its wake equal to twice the bubble diameter. Then, the cool liquid that rushes in to replace it is heated via transient conduction from the heater thus the total quench heat flux $q_Q^{"}$ is given as shown by Equation 11.

$$q_Q^{"} = \frac{2k_l}{\sqrt{\pi \lambda_l T}}(T_w - T_l) \tag{11}$$

where k is the thermal conductivity, T is the periodic time, and $\lambda_l = k_l/\rho_l C_{pl}$ is the thermal diffusivity. The latent heat of evaporation to form the bubbles, namely the evaporative heat flux, is given by Equation 12.

$$q_E^{"} = V_d N_w f \rho_v H \quad (12)$$

where V_d is the volume of bubble based on the bubble departure diameter, N_w is the nucleation site density, ρ_v is the vapor density, H is the latent heat of evaporation, and f is the bubble departure frequency. In Equations 10-12, a closure must be provided for wall boiling parameters. Several existing closure relationships were considered for implementation in the model. Kurul and Podowski [33] selected the correlations to describe the remaining wall boiling parameters based on the following criteria:

- A general form of the models should be based on mechanistic considerations, so that non-mechanistic/empirical aspects are limited to the necessary scalar quantities only.
- The models do not violate the fundamental invariance principles.
- The constitutive models, whenever applicable, reduce to known theoretical results for simplified flow and heat transfer conditions (such as single spherical bubbles, for example).
- For continuous phase, two-phase flow models reduce to single-phase models when the concentration of the dispersed phase approaches zero.
- The range of validity of the hydrodynamic models extend to adiabatic flows and developing flow conditions
- The proposed new local constitutive equations are consistent with the existing cross-section averaged correlations.
- Whenever experimentally-verified correlations are known for selected conditions only, a linear interpolation method is used to obtain constitutive laws for gradually changing conditions.

Specific sub-models have been considered to account for the interfacial transfer of momentum, mass, and heat, as well as turbulence models in boiling flows. Detailed descriptions of the relevant correlations within the wall boiling model are provided below.

The area of influence Ω, the portion of the surface covered by nucleating bubbles, is strongly dependent on the departure diameter, D_w, and the nucleation site density as can be observed in Equation 13.

$$\Omega = K\frac{N_w \pi D_w^2}{4} \tag{13}$$

In order to avoid numerical instabilities due to unbound empirical correlations for the nucleate site density, the area of influence must be limited as presented by Equation 14.

$$\Omega = min\left(1, K\frac{N_w \pi D_w^2}{4}\right) \tag{14}$$

where the value of the empirical constant *K,* which helps determining the ratio of the area of influence to the maximum bubble projected area. Conventionally, *K* is expected to have a value of about 4; however, it has been found that this value can vary between 1.8 and 5. Equation 15 describes the relation for this constant that has been implemented based on Del Valle and Kenning's findings [36].

$$K = 4.8 \cdot exp\left({}^{-Ja}/_{80}\right) \tag{15}$$

where the Jacob number is obtained using the formulation proposed by Kenning and Victor, $Ja = C_{pl}\rho_l(T_{sat} - T_l) \cdot (\rho_v L)^{-1}$ [37]. Correct prediction of bubble departure diameter is very important because evaporation rate depends strongly on this parameter, as observed in Equation 12. For sub-cooled boiling, this value is controlled by condensation

at the top of the bubble. A correlation for D_w for sub-cooled boiling was developed by Unal [38] using a high-speed photographic technique and the data available in the literature. In sub-cooled boiling, the recommended expression for the bubble departure diameter is given by Equations 16.

$$D_w = 2.42 \times 10^{-5} P^{-0.709} \left(\frac{a}{b\sqrt{\varphi}} \right) \tag{16}$$

where the parameters in Equation 16 are:

$$a = \frac{\Delta T_{sat}}{2\rho_v H} \sqrt{\frac{\rho_s C_{ps} K_s}{\pi}} \tag{17}$$

$$b = \frac{\Delta T_{sup}}{2\left(1 - \frac{\rho_v}{\rho_l}\right)} \tag{18}$$

$$\varphi = max\left(\frac{U_b}{U_o}, 1.0\right) \tag{19}$$

Here, P is the flow pressure, $\Delta T_{sat} = T_w - T_{sat}$ is the wall superheat, H is the latent heat of evaporation, U_b is the near wall bulk velocity, and U_b = 0.61 *m/s*. The experimental range of validity for Equation 16 is P = 0.1 – 17.7 MPa, q''_w = 0.47 – 10.64 MW/m2, v = 0.08 – 9.15 m/s, ΔT_{sub} = 3 – 86 K, and bubble diameter D_m = 0.08 – 1.24 mm. The *s*, *l*, and *v* denote the solid material, liquid and vapor phase, respectively. Nucleation site density is found using Equation 20, which is a general expression based on the wall superheat.

$$N_w = C^n (T_w - T_{sat})^n \tag{20}$$

Here C and n are the empirical parameters given by Lemmert and Chawla, where $n = 1.805$ and $C = 210$ [39]. Application of the RPI model generally uses the frequency of bubble departure as the one based on inertia controlled growth. This parameter was determined empirically by Cole [35] using frame-by-frame measurements made of bubble diameters and bubble positions from high speed photographs of the boiling phenomena for water. The resultant correlation is shown below, Equation 21 [69].

$$f = \sqrt{\left(\frac{4g(\rho_l - \rho_v)}{3\rho_l D_w}\right)} \tag{21}$$

Further detail in all closure relationships for the relevant parameters presented within the context of the wall boiling model can be found in the ANSYS™ FLUENT® user manual [48] or the indicated references for each correlation [35, 36, 37, 38, 39,].

2.4.3 Turbulence Model Equations

The turbulence model selection was based on the collective experience of multiple numerical studies where the wall boiling models were used along with the *k*-epsilon model. For instance, numerical work conducted by Podowski et al. (1997) [40] on the CFD prediction of flow and phase distribution in fuel assemblies with spacers showed satisfactory results when using the *k*-epsilon model within the framework of the CFD computer code CFDS-FLOW3D. In a recent numerical study conducted by Zhang et al. (2014) [52], a two-fluid model employing the *k*-epsilon model was used to investigate the departure from nucleate boiling (DNB) phenomena in vertical pipes within the framework of ANSYS™ FLUENT® showing satisfactory results. In addition, simulation work performed by Narumanchi et al. (2008) [43], presented in the next section, showed that the

usage of the *k*-epsilon model, within the framework of ANSYS™ FLUENT®, provided reasonable agreement for the simulation of saturated boiling jets.

Aside from the apparent standard the *k*-epsilon model has become in the CFD community, the ANSYS™ FLUENT® recommends its use when Eulerian multiphase model are used along with wall boiling models [48]. Since most sub-cooled boiling flows are turbulent, the mixture phase *k*-epsilon model is used. The turbulent kinetic energy correlation is presented by Equation 22.

$$\frac{\partial}{\partial t}(\rho_m k_i) + \nabla \cdot (\rho_m \vec{v}_m k_i) = -\nabla \cdot \left(\frac{\mu_{t,m}}{Pr_{k_i}} \nabla k_i\right) + G_{k_i,m} + \rho_m \varepsilon + S_{k_i} \tag{22}$$

where k_i is the turbulent kinetic energy, μ is the viscosity, ε is the dissipation rate, G is the turbulence production rate, and S_k is the bubble-induced turbulence in the turbulent kinetic energy equation. In the same manner, Equation 23 presents the dissipation rate equation.

$$\frac{\partial}{\partial t}(\rho_m \varepsilon) + \nabla \cdot (\rho_m \vec{v}_m \varepsilon) = -\nabla \cdot \left(\frac{\mu_{t,m}}{Pr_\varepsilon} \nabla \varepsilon\right) + \frac{\varepsilon}{k}\left(C_{\varepsilon 1} G_{k,m} - C_{\varepsilon 2} \rho_m \varepsilon\right) + S_\varepsilon \tag{23}$$

where $C_{\varepsilon 1}$, $C_{\varepsilon 2}$ are constants and S_ε is the bubble-induced dissipation in the dissipation rate equation. As described by Equations 22 and 23, the conventional mixture *k*-epsilon model contains two additional terms that describe additional bubble stirring and dissipation. These additional terms for the turbulent kinetic energy and dissipation rate equation can be calculated using Equations 24 and 25, respectively.

$$S_{k_i} = \frac{0.75 C_d \rho_l \alpha_v |\vec{v}_r|^2}{d_v} \tag{24}$$

$$S_\varepsilon = C_{\varepsilon 3} \frac{3 C_d |\vec{v}_r|}{d_v} S_k \tag{25}$$

where $C_{\varepsilon 3} = 0.45$ as evaluated by Troshko and Hassan [41].

2.4.4 Previous Wall Boiling Model Validation Work Including Jet Impingement Cooling

In this section, previous validation work of the wall boiling model, specifically, RPI model is presented. Although some multiphase models have been presented in the literature [33, 34] and modeling of nucleate boiling on a heated surface has been attempted [42], CFD modeling demonstrating numerical phenomena such as jet cooling involving nucleate boiling [43] are just beginning to appear in the literature.

Work conducted by Narumanchi et al. (2008) presented validation of the RPI model within ANSYS™ FLUENT® [43]. Experimental results with submerged jets involving nucleate boiling were compared to the predictions of the numerical models. First, Narumanchi et al. [43] examined the experimental study of Katto and Kunihiro [17].

A jet of water with 3 °C of sub-cooling was impinged onto a heated disk of 10-mm-diameter. For this experiment, the nozzle diameter and jet velocity were 1.6 mm and 2 m/s, respectively. For this submerged jet configuration, an axisymmetric domain was established. The Reynolds Normalization Group (RNG) *k*-epsilon model with standard wall functions was used. All the results presented by Narumanchi et al. were independent of mesh size (within 5%). As reported, the experimental results were close to the stagnation superheat (within 20%), which is encouraging. Given the nature of this problem, uncertainties of the order of even 30% are acceptable.

Narumanchi et al. [43] considered another experimental study with submerged boiling jets, the study by Zhou and Ma using a submerged R-113 jet [44]. The rationale for choosing this study was that it involved a fluid other than water, it involved sub-cooling and it was performed at both low (0.41 m/s) and high (11.36 m/s) velocities. A R-113 jet with 18.5 °C of sub-cooling at atmospheric pressure impinging on a 2.8-mm-diameter disk from a 1-mm- diameter nozzle. As a simplification, the domain was assumed to be axisymmetric. The RNG *k*-epsilon model with standard wall functions was used. At the elevated velocity, the saturation temperature of the fluid changes along the target wall; this aspect is shown to be accounted for in the code. At the lower velocity, the wall superheat fluctuates quite a lot; hence, time-averaged quantities were reported. The results for wall superheat presented mesh-independent values to within 2%. Agreement between experiments and CFD predictions was determined to be within 10%. For the higher velocity case, at lower heat fluxes, no significant difference was found between the single-phase and boiling predictions. Nevertheless, the single-phase case showed higher wall temperatures as compared to the boiling case when the heat flux was increased, an indicator to the effect of boiling in reducing the wall temperatures.

Although experiments are essential, modeling can yield very useful information when used within their range of applicability. Overall, it could be stated that the experimental validations presented in this section give some degree of confidence in the predictions yielded by the Eulerian multiphase model implemented in ANSYS™ FLUENT®. In the following chapters, the numerical models developed for the sample holders are presented and experimental validation is conducted. These numerical models

are then used to assess the thermal performance in order to predict safe limits of operation and testing for the various sample holder designs.

CHAPTER 3: NUMERICAL MODELING

3.1 Numerical Modeling of Gen 1 Sample Holder

A numerical model was constructed to evaluate the thermal performance of the Gen 1 sample holder used during HHF testing conducted at the IMTS facility located at ORNL. This numerical model is built using FLUENT® in ANSYS™ Workbench® 14.0 and solves the conservation equations for mass, momentum, and energy in the coolant, and conduction heat transfer in the solid. Experimental data collected from HHF transient experiments was provided by Dr. A. S. Sabau, from the Material Science & Technology Division at ORNL, and used in the simulations as boundary conditions. The following sections provide details related to the development of the numerical model. Furthermore, evaluation of the numerical predictions against experimental data, for a nominal transient case, is conducted in order to assess the applicability of the model and the effects of the assumptions made during its development.

3.1.1 Problem Setup

The Gen 1 sample holder, presented in Figure 7, was used during HHF testing conducted at the IMTS facility located at ORNL. This design is the first of two sample holders considered in this thesis. It consisted of a Molybdenum holder (Mo-holder), a Copper cooling rod (Cu-rod), and a stainless steel jet cartridge (SS-cartridge). The Cu-rod was made out of a Copper alloy (C10100) with a high thermal conductivity (~ 391 W/m-K) favorable for the sample holder design. Molybdenum was the material of choice for the fabrication of the Mo-holder because of its optimal physical properties, specifically, high

melting temperature and thermal conductivity. For the SS-cartridge, the SS-304L, an austenitic Chromium-Nickel stainless steel, offered the optimum combination of corrosion resistance, strength, and ductility.

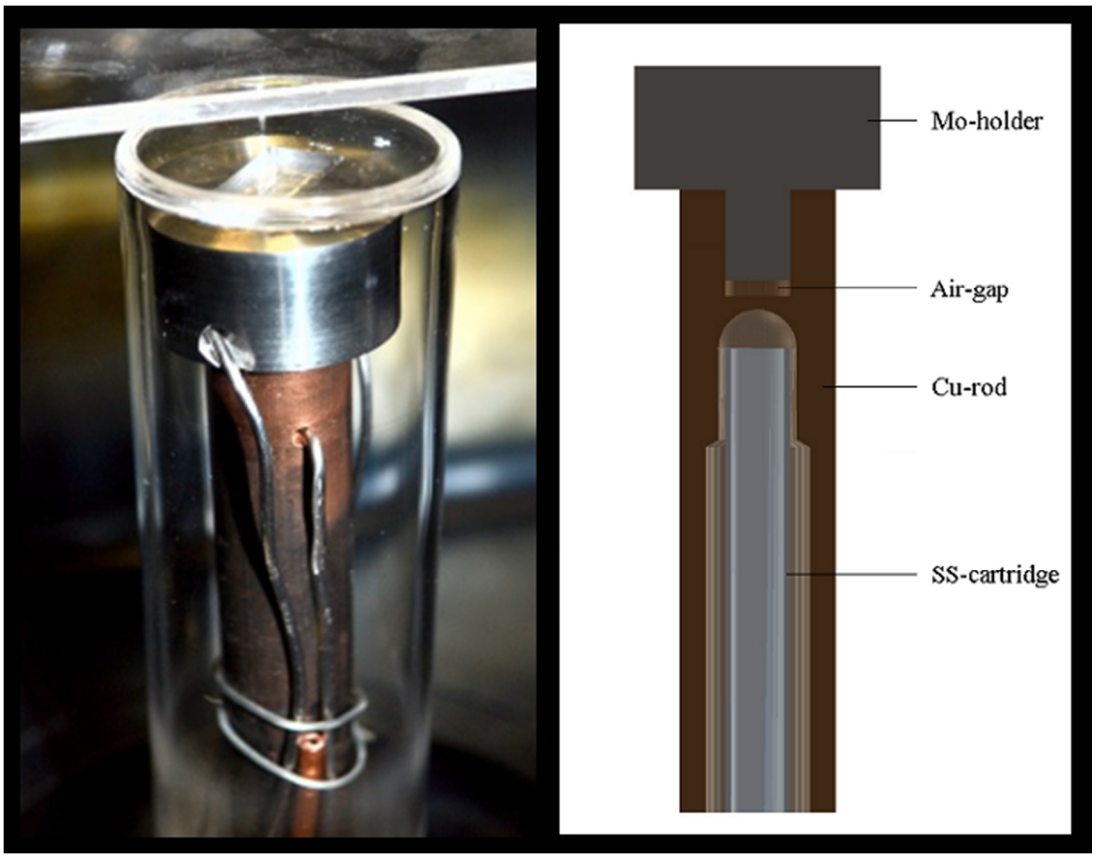

Figure 7. Gen 1 sample holder test stand composed of quartz cylinder for containment of volatile radioactive gases, water-cooled rod, Mo-Holder, and thermocouples.

Using the ANSYS™ DesignModeler® tool, a 2D axisymmetric model was developed, shown in Figure 8, consisting of the Mo-holder, Cu-rod, and SS-cartridge. In addition, a 2.1 mm air-gap, measured during the experiments, was included in the model representing the distance between the bottom of the Mo-holder insert and the Cu-rod threaded cavity [47]. In the model, all external surfaces on the solid body were assumed to be adiabatic except the two faces where the heat flux is incident. Furthermore, the effect of the contact resistance between the Mo-holder and the Cu-rod was assumed to be negligible.

As discussed by Sabau (2014), the heat flux profile of the PAL can be assumed to be uniform [5]. The values of the incident heat fluxes used for validation are those presented in Table 2, which reflect the experimental conditions provided in the literature explaining the experimental work conducted with the Gen 1 sample holder [45]. Also, experimental measurements were performed to estimate the heat flux incident on the cylindrical side wall of the Mo-holder (perpendicular to the PAL) which was estimated to be an additional 10 % of the heat flux incident on the top face surface [47].

Table 2. Setup and input parameters for nominal transient case related to Gen 1 sample holder

Testing Parameters					
Cycle Specifications	Cycle 1	Cycle 2	Cycle 3	Cycle 4	Cycle5
Heat Flux [MW/m^2]	2.65	2.43	2.30	2.17	2.17
Irradiation Time [s]	15	15	15	15	15
Dwell Time [s]	120	120	120	120	120
System Parameters					
Pressure [psi]	80				
Mass Flow Rate [kg/s]	0.032				
Coolant Inlet Temperature [K]	287.15				
k-ε Model Input Parameters					
Boundary	Inlet		Outlet		
Turbulent Kinetic Energy 'k'	4.42×10^{-3}		9.68×10^{-4}		
Turbulent Dissipation Rate 'ε'	1.08×10^{-1}		1.48×10^{-2}		

Further details on the experimental setup and procedure for HHF testing, conducted at the IMTS facility, can be found in the published literature [5, 45]. Due to the large temperature gradients expected within the solids, for the range of experimental heat fluxes,

temperature dependence of the material properties have been accounted for. A detailed compilation of the temperature dependent properties for all materials is available in Appendix B. In addition, the User Defined Function (UDF) created as a materials input for ANSYS™ FLUENT® is included in Appendix C.

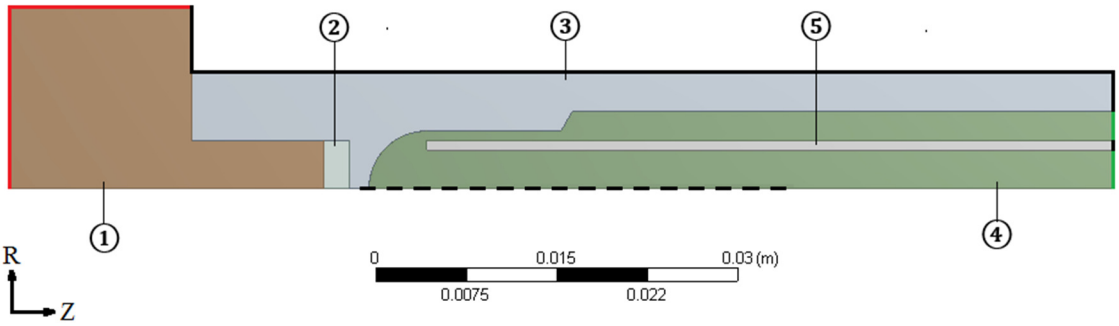

Figure 8. 2D axisymmetric model used in the Gen 1 sample holder CFD analysis composed by Mo-holder ①, air-gap ②, Cu-rod ③, coolant ④, and SS-cartridge ⑤. Solid black lines indicate adiabatic boundary conditions, red lines indicate heat flux boundary condition, green lines indicate coolant boundary conditions (mass flow inlet and pressure outlet), dash black line indicates symmetry axis 'Z' and the radial direction is indicated by the 'R' axis

The turbulence model was chosen based on previous work conducted by Narumanchi et al. (2008) [43]. After conducting validation of previous experimental results obtained by Katto and Kunihiro [17] and Zhou and Ma [44], it was shown that the RNG k-ε turbulence model with standard wall functions was able to successfully reproduce, within acceptable agreement, the experimental results for a submerged, circular jet impinging on a flat surface. In order to better represent the complex flow on the concave surface of impingement, for the sample holder, the realizable k-ε model (RKE) instead of the RNG is used as it provides more accurate results for separated flows and flows with complex secondary flow features [48]. Another consideration fundamental in the accurate prediction and stability of flow phenomena based on these turbulence models is the near wall treatment. In the construction of this numerical model, the enhanced wall treatment is

chosen over the standard wall functions because it allows for more accurate modeling of the boundary layer while reducing the computation time. This is achieved because of the enhanced wall treatment inherent flexibility in the spatial resolution of mesh along all walls of the model. The enhanced wall model treatment is further described in the manual for the ANSYS™ FLUENT® software [48]. Overall, it was concluded that the RKE turbulence model with enhanced wall treatment is the most appropriate choice for this geometry.

Using the experimental measurements taken, the mass flow inlet and pressure outlet coolant boundary conditions are defined. In addition, measurements acquired for the coolant inlet temperature are used as an input parameter. For the κ-ε model, the parameter κ, the turbulent kinetic energy, must also be defined at both boundaries as given by Equation 26.

$$\kappa = \frac{3}{2}\left(V_{avg} I\right)^2 \tag{26}$$

Where V_{avg} is the average velocity at the boundary and I is the turbulence intensity defined by Equation 27 and 28, respectively.

$$V_{avg} = \frac{\dot{m}}{\rho_b A_b} \tag{27}$$

$$I = 0.16(Re_b)^{-1/8} \tag{28}$$

Where $\dot{m}$ is the mass flow rate, A_b is the cross sectional area at the boundary, ρ_b is the density of the coolant at the boundary, and Re_b is the Reynolds number evaluated at the boundary using the hydraulic diameter. Similarly, the parameter ε, the turbulent dissipation rate, must be defined at both boundaries as described by Equation 29.

$$\varepsilon = C_{\mu}^{3/4} \frac{\kappa^{3/2}}{l} \tag{29}$$

Where C_{μ} is an empirical constant approximately equal to 0.09, κ is the turbulent kinetic energy at the boundary, and l is the turbulence length defined by Equation 30.

$$l = 0.07L \tag{30}$$

Where L is the hydraulic diameter at the boundary.

A mesh convergence analysis was conducted to determine the minimum number of cells needed in the model to achieve mesh-independent results. The effective number of cells is determined by conducting a comparative study for various mesh-elements sizes ranging from 15×10^3 to 100×10^3 mesh-elements. The reference case study was conducted at steady-state for an incident heat flux of 2.65 MW/m^2. All other simulation details, such as the system setup and k-ε model input parameters, are the same as those for the transient case provided in Table 2. One of the most important results in these simulations is the temperature distribution along the cooled surface, also referred to as the impingement region. The temperature distribution along the cooled surface for the various meshes are plotted simultaneously in Figure 9. As the number of mesh-elements increases, the numerical prediction for the temperature distribution initially decreases in magnitude before showing no apparent dependence on mesh size for grids greater than 27,053 elements (mesh 3). Therefore, this was the mesh selected for the simulation of Gen 1 sample holder as it minimized the already computationally expensive transient simulations required for the characterization of the experiments.

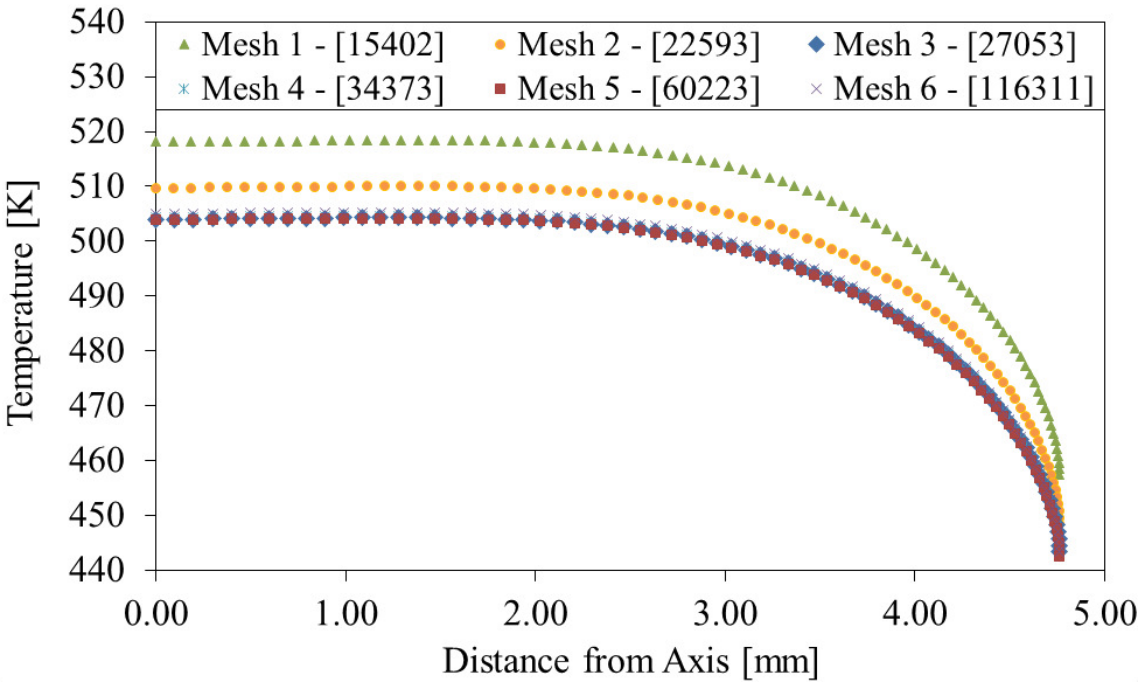

Figure 9. Temperature distribution along cooled surface for Gen 1 model showing mesh convergence after mesh 3 with 27,053 elements

The mesh selected is comprised of different cells types and sizes as depicted in Figure 10 and presented in Table 3. The values provided for the water and Cu-rod are maximum cell values imposed via the face sizing feature available in ANSYS™ Meshing. In most of the model, triangles were chosen instead of quadrilateral elements, since unstructured tetragonal meshes tend to perform better (have lower skewness values) for complex geometries.

Table 3. Mesh characteristics for the various regions in the Gen 1 sample holder

Location	Cell Type	Number of Cells	Cell Size [µm]
Mo-holder	Quadrilateral	2,596	484
Air Gap	Quadrilateral	467	140
Cu-rod	Triangular	9,551	1000
Water	Triangular	12,881	750
SS-cartridge	Triangular	1,528	253

A size function was applied to the face mesh along the cooled surface to allow a fine mesh in the region of high velocity gradients (near the jet stagnation point/impingement region) and a coarser mesh as the velocity gradients decrease (away from the impingement area and narrow side channel). Another size function used was the inflation layer feature. The inclusion of inflation layers along the solid walls, in contact with the fluid, allow for more accurate characterization of the boundary layer development and for resolving the rapid variation of flow variables within the boundary layer region effectively [49].

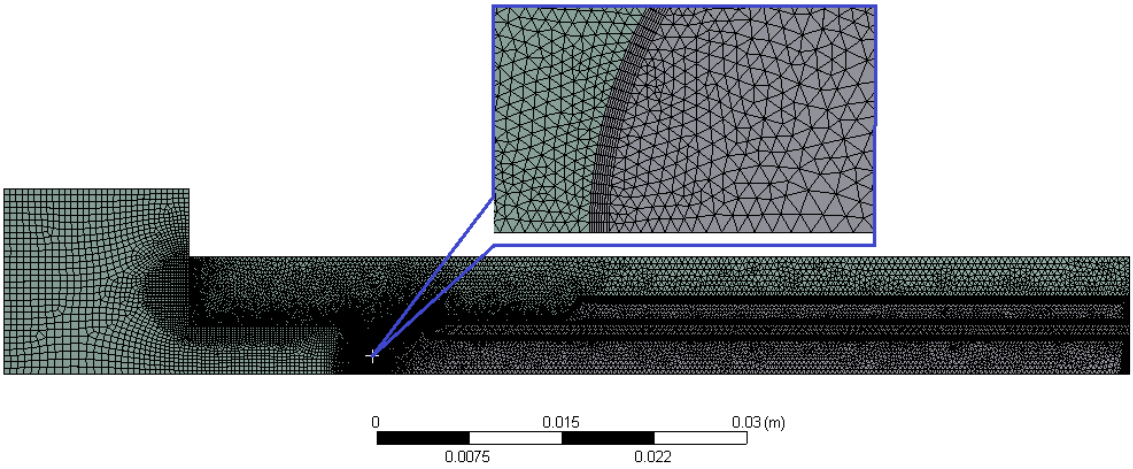

Figure 10. Gen 1 sample holder mesh and close-up on cooled surface showing inflation layers at the Cu-rod to water interface

Although a mesh-independent and convergent model was developed to represent the steady state case presented by each of the five cycles composing the nominal case, when the simulations were performed in transient mode, an oscillatory trend in the predicted average value for the heat transfer coefficient along the cooled surface was observed. Therefore, a time-step analysis was performed in order to find the maximum time-step size needed to minimize the oscillatory behavior in the heat transfer coefficient such that its impact relative to the average value would be negligible. The effect of the

time-step size on the heat transfer coefficient oscillation is plotted in Figure 11 for time-step sizes ranging from 2 ms to 100 ms. As the time-step size decreases, the amplitude of oscillations decreases, while the heat transfer coefficient converges towards a value that appears invariant to further decreases in the time-step size. Detailed analysis showed that the 4 ms time-step predicts the heat transfer coefficient within 1.5 % of the final converged value. Therefore, this was the time-step selected for the transient simulation of the Gen 1 sample holder as it minimized the already computationally expensive transient simulations required for the characterization of the experiments.

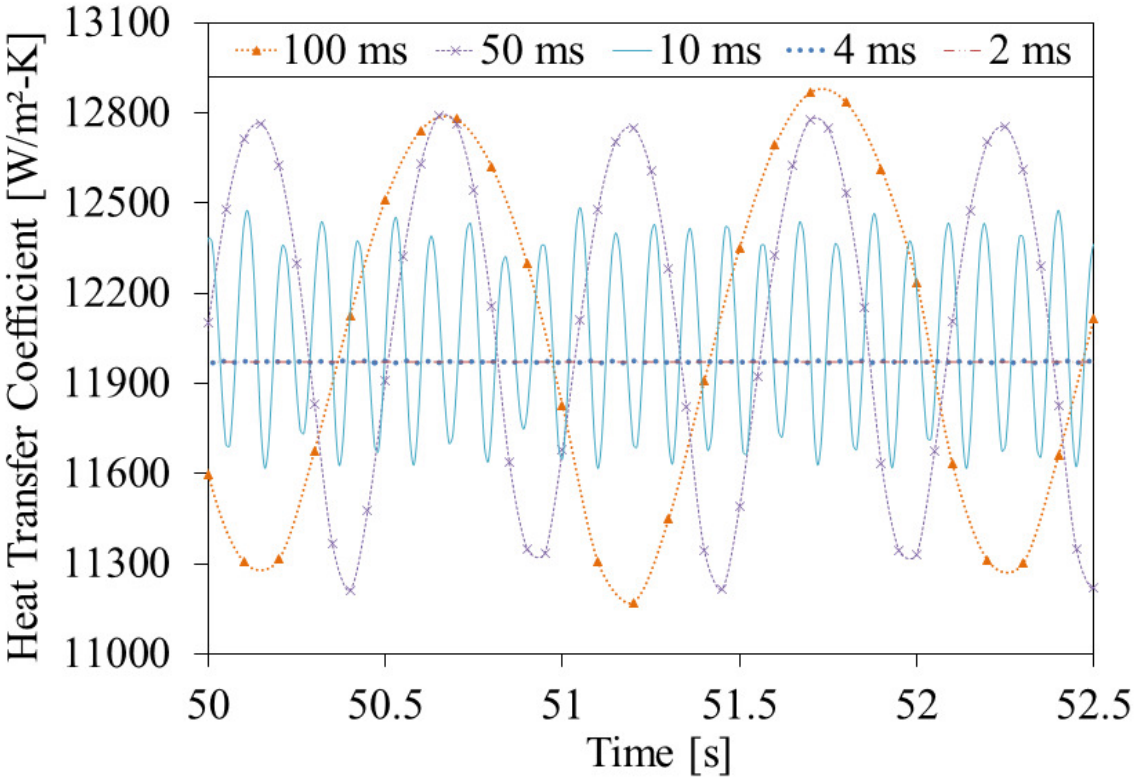

Figure 11. Time step analysis for modeling of Gen 1 sample holder in transient mode

As described throughout this section, the numerical model developed for representation of the Gen 1 sample holder is mesh-independent, fully converged, and free from numerical oscillations. In order to experimentally validate the model described above, the numerical predictions from the model are compared against the experimental data

presented in the literature for the nominal transient case [5]. Specific details pertinent to the nominal transient case such as; testing system conditions, and k-ε model input parameters are provided in Table 2. Validation and discussion of the results is provided in the following section.

3.1.2 Model Validation for Nominal Transient Case

The model developed for the Gen 1 sample holder is now used to simulate the nominal transient case incorporating all setup and input parameters given in Table 2. The results obtained from the simulation are compared against experimental data provided by Dr. A. S. Sabau from the Material Science & Technology Division at ORNL [46]. The experimental data is comprised of temperature and hydraulics measurements. Specifically, all data are related to testing conducted corroborating the readiness of the IMTS facility at ORNL [5]. In the experiment conducted, four thermocouples were used to sample data at a rate of 0.1 seconds. One thermocouple was located in the Mo-holder, two thermocouples at the same axial height and different angular location were embedded in the Cu-rod, and one thermocouple was located below the coolant outlet channel. Detailed dimensional drawings for the sample holder geometry and its thermocouple locations can be found in Appendix A. The data collected by the thermocouple located at the coolant outlet is the first experimental result used for validation of the numerical model. As depicted in Figure 12, the comparison of the experimental and simulation results shows reasonable agreement with an estimated 0.52 % mean difference.

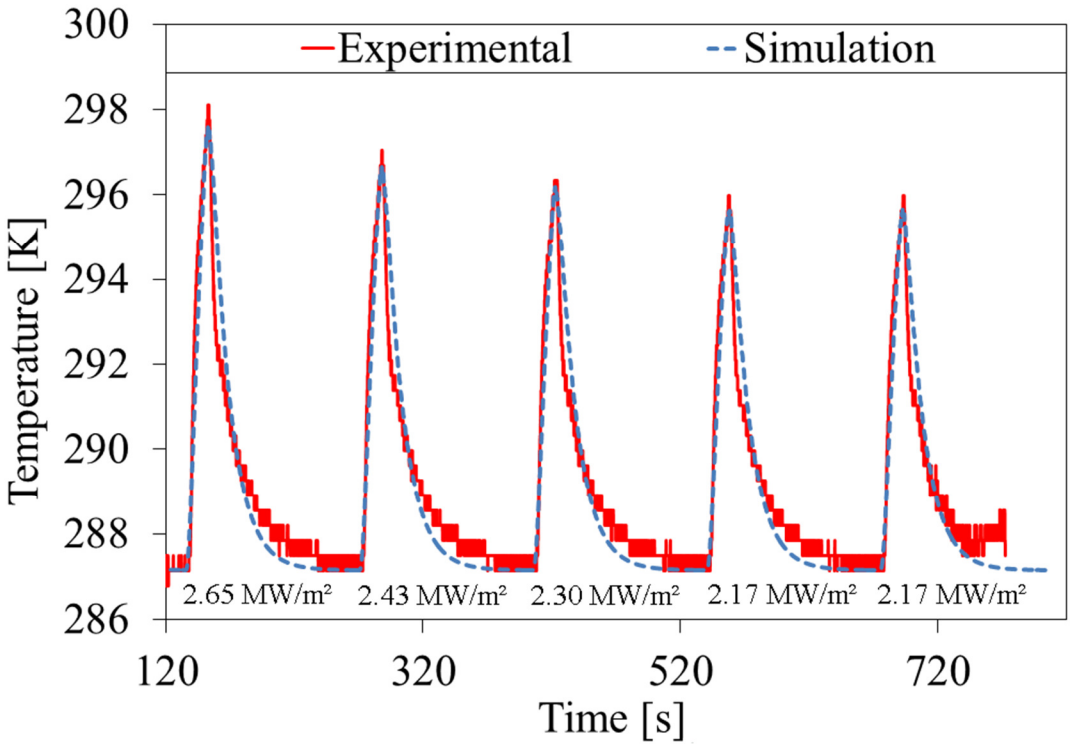

Figure 12. Outlet temperature comparison of experimental results against simulation prediction for Gen 1 sample holder

Although the trend is closely predicted, differences in the temperature gradient during the cooling period (temperature drop) can be attributed to the adiabatic boundary assumption as no heat losses to the environment are considered. Even though no uncertainty related to the thermocouples measurements were provided in the literature, the results suggest that the simulation predictions are within the range of uncertainty related to the thermocouple located at the coolant outlet (~ ± 1 °C). Therefore, the adiabatic boundary assumption used in the model is reasonably accurate.

With the purpose of further evaluating how closely the numerical model characterizes the Gen 1 sample holder, the experimental measurements collected by thermocouples embedded in the Cu-rod are compared to the results predicted by the simulation. As presented in Figure 13, the results for the two thermocouples embedded in

the Cu-rod are plotted simultaneously with average value obtained from the numerical model.

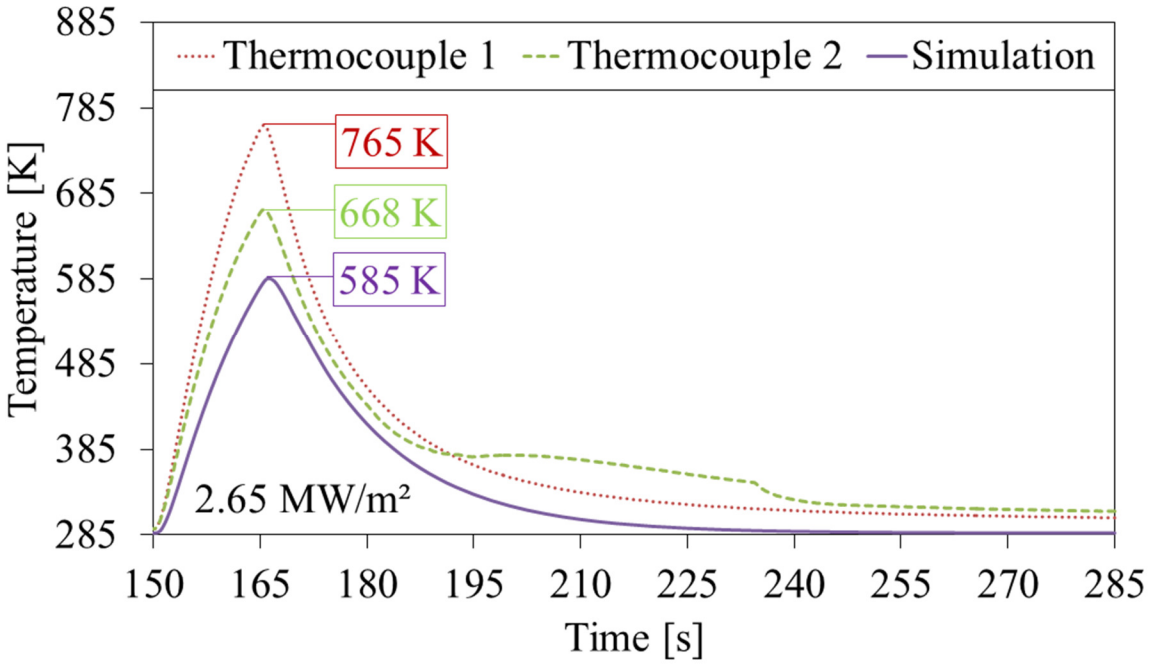

Figure 13. Comparison of experimental results against simulation prediction for Cu-rod thermocouple for Gen 1 sample holder

A significant deviation between the two thermocouple readings is observed as the temperature rises. For the peak temperature values, there is a difference of approximately 100 °C. A plausible explanation for this discrepancy is the uncertainty related to the location where the tip of the thermocouple probe makes contact with the Cu-rod (inside the thermocouple holes). Since the thermocouple holes have a diameter of 3.5 mm, the temperature gradient between the top and bottom of the holes may be substantial. Therefore, the temperature difference reported for the two experimental thermocouple readings could be plausible. As depicted in Figure 13, there is a discrepancy between the temperature predicted by the simulation and the experimental data. The mean difference for the peak temperature values predicted by the simulation and the thermocouple readings is approximately 130 °C. This large deviation may be due to the uncertainty related to the

incident heat flux measurement and the estimate provided for heat flux absorbed by the sample holder. Although the reported estimate in the heat flux measurements is ± 2 %, simulation results suggest that the uncertainty could be as large as ± 20 % in which case the temperatures predicted by the simulation would be in agreement with the experimental results. This deviation would have little impact on the predicted coolant exit temperature as noted in Figure 12 above.

Throughout this section the numerical model developed for the Gen 1 sample holder was presented and good agreement with the experimental data available for the coolant thermocouple reading was shown. Also, justifiable discrepancy with experimental data provided for the Cu-rod thermocouples was presented. Overall, the idealization and assumptions associated with the numerical model in addition to the uncertainties related to the experimental data suggest that further validation of the model would be necessary to fully characterize the nominal transient case. Nevertheless, the numerical model is still a valid tool for parametric design and thermal performance evaluation, provided that, the effects of the assumptions made in the development of the model are taken into account. In the next chapter, a parametric study evaluating the thermal performance of the Gen 1 sample holder is performed. The numerical model is used for analyzing parameters, such as maximum allowable temperatures of the sample holder components, in order to establish safe limits of operation during HHF testing.

3.2 Numerical Modeling of Gen 2 Sample Holder

The need to increase the limits of operation for HHF testing entails the consideration of other sample holder designs. To that end, significant changes were made in the geometry of the Gen 2 sample holder when compared to the Gen 1 sample holder. It is a fundamental goal to understand the effects that geometric changes have in thermal performance and the possibilities for further optimization. In this section, the Gen 2 sample holder design is presented and validation of its numerical model is conducted. In addition, a brief analysis of a relevant geometric parameter for the sample holder design is considered.

3.2.1 Problem Setup

The Gen 2 sample holder, shown in Figure 14, was used during a second round of HHF experiments conducted at the IMTS facility located at ORNL. This is the second sample holders design considered in this thesis. It is comprised of a Molybdenum holder (Mo-holder), a Molybdenum clamping disk (Mo-clamp), a Copper cooling rod (Cu-rod), a stainless steel jet cartridge (SS-cartridge), and a bi-metallic sample formed by Tungsten and FH82-steel (W-FH82-sample). The materials used in the fabrication of this sample holder were the same as those utilize for the Gen 1 sample holder except for the FH82 in the W-F82H-sample which was used to improve material compatibility between the Tungsten sample and the Mo-holder. There is no thermal contact resistance between W and F82H as these surfaces are metallurgically bonded [47].

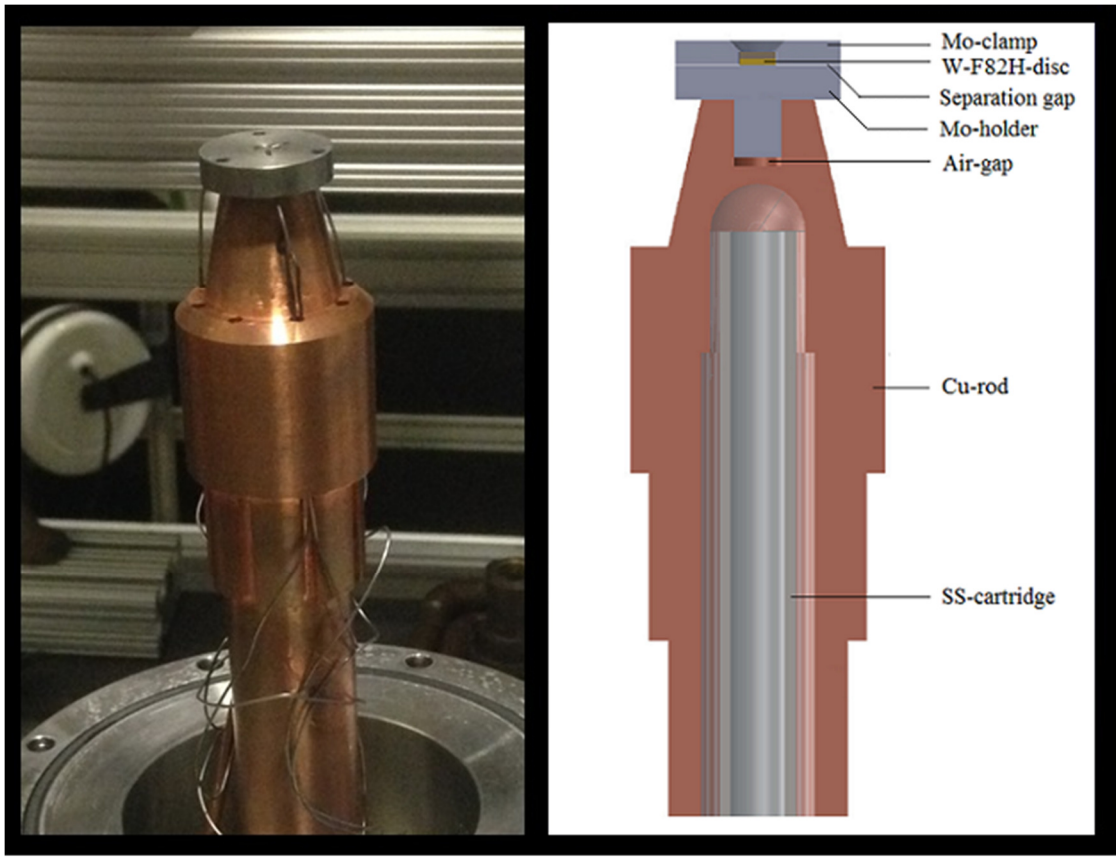

Figure 14. Gen 2 sample holder composed of clamping disk, water-cooled rod, Mo-Holder, and thermocouples.

A 2D axisymmetric model was developed, using the ANSYS™ DesignModeler® tool. As depicted in Figure 15, the model consists of the Mo-holder, Cu-rod, SS-cartridge, and W-F82H-sample. In order to account for the effects of the two materials composing the bi-metallic sample, the W-F82H-sample piece was modeled as two separate elements, W-disk and F82H-disk, with no contact resistance between them. In addition, three air gaps measured during experiments were included in the model: an air-gap of 1.4 mm between the bottom of the Mo-holder insert and the Cu-rod threaded cavity, an air-gap of 150 μm between the W-F82H-sample and the Mo-clamp (around the sample), and an air-gap of 44 μm between the Mo-clamp and Mo-holder [47]. In the model, all outer surfaces on the solid body were assumed to be adiabatic except the five faces where the heat flux is incident.

Furthermore, the effect of the contact resistances between; the Mo-holder and the Cu-rod, the F82H-disk and the Mo-holder, the W-disk and the Mo-clamp, were assumed to be negligible. As discussed by Sabau (2014), the heat flux profile of the PAL can be assumed to be uniform [5]. Table 4 presents the list of experimental parameters, including the incident heat fluxes, used during HHF testing for the Gen 2 sample holder [47].

Table 4. Setup and input parameters for nominal transient case of the Gen 2 sample holder

Testing Parameters						
Cycle Specifications	Cycle 1	Cycle 2	Cycle 3	Cycle 4	Cycle 5	Cycle 6
Heat Flux [MW/m^2]	1.505	1.505	1.505	1.413	1.413	1.413
Irradiation Time [s]	25	25	25	25	25	25
Dwell Time [s]	88.2	78.5	74.9	90	90	90
System Parameters						
Pressure [psi]	80					
Mass Flow Rate [kg/s]	0.348					
Coolant Inlet Temperature [K]	281.48					
k-ε Model Input Parameters						
Boundary	Inlet			Outlet		
Turbulent Kinetic Energy 'k'	7.73×10^{-2}			1.65×10^{-2}		
Turbulent Dissipation Rate 'ε'	5.54×10^{0}			7.75×10^{-1}		

In addition, nearly 10 percent of the incident heat flux was measured to be absorbed by the cylindrical side wall of the Mo-clamp and Mo-holder (perpendicular to the PAL) [47]. Due to the large temperature gradients that are expected within the solids, for the range of experimental heat fluxes, the temperature dependence of the material properties

was included. The evaluation of the physical properties for F82H-steel and their variation with temperature are provided according to study conducted by Tavassoli et al. [49]. A detailed compilation of the temperature dependent properties for all materials is available in Appendix B. In addition, the User Defined Function (UDF) created as a materials input for ANSYS™ FLUENT® is included in Appendix C.

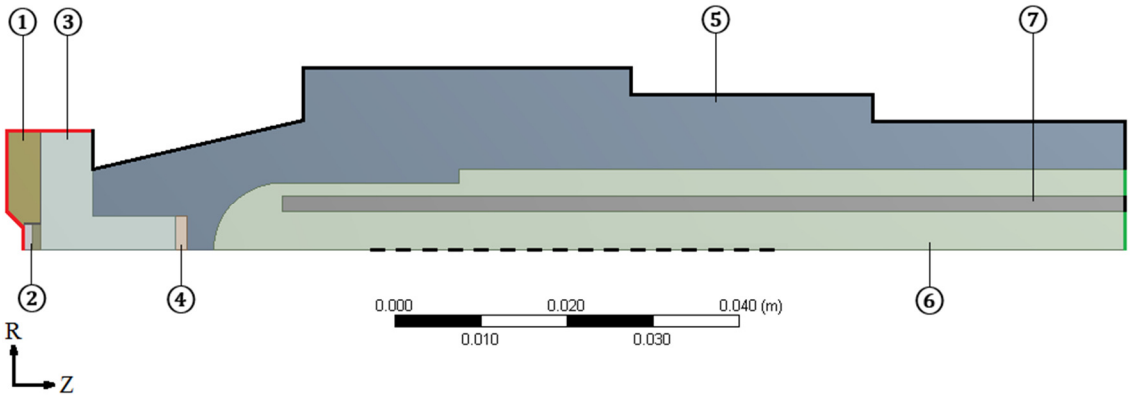

Figure 15. 2D axisymmetric model used in the Gen 2 sample holder CFD analysis composed by Mo-clamp ①, W-F82H-disc ②, Mo-holder ③, air-gap ④, Cu-rod ⑤, coolant ⑥, and SS-cartridge ⑦. Solid black lines indicate adiabatic boundary conditions, red lines indicate heat flux boundary condition, green lines indicate coolant boundary conditions (mass flow inlet or pressure outlet depending on the direction of flow), dash black line indicates symmetry axis 'Z' and the radial direction is indicated by the 'R' axis

The turbulence model was chosen based on the similarity of the geometry and flow characteristics of the Gen 2 sample holder and those for the Gen 1 sample holder design. Therefore, it was concluded that the RKE turbulence model with enhanced wall treatment is also the most appropriate model to characterize the Gen 2 sample holder.

A mesh convergence analysis was conducted to determine the minimum number of cells needed in the model to achieve mesh-independent results. The effective number of cells is determined by conducting a comparative study for various mesh-elements sizes ranging from 27×10^3 to 148×10^3 mesh-elements. The reference case used in the mesh

converge study was conducted at steady-state. All specific details such as system setup and k-ε model input parameters are provided in Table 5.

Table 5. Input parameters for mesh convergence reference case of the Gen 2 sample holder

System Parameters		
Heat Flux [MW/ m^2]	1.0	
Pressure [psi]	80	
Mass Flow Rate [kg/s]	0.032	
Coolant Inlet Temperature [K]	281.48	
k-ε Model Input Parameters		
Boundary	Inlet	Outlet
Turbulent Kinetic Energy 'k'	4.42×10^{-3}	9.68×10^{-4}
Turbulent Dissipation Rate 'ε'	1.08×10^{-1}	1.48×10^{-2}

One of the most important results in these simulations is the temperature distribution along the cooled surface, also referred to as impingement region. The temperature distribution along the cooled surface for the various meshes are plotted simultaneously in Figure 16.

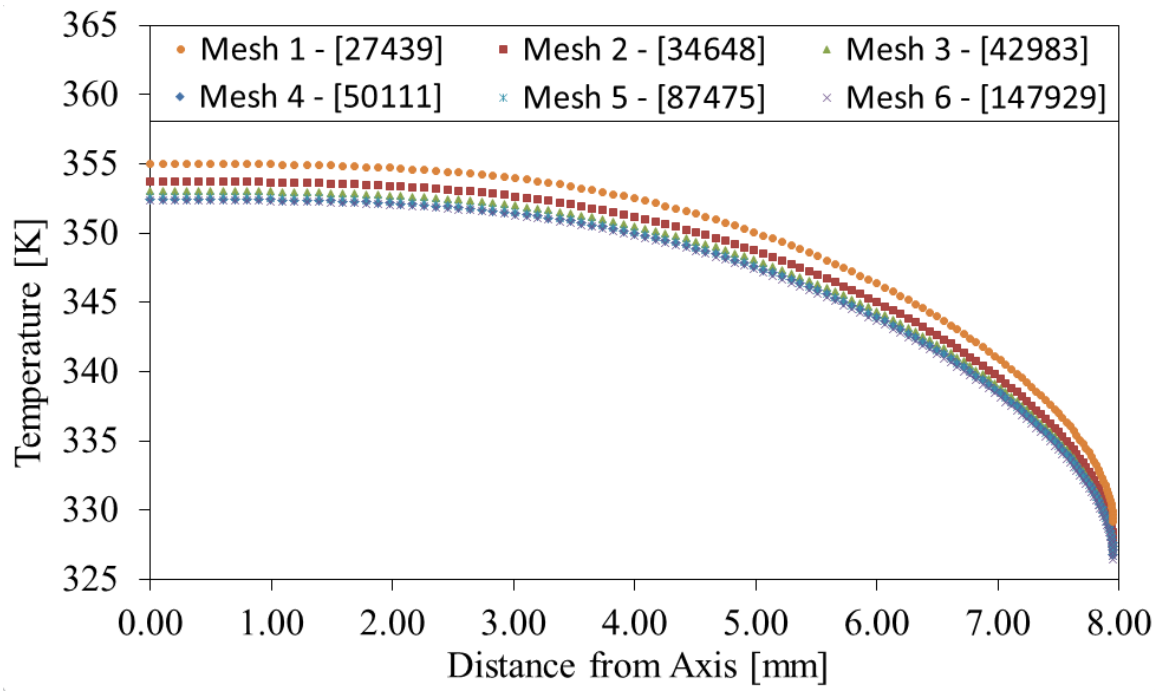

Figure 16. Temperature distribution along cooled surface for Gen 2 model showing mesh convergence after mesh 4 with 50,111 elements

As the number of mesh-elements increases, the numerical prediction for the temperature distribution converges towards a set trend that appear invariant to further increases in mesh-elements, suggesting that the mesh has already converged at 50,111 elements (mesh 4). Mesh 4 was the mesh selected for the simulation of Gen 2 sample holder as it minimized the already computational expensive transient simulations required for the characterization of the experiments. The mesh selected is comprised of different cells types and sizes as depicted in Figure 17 and presented in Table 6. The values provided for the water and Cu-rod are maximum cell values imposed via the face sizing feature available in ANSYS™ Meshing. In most of the model, triangles were chosen instead of quadrilateral elements, since unstructured tetragonal meshes tend to perform better (have lower skewness values) for complex geometries.

Table 6. Mesh characteristics for the various regions in the Gen 2 sample holder

Location	Cell Type	Number of Cells	Cell Size [μm]
Mo-clamp	Triangular	1,715	247
W-disk	Quadrilateral	124	167
F82H-disc	Quadrilateral	140	143
Mo-holder	Quadrilateral	1,559	353
Air Gap	Quadrilateral	222	156
Cu-rod	Triangular	9,952	1000
Water	Triangular	28,798	750
SS-cartridge	Triangular	7,516	225

A size function was applied to the face mesh along the cooled surface to allow a fine mesh in the region of high velocity gradients (near the jet stagnation point/area of impingement) and a coarser mesh as the velocity gradients decrease (away from the impingement area and narrow side channel).

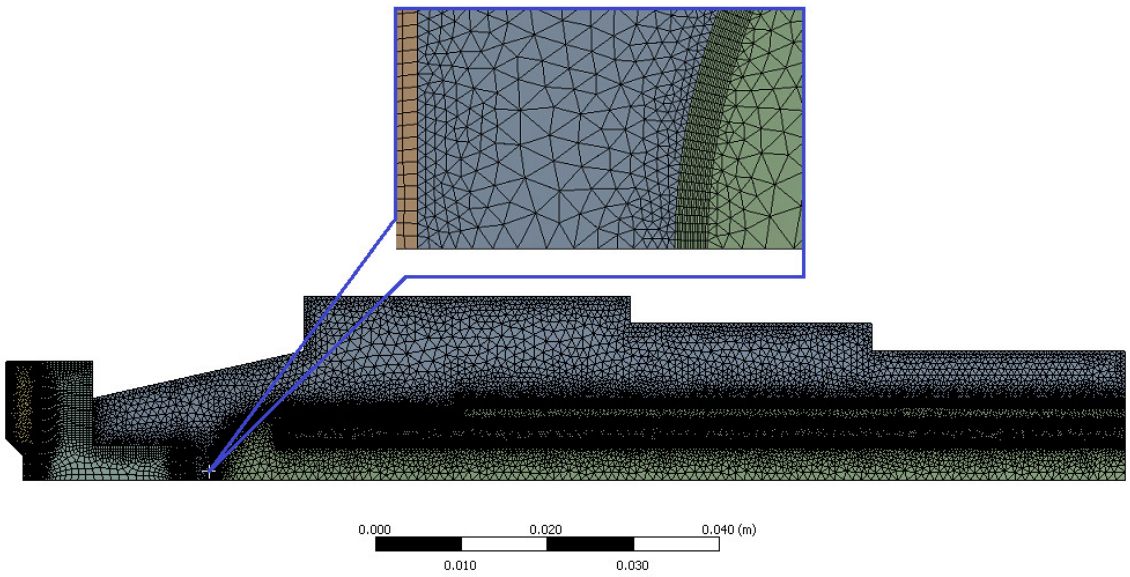

Figure 17. Gen 2 sample holder mesh and close-up on cooled surface showing inflation layers at the Cu-rod to water interface

Another size function used was the inflation layer feature. The inclusion of inflation layers along the solid walls, in contact with the fluid, allows for better depiction of the

boundary layer development and for resolving the rapid variation of flow variables within the boundary layer region effectively. Although a mesh-independent and convergent model was developed to represent the reference case in steady state mode, when the simulation was performed in transient mode, a dependence on the step-size was observed when predicting the average value for the heat transfer coefficient. Therefore, a time-step analysis was performed in order to find the maximum time-step size needed to find a convergent value. The effect of the time-step size on the heat transfer coefficient is plotted in Figure 18 for time-step sizes ranging from 10 ms to 100 ms.

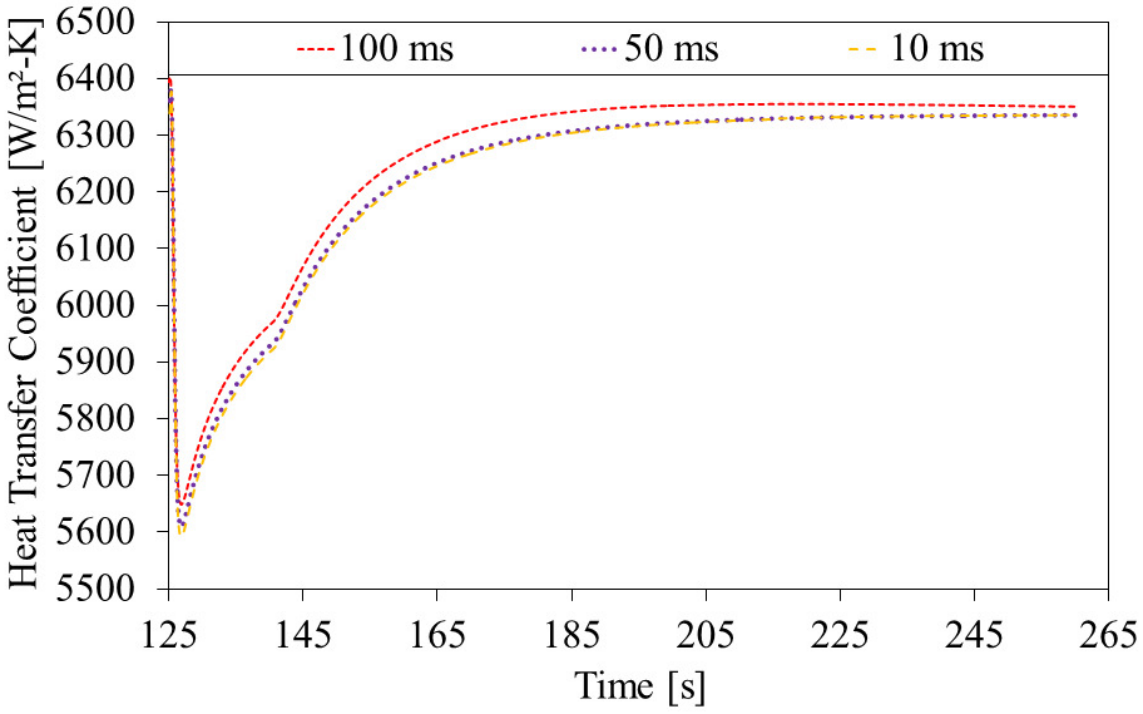

Figure 18. Time step analysis for modeling of Gen 2 sample holder in transient mode

As the time-step size decreases, the predicted value for the heat transfer coefficient converges towards a value that appears invariant to further decreases in the time-step size, suggesting that the maximum time-step size is about 50 ms. Detailed analysis showed that the 50 ms time-step predicts the heat transfer coefficient within 1.0 % of the final converged value. This was the time-step selected for the transient simulation of Gen 2 sample holder

as it significantly minimized the computationally expensive transient simulations required for the characterization of the experiments while providing accurate results (less than 1% mean difference).

As presented throughout this section, the numerical model developed for representation of the Gen 2 sample holder is mesh-independent, time-step independent, and fully converged. In order to experimentally validate the model described above, the numerical predictions resultant from the model are compared against the experimental data presented in the literature for the nominal transient case [47]. Specific details pertinent to the nominal transient case such as; testing, system, and k-ε model input parameters are provided in Table 4. Validation and discussion of the results is provided in the following section.

3.2.2 Gen 2 Model Validation for Nominal Transient Case

The model developed for the Gen 2 sample holder is now used to simulate the nominal transient case incorporating all setup and input parameters provided in Table 4. The results obtained from the simulation are compared against experimental data provided by Dr. A. S. Sabau from the Material Science & Technology Division at ORNL [47]. The experimental data provide a list of temperature and hydraulic measurements. In the experiment conducted, there were four thermocouples sampling data at a rate of 0.1 seconds. Two thermocouples were embedded at different locations in the Mo-holder, one thermocouple was located in the Cu-rod, and one thermocouple was positioned below the coolant outlet channel. Detailed dimensional drawings for the sample holder geometry and its thermocouples locations can be found in Appendix A. The data collected by the thermocouple located at the coolant outlet is the first experimental result used for validation

of the numerical model. As depicted in Figure 19, the comparison of the experimental and simulation results shows discrepancies on the peak values with an estimated 45.5 % mean difference when considering the temperature change between inlet and exit.

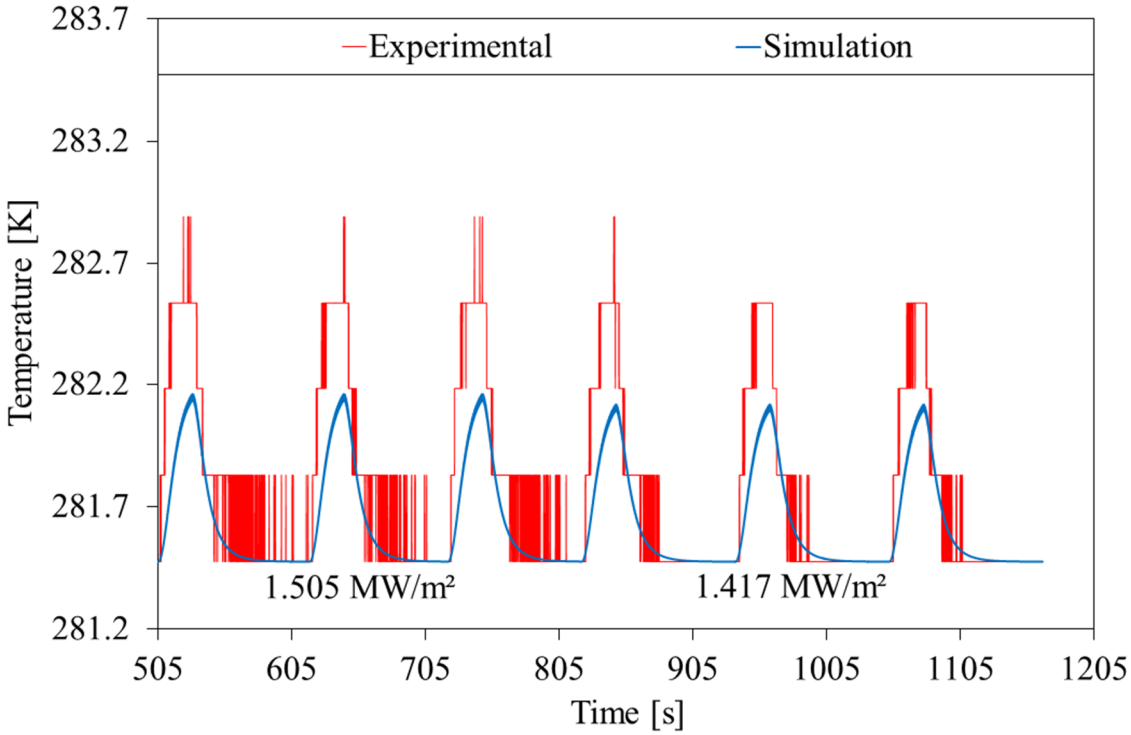

Figure 19. Outlet temperature comparison of experimental results against simulation prediction

Due to the small change in temperature between inlet and outlet, it is difficult to draw definite conclusions from the discrepancy observed between experimental and simulation results. As observed in Figure 19, the temperature change, per experimental data in the first three cycles, is approximately 1.4 °C whereas the change for the simulation is about 0.74 °C. Although the apparent difference between the two values is seemingly large, the simulation predictions may still be quite reliable as it is within the range of uncertainty expected with the thermocouple readings (~ ±1°C). Unfortunately, no calibration data or uncertainty pertinent to this specific thermocouple has been recorded in the ORNL data. Therefore, it would be necessary to further evaluate the model against

experimental data showing larger temperature gradients where small discrepancies (less than 1 °C) are within acceptable range of results.

With the purpose of evaluating further how the numerical model characterizes the Gen 2 sample holder, the experimental measurements collected by thermocouple embedded in the Cu-rod is compared to the results predicted by the simulation. As presented in Figure 20, the results for this thermocouple are plotted simultaneously with average value obtained from the numerical model.

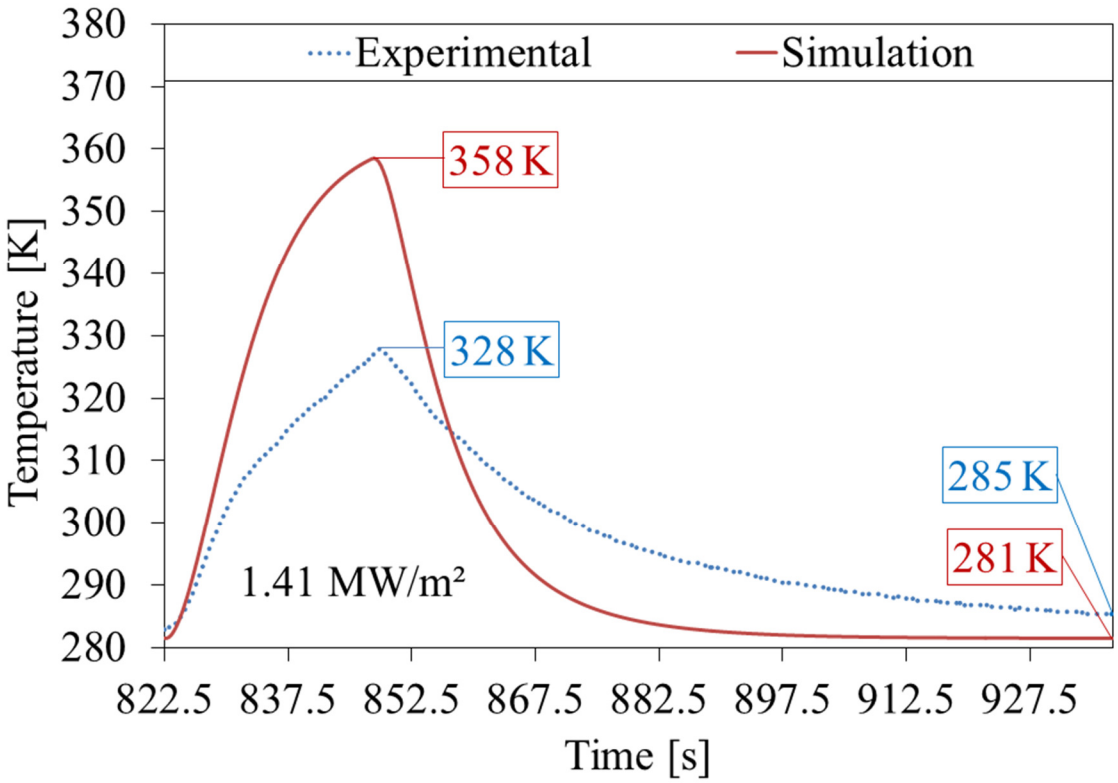

Figure 20. Comparison of experimental results against simulation prediction for Cu-rod thermocouple for Gen 2 sample holder

The approximate difference observed between experimental and simulation results is about 30 °C for the peak values. Due to the assumptions made in the development of the numerical model, the difference observed between the experimental and simulation results is expected. By neglecting the effects of contact resistance at the Mo-holder and Cu-rod

interface, in the idealized model, the heat is able to rapidly diffuse and travel down the length of the sample holder without any opposition, thus, the recorded temperatures in the Cu-rod are higher than in the opposite case, where contact resistance is considered, for the transient interval during the irradiation period. In the non-ideal model, the contact resistance acts as an added thermal resistance limiting the heat transfer between the Mo-holder and the Cu-rod, therefore, lower temperatures are recorded in the Cu-rod. Another assumption, the adiabatic boundary condition, contributes to the discrepancy observed in the results. Since no heat losses are taken into consideration, the avenues by which the heat travels as it diffuses are limited. The energy contained within the bounded system can only be removed by conduction along the sample holder. Therefore, higher temperatures along the Cu-rod are predicted in the idealized model.

Another effect of the contact resistance is observed at the end of the transient cycle when the temperatures recorded by the Cu-rod thermocouple are consistently higher than those predicted by the numerical model. This behavior is a result of the time delay in the energy transfer between the Mo-holder and the Cu-rod caused by the thermal resistance. As more energy is held upstream, the temperatures recorded by the Cu-rod thermocouple are higher at the end of cycle. In other words, it would take a longer dwell period for the heat to be fully removed. The effects of these two assumptions are also reflected in the experimental data recorded for the two thermocouples embedded in the Mo-holder depicted in Figure 21 (Bolted-Thermocouple) and Figure 22 (Unbolted-Thermocouple).

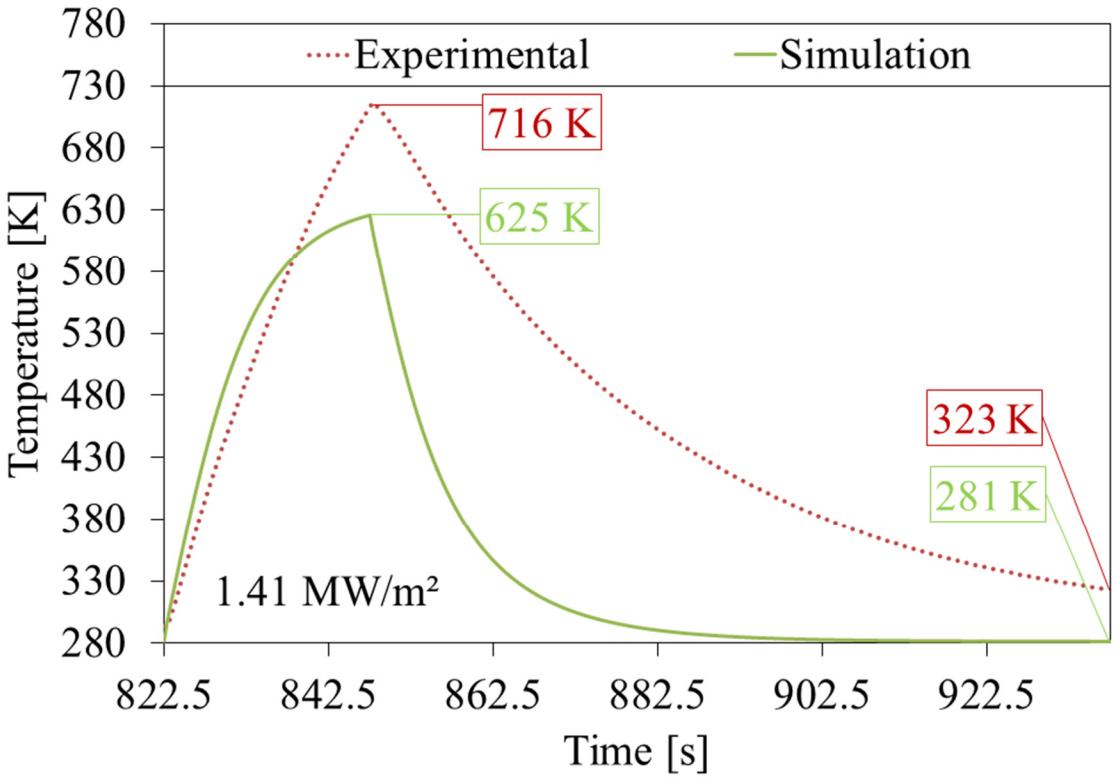

Figure 21. Comparison of experimental results against simulation prediction for Mo-holder bolted-thermocouple for Gen 2 sample holder

The temperatures predicted by the numerical model are approximately 100 °C lower than those measured experimentally by the Mo-holder thermocouples. The lower predicted temperatures may be attributed in part to ignoring of the contact resistance at the Mo-holder and Cu-rod interface. Analysis conducted using the numerical model suggested that inclusion of a contact resistance equivalent to a 1 μm gap distance of air between the Mo-holder and the Cu-rod would increase the temperature within the Mo-holder to values comparable to the experimental values recorded by the Mo-holder thermocouples. The contact resistance pertinent to the interface between the F82H-disk and the Mo-holder was assumed negligible in the numerical model. The effect of this assumption is reflected at the start of the cycle, depicted in Figure 21 and Figure 22, where a rapid rise in the temperature

is shown, for the simulation results, leading to a change in the temperature difference as the irradiation period ends.

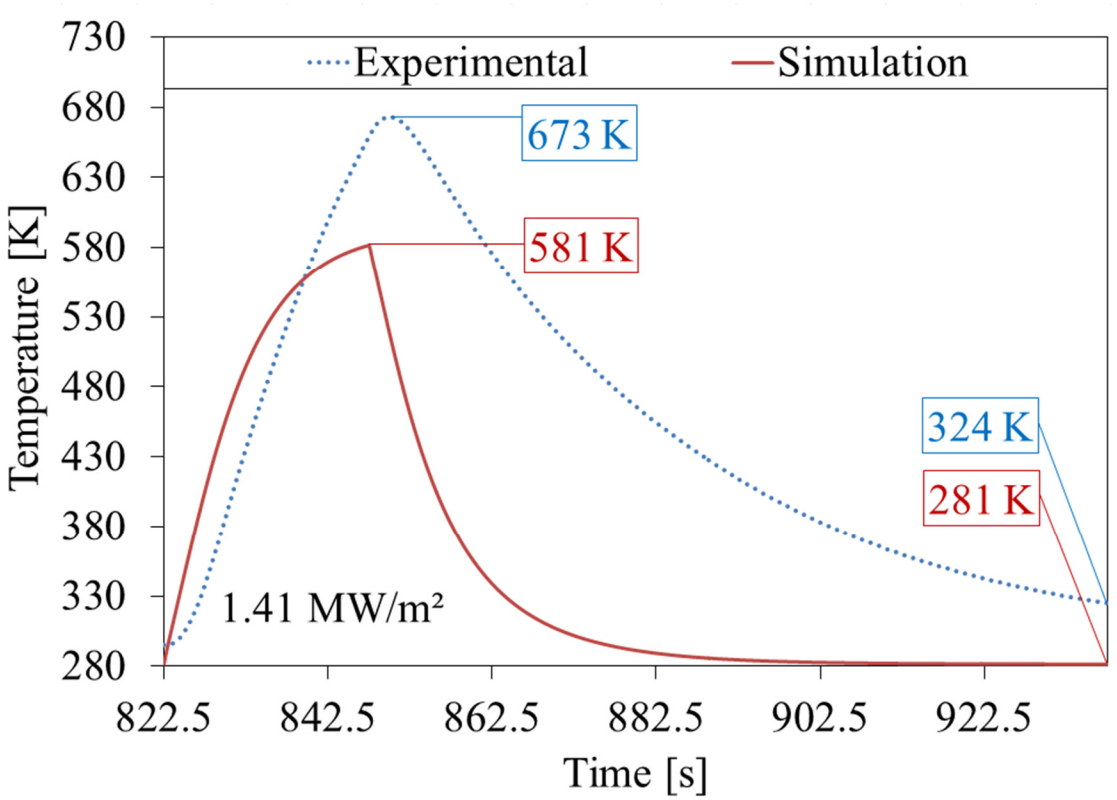

Figure 22. Comparison of experimental results against simulation prediction for Mo-holder unbolted-thermocouple for Gen 2 sample holder

In contrast, a time delay is observed initially in experimental results, more pronounced in the unbolted thermocouple data (Figure 22), which then rises at a constant rate until the end of the irradiation period is reached. As previously discussed, the heat is removed more efficiently in the ideal model causing the initial temperature condition to be obtained within the dwell period (at the end of the cycle). On the contrary, reflected in the experimental results, the impact of the contact resistances is most likely manifested in a significant delay in heat removal, thus, recording higher temperature in the Mo-holder at the end of the cycle.

In addition to the effects of contact resistance, the gap distance between the Mo-clamp and the Mo-holder significantly affects the temperature and heat flux distribution along the sample holder. Although the contact resistance effects were not considered in the ideal model, the effects of the gap distance were evident in the numerical simulations. A significant shift in the temperature, concentrated at the center of the Mo-holder, was observed as a result of the gap distance. Therefore, it is safe to conclude that the noted difference between the experimental Mo-holder thermocouple readings and the corresponding numerical values are a reflection of the contact resistance and gap distance. A detailed study of the effects of gap distance is conducted in the next chapter.

Throughout this section the numerical model developed for the Gen 2 sample holder was presented and its numerical predictions were compared against available experimental thermocouple data. Overall, the idealization and assumptions associated with the numerical model in addition to the uncertainties related to the experimental data suggest that further validation of the model would be necessary to fully characterize the nominal transient case. Nevertheless, the numerical model is still a valid tool to conduct a parametric study for thermal performance evaluation, provided that, the effects of the assumptions made in the development of the model are taken into account. In the next chapter, a parametric study to evaluate the thermal performance of the Gen 2 sample holder is performed. The numerical model is used for analyzing the effect of various parameters on the peak temperatures of the sample holder components, in order to establish safe limits of operation during HHF testing.

CHAPTER 4: THERMAL PERFORMANCE EVALUATION

4.1 Sample Holders Nominal Case Thermal Performance Evaluation

The numerical models described in the previous chapter for each of the sample holders were then used to determine the temperature distribution and local heat transfer coefficients at different times during the irradiation periods. This chapter presents these results.

4.1.1 Gen 1 Sample Holder Nominal Case

The heat transfer coefficient (HTC) as a function of the radial distance from the symmetry axis over the cooled surface predicted by FLUENT for the Gen 1 sample holder are shown every second over the 15 s irradiation period and the first 5 s of the dwell period following the irradiation period for the nominal case are shown in Figure 23. These results are over the first irradiation cycle, with a uniform power of 2.65 MW/m^2, of the nominal case. The simulation results indicate that the local HTC distribution along the cooled surface was similar over all five cycles, within the similar values for the HTC at a given location and a given time within the irradiation cycle.

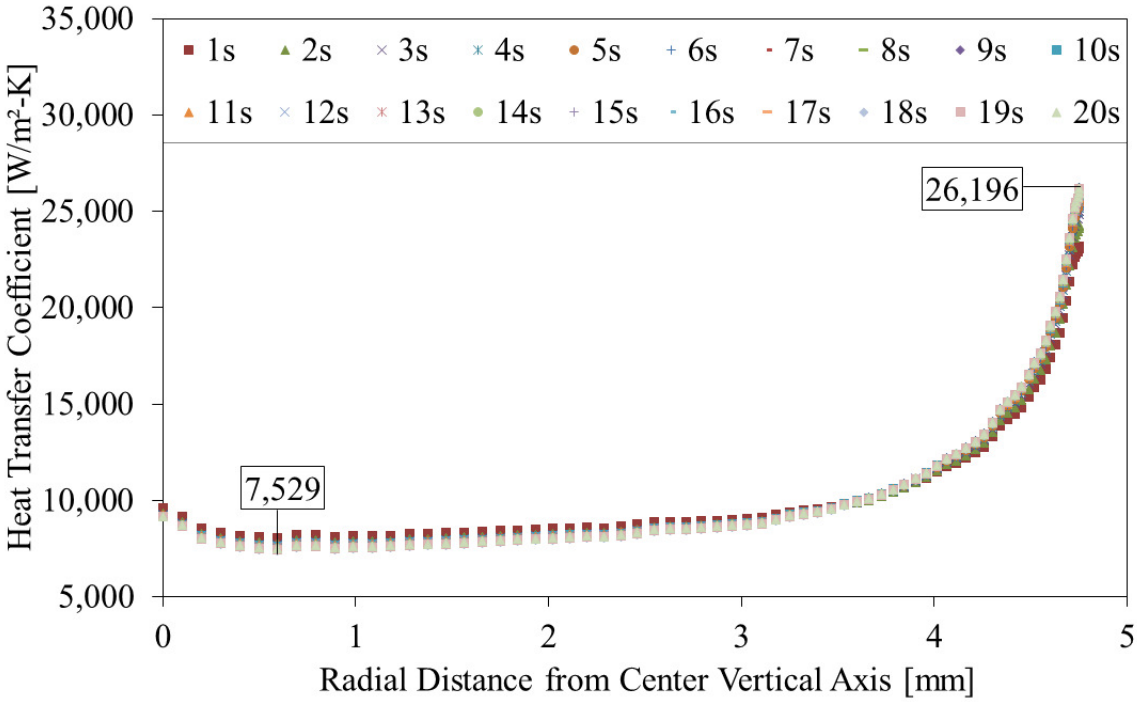

Figure 23. Heat transfer coefficient distribution along cooled surface for the first cycle of the Gen 1 sample holder nominal case

The HTC results for the four irradiation cycles are therefore provided in Appendix D. The small variations in the HTC distribution along the cooled surface are due to the relative large time-steps used in these simulations. As shown in the previous chapter, these variations could be essentially eliminated by further decreasing the time step, but this was impractical because it would greatly increase computational times, so the results presented here were obtained with a time step of 4 ms. This relatively large time step will introduce at most a variation of 1.5% in the HTC. The maximum value of HTC (~ 2.62×10^4 W/m^2-K) occurs at the entrance of the narrow annular channels where the average coolant velocity is about 2 m/s, double the inlet velocity (1 m/s), for a mass flow rate of 32 g/s in the nominal case. The lowest value of HTC (~7.53×10^3 W/m^2-K) occurs near the stagnation point at a radial position of ~ 1 mm. As shown in Figure 24, which depicts the corresponding temperature profile along the cooled surface, the maximum surface temperatures are found

near the stagnation point, as expected because the coolant speed should be minimum in this region.

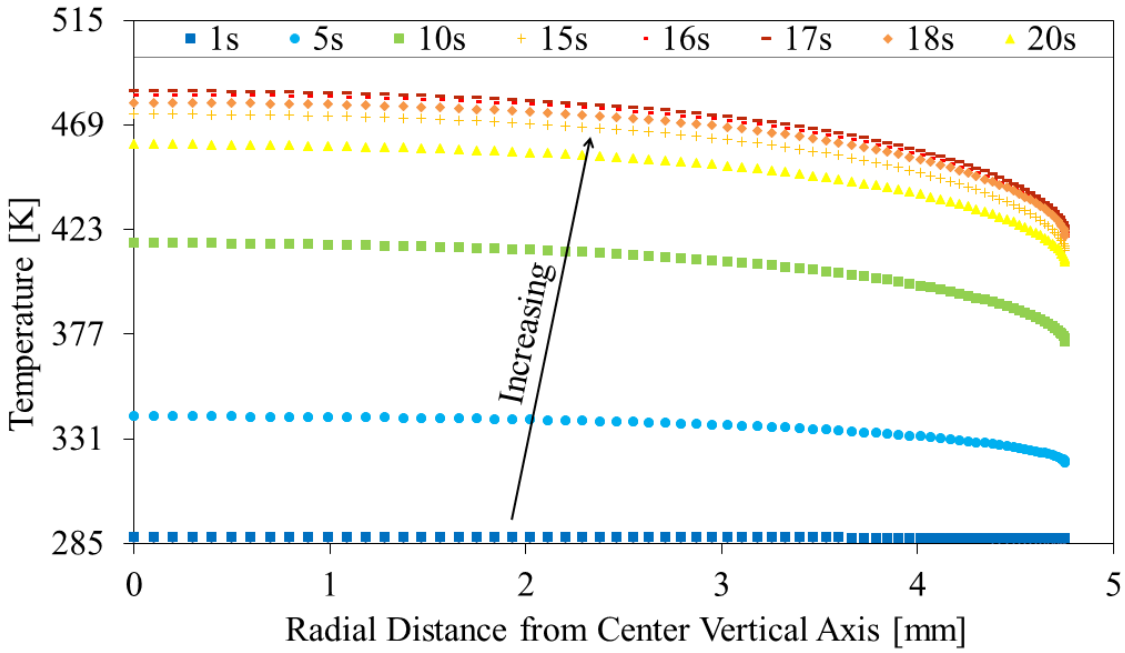

Figure 24. Temperature distribution along cooled surface for the first cycle of the Gen 1 sample holder nominal case

In Figure 24, the temperature distribution variation with time is depicted. The maximum surface temperature overall is about 484 K, at the end of the HHF irradiation period (~17 s). Note that the maximum temperature occurs two seconds after the irradiation period (15 s) has ended. This time delay correspond to the time it takes for heat to be conducted from the irradiation surface to the cooled surface. The surface temperature distribution for the other four cycles of this case are also given in Appendix D.

4.1.2 Gen 2 Sample Holder Nominal Case

Figure 25 shows the local HTC as a function of radial distance from the axis of symmetry at different times during the irradiation period of the nominal case for the Gen 2

sample holder. Results are shown for the 25 s HHF irradiation period (505.9-530.9 seconds) and the first 5 s of the 74-90 s dwell period (530.9-619.1 seconds).

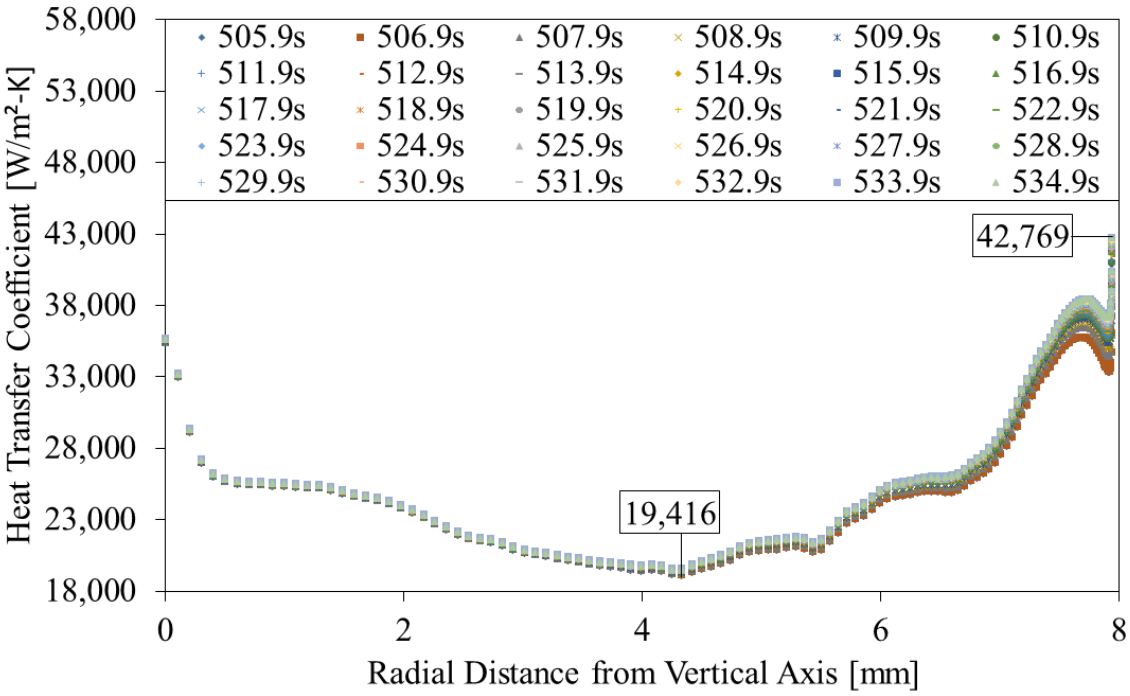

Figure 25. Heat transfer coefficient distribution along cooled surface for the first cycle of the Gen 2 sample holder nominal case

The small numerical variations observed in the HTC distribution along the cooled surface are due to the relatively large the time-step used in this simulations. As shown in the previous chapter, these variations could be essentially eliminated by further decreasing the time step, but this was impractical because it would greatly increase computational times, so the results presented here were obtained with a time step of 50 ms. This relatively large time step will introduce at most a variation of 1.0% in the HTC. The maximum value of HTC (~ 4.28×10^4 W/m^2-K) is reached at the entrance of the narrow annular channel where the average coolant velocity along the cooled surface is the greatest (~ 5.5 m/s). The lowest value of HTC (~1.94×10^4 W/m^2-K) occurs at radial position of ~ 4 mm. As shown in Figure 26, which illustrates the corresponding temperature profile along the cooled

surface, the maximum surface are found in the proximity of the stagnation point, as expected because the coolant speed should be a minimum in this region. The maximum surface temperature overall is about 344 K, at the end of the HHF irradiation period (~ 530.9 s) near the stagnation point. Plots indicating the HTC distributions and the temperature distribution for each cycle of the nominal case for the Gen 2 sample holder are provided in Appendix D.

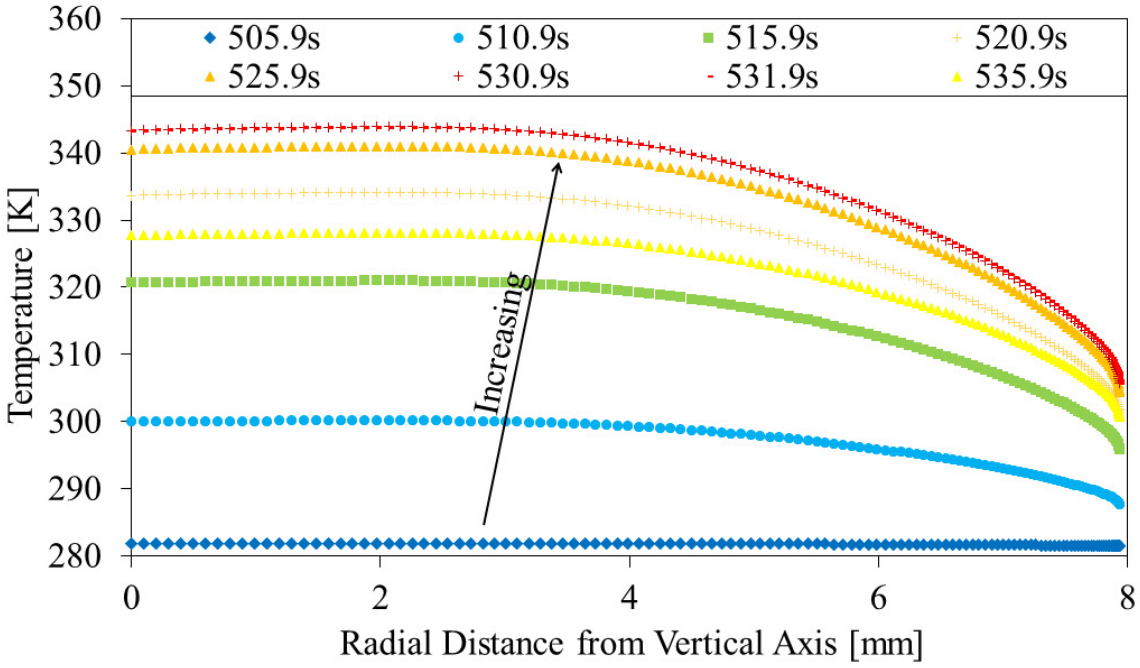

Figure 26. Temperature distribution along cooled surface for the first cycle of the Gen 2 sample holder nominal case

4.2 Gen 1 Sample Holder Parametric Study

The numerical model of the Gen 1 sample holder was also used to determine the limiting parameters during HHF testing for the sample holder in order to establish operational safety limits during high heat flux (HHF) testing. This initial analysis considered only two limiting parameters: the maximum temperatures in the sample holder as a function of a range of incident heat flux (IHF) values, and the IHF values where critical

heat flux (CHF) occurs at the stagnation point. The thermal performance of the sample holder is then evaluated over a range of parameters within these operational safety limits.

4.2.1 Incident Heat Flux Limit as Defined by Melting Temperature of Cu and Mo Materials

These analyses only considered the same 15 s interval that was considered in the nominal case. The simulations were used to determine the minimum value of IHF when any part of the copper (Cu) and molybdenum (Mo) portions of the Gen 1 sample holder reached their respective melting points for coolant mass flow rates $\dot{m}$ = 32 g/s, 50 g/s, and 100 g/s. An initial parametric study that considered various system pressure values of 80 psi, 140 psi, and 200 psi indicated that the system pressure had little, if any, effect on the maximum temperatures of the Mo and Cu parts of the sample holder. All the results reported here were therefore obtained at a system pressure of 80 psi. The results shown in Figure 27 suggest that the temperatures in the Cu part reach the melting point of Cu well before those in the Mo part reach the melting point of Mo for all three $\dot{m}$. Moreover, variations in $\dot{m}$ have little effect on the value of the IHF required for the Cu part to reach its melting point. Therefore, the parameter limiting the allowable IHF for the Gen 1 sample holder is the melting point of Cu, which occurs at an IHF of approximately 6 MW/m^2. As depicted in Figure 27, increasing $\dot{m}$ from 32 g/s to 100 g/s, only increases the maximum allowable IHF by 0.5 MW/m^2 for the Gen 1 sample holder. In contrast, the melting temperature of Molybdenum is reached at an IHF of approximately 8.7 MW/m^2, and variations in $\dot{m}$ again have little effect on the maximum allowable IHF.

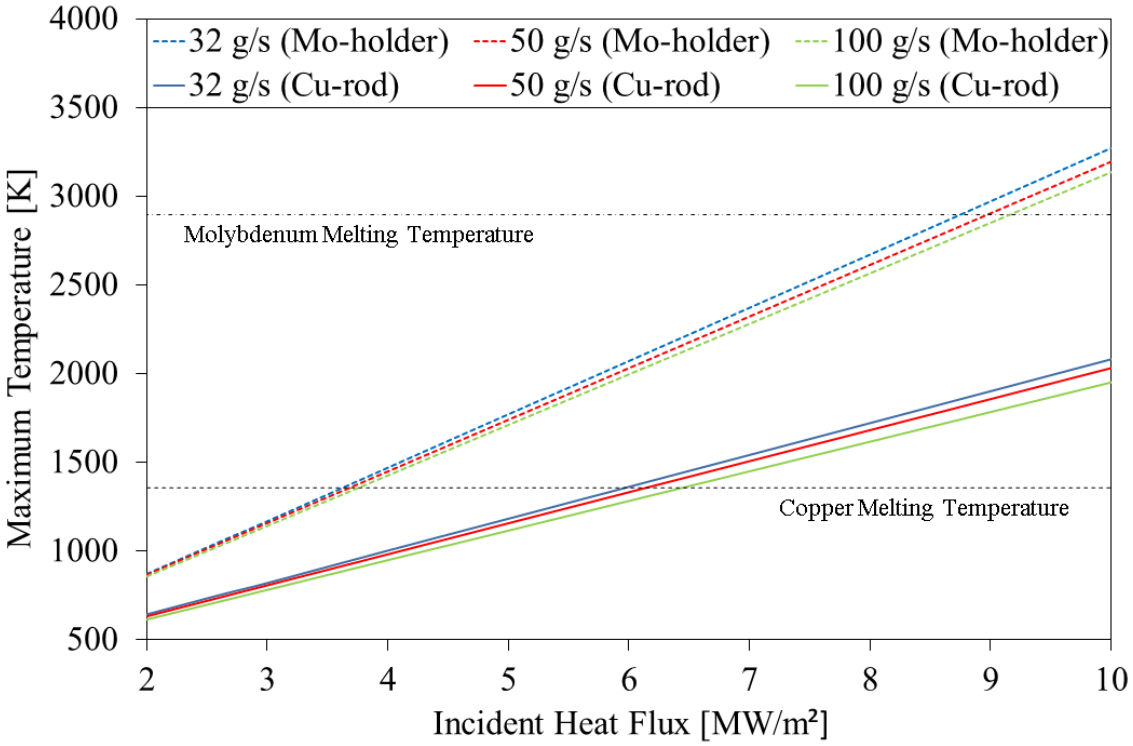

Figure 27. Effect of the incident heat flux on the maximum temperature of the Mo-holder and Cu-rod for the Gen 1 sample holder

4.2.2 Incident Heat Flux Limit as Defined by the Critical Heat Flux

Critical heat flux (CHF) is a major issue in two-phase evaporative cooling because the temperature of the wall in contact with the coolant increases rapidly under CHF conditions, causing a significant decrease in the HTC along the cooled surface. This decrease in HTC could, for example, lead to melting of the Cu part of the sample holder at lower IHF values than those shown in the previous section.

Unfortunately, there is no general valid method for predicting when CHF will occur. None of the standard CHF correlations are applicable to the complex geometry of these sample holders. Nevertheless, a conservative estimate for the CHF can be obtained using the correlation (Eq. 2) proposed by Škéma and Šlančiauskas [25], for a submerged circular jet of highly sub-cooled water with dimensions similar to those of the sample

holders. Table 7 compares the dimensions of the Gen 1 sample holder with the range of applicability of the Škéma and Šlančiauskas (ŠŠ) correlation.

Table 7. Range of applicability for Škéma and Šlančiauskas correlation in comparison to the Gen 1 sample holder parameters

Parameter	Range of applicability of ŠŠ correlation	Gen 1 Sample Holder
Nozzle Diameter '*d*' [mm]	$3 \leq d \leq 18$	6.4
Heater Diameter '*D*' [mm]	$9 \leq D \leq 20$	12
Ratio of Diameters '*D/d*'	$0.5 \leq D/d \leq 6.67$	2.34
Nozzle-to-Surface Spacing '*h/d*'	$2 \leq h/d \leq 4$	0.744
Jet Velocity 'V_j' [m/s]	$1 \leq V_j \leq 35$	1.01
Degree of Subcooling 'ΔT_{sub}' [°C]	$85 \leq \Delta T_{sub} \leq 151$	148

As can be deduced from Table 7, the ŠŠ correlation should, with one exception, apply to the Gen 1 sample holder. This exception, specifically the nozzle-to–surface spacing (separation distance) *h*/*d*, and other differences between the Gen 1 sample holder and the experimental data used to develop the ŠŠ correlation are discussed next.

As previously discussed in the literature review, Katto and Kunihiro [17] studied the effects of the separation distance on the CHF for submerged, circular jets of water, and concluded that the CHF increases with decreasing separation distance. Similarly, Aihara et al. [22] studied the effects of separation distance in a concave geometry, similar to that of the sample holder, and observed a significant increase in CHF with decreasing separation distance. Therefore, using the Škéma and Šlančiauskas correlation will yield a conservative estimate of the CHF for the Gen 1 sample holder, which has a *h*/*d* less than the minimum value for this correlation.

The experiments of Škéma and Šlančiauskas considered only a jet of sub-cooled water impinging on a flat target, *vs.* the concave target for the Gen 1 sample holder. Aihara et al. [22] compared the effect of heater geometry, specifically flat heater (with and without the needle) and a hemispherical, concave heater on the CHF. They reported that the critical heat flux for the hemispherical surface was approximately 70 % to 90 % greater than the value obtained for the flat surface with and without the needle, respectively. This suggests that the prediction for flat surfaces is more conservative than that for hemispherical surfaces. In addition, Škéma and Šlančiauskas considered a water jet flowing downwards, while the jet flows upwards in the sample holder. As discussed in the literature review, gravitational effects on jets should be negligible when the ratio between the nozzle height and nozzle diameter $z/d < 5$ [6]. Gravitational effects should therefore be negligible. Finally, Škéma and Šlančiauskas developed their correlation for steady-heating, and the sample holder is of course subject to transient heating. In order to establish a reasonable comparison when using the ŠŠ correlation, steady-state simulations were conducted for all the cases studied here, and a curve-fit to the results from these steady-state simulations were used to develop a correlation for the heat flux incident on the sample holder and the local heat flux (LHF) at the stagnation point. Data corresponding to all nine cases were considered ($\dot{m}$ = 32 g/s, 50 g/s, and 100 g/s and system pressures P = 80 psi, 140 psi, and 200 psi) and plotted in Figure 28..

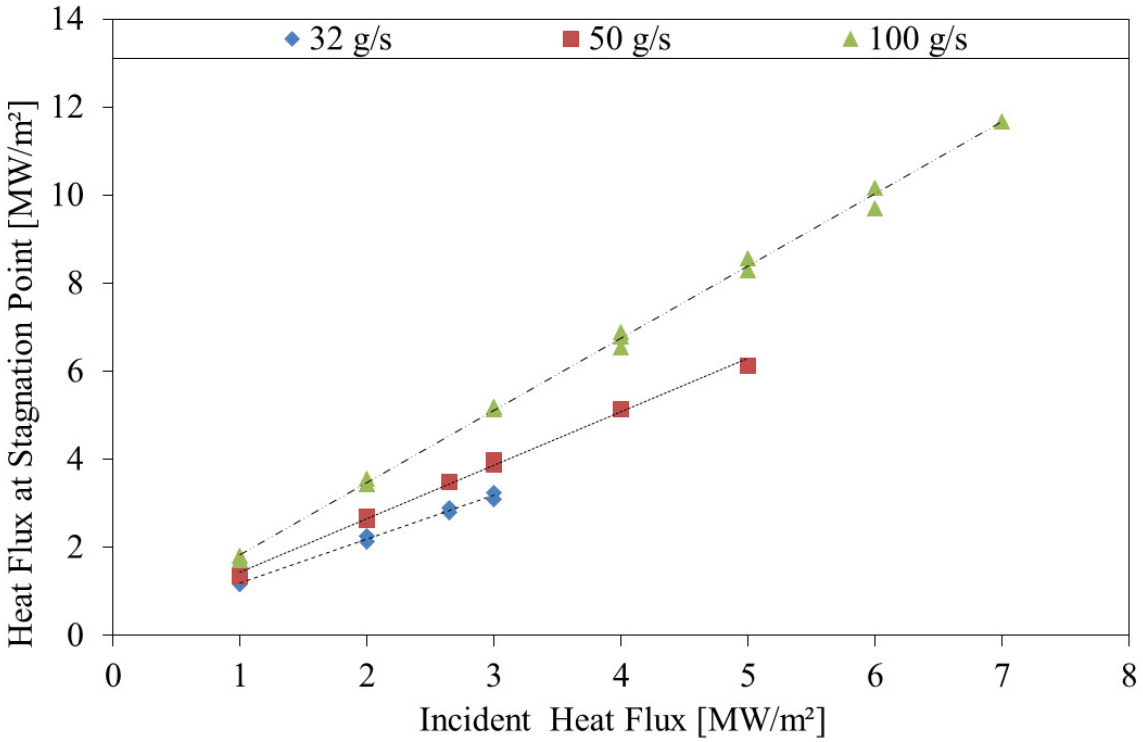

Figure 28. Data fitting for all cases considered in the steady-state parametric analysis defining the ratio between the IHF on the sample holder and the LHF at the stagnation point for Gen 1 sample holder

As depicted in Figure 28, the ratio between the incident heat flux and the local heat flux at the stagnation point appears unaffected by the pressure variation. Using the linear curve-fitting tool available in Microsoft® Excel 2010, fitted-correlations and their respective R^2 values describing the heat flux ratio are obtained for each of the mass flow rates evaluated. The resulting linearly fitted-correlations used to define the IHF, q''_{IHF}, at which the LHF value, q''_{LHF}, is equal to the CHF for 32 g/s, 50 g/s, and 100 g/s are given by Equations 31, 32, and 33, respectively.

$$q''_{IHF_{32\,g/s}} = \frac{1}{1.0024}\left[q''_{LHF_{32\,g/s}} - 0.1865\right] \qquad R^2 = 0.994 \tag{31}$$

$$q''_{IHF_{50\,g/s}} = \frac{1}{1.2177}\left[q''_{LHF_{50\,g/s}} - 0.2065\right] \qquad R^2 = 0.997 \tag{32}$$

$$q''_{IHF_{100\,g/s}} = \frac{1}{1.6403}\left[q''_{LHF_{100\,g/s}} - 0.1807\right] \qquad R^2 = 0.998 \tag{33}$$

Despite their limitations, using these correlations to find the respective IHF for a given CHF value should provide a conservative estimate for the conditions under which CHF will occur at the stagnation point. Table 8 presents the CHF value q''_{LHF} nd its corresponding IHF value, $q''_{IHF}$for each of the nine parametric cases. The degree of sub-cooling is also considered and results for the sub-cooled water jet (ΔT_{sub} = 148 °C) and boiling water jet (ΔT_{sub} = 0 °C) cases are provided. As discussed in the literature review, the CHF value (Eq. 2) is directly affected by the sub-cooling correction factor (Eq.4) which is reflected in the results presented. For each mass flow rate evaluated, three pressure values are considered (80 psi, 140 psi, and 200 psi). The effects of pressure variation are discussed in the next section.

Table 8. Predictions for the CHF as given by the Škéma and Šlančiauskas correlation for sub-cooled and boiling water jets in the Gen 1 sample holder

Parametric Case		Critical Heat Flux (ΔT_{sub} = 0 °C)		Critical Heat Flux (ΔT_{sub} = 148 °C)	
Pressure [psi]	Mass Flow Rate [g/s]	q''_{LHF} [MW/m^2]	q''_{IHF} [MW/m^2]	q''_{LHF} [MW/m^2]	q''_{IHF} [MW/m^2]
80	32	5.31	5.11	18.4	18.2
	50	5.86	4.64	20.3	16.5
	100	6.98	4.14	24.1	14.6
140	32	6.27	6.07	18.9	18.6
	50	6.92	5.51	20.8	16.9
	100	8.23	4.91	24.7	14.9
200	32	6.94	6.74	19.1	18.9
	50	7.66	6.12	21.1	17.1
	100	9.11	5.44	25.0	15.1

As can be deduced from Table 8, the CHF is not the primary limiting factor for any of the sub-cooled cases considered regardless of mass flow rate or pressure value. As shown in Figure 26, the melting temperature of Copper is achieved within the Cu-rod at an IHF lower than that needed to reach CHF for any of the sub-cooled cases. Another trend worth noting is exhibited by the value of the IHF. For a specific pressure case, as the mass flow rate increases, the corresponding IHF value at which the CHF value is reached at the local stagnation point decreases. This result is counter-intuitive as it would be expected to see an increase in the allowable IHF with increasing $\dot{m}$, however, the behavior is reversed. In other words, the allowable IHF for 32 g/s is higher than that for 100 g/s even though the CHF value is higher for the $\dot{m}$ = 100 g/s. This behavior can be explained by examining the effects of $\dot{m}$ in the entire sample holder system. As $\dot{m}$ increases, the local HTC increases, so more heat is removed at the stagnation point, resulting in lower local wall temperature values. This increase in the temperature gradient means that more heat can be removed at a given IHF as $\dot{m}$ increases. Therefore, the system should reach CHF at the stagnation point more rapidly at lower IHF values when the mass flow rate is increased. The next section investigates the effect of system pressure for the range of relevant IHFs for the Gen 2 sample holder.

4.2.3 Effects of Pressure in the Applicable Range of Study

We next examine how system pressure P affects the thermal performance of the system. Simulations were performed at P = 80 psi, 140 psi, and 200 psi. For each pressure scenario, three mass flow rate values were considered (32 g/s, 50 g/s, and 100 g/s). The motivation for investigating the effects of pressure on the sample holder is related to the inherent increase in the fluid's saturation temperature. Moreover, defining the benefits and

the drawbacks associated with an increase in the pressure of the system are fundamental design conclusions that could be used as baseline for future sample holder designs. In this study, the effects of pressure are first considered individually for each case and then compared to one another. In addition to considering the effects of pressure with increasing mass flow rate and increasing IHF, the volume fraction (VF) of vapor formed at the stagnation point, as predicted by RPI model within ANSYS™ FLUENT®, is plotted in the figure below. For the 80 psi pressure case, Figure 29 presents the effect of the IHF for the 3 mass flow rate cases considered.

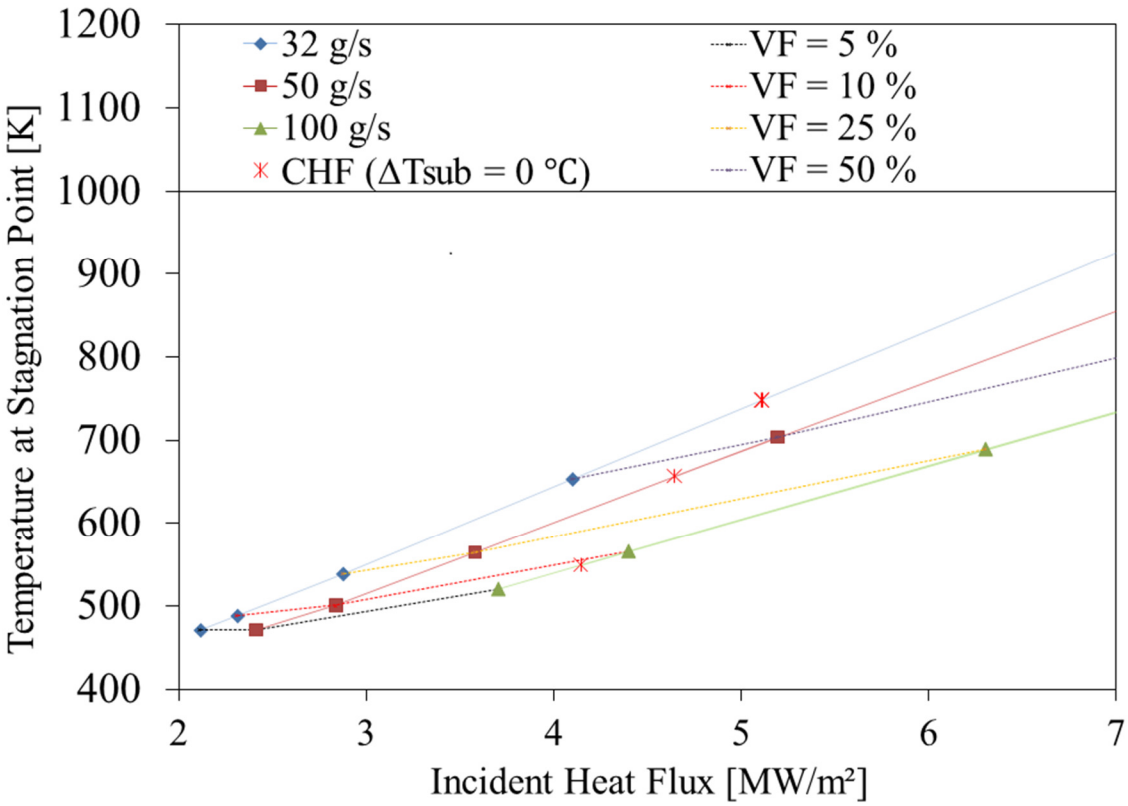

Figure 29. Comparative analysis of the effects of increasing incident heat flux at various mass flow rate values considering the estimate of vapor fraction formation for the Gen 1 sample holder at 80 psi system pressure

The effect of the mass flow rate variation and any resulting VFs are plotted simultaneously in Figure 29. For instance, when increasing the mass flow rate from 32 g/s

to 100 g/s and considering a VF of 5 %, the IHF needed to achieve such vapor formation increases from 2.11 MW/m^2 to 3.71 MW/m^2.One instance where predicting the vapor formation associated with a specific incident heat flux may be important is when bubble blanketing in a narrow channel is undesirable. The occlusion of the narrow channel by adherent bubbles is directly analogous to nucleate/film boiling where there is a maximum heat flux which depends on the insulating effect of the gas film or bubble layer on the heat transfer surface. Any attempt to increase the heat flux simply increases the blanketing effect of the bubble layer up to the point where burn-out of the heating surface occurs. In other words, bubble blanketing could cause flow obstruction and a significant decrease in the heat transfer coefficient which in turn causes a sudden increase in the wall temperature that may ultimately result in total system failure as the melting temperature could be rapidly reached at a lower IHF than predicted by previous analysis. It is important to conduct experiments to determine the target VF and its related operating parameters. Experimental data resulting from such experiment can be used to further validate the numerical model. Thus, a diagram such as the one presented in Figure 29 could be used as a tool for defining the IHF for a given $\dot{m}$ and target VF.

The results for the 140 psi pressure case are presented in Figure 30. The main difference associated with the increase in pressure is the reduction on the vapor formation for a given IHF, that is, when comparing against the results presented in Figure 29 for the 80 psi pressure case. This behavior is a result of the inherent increase in the saturation temperature, from 435.3 K (80 psi) to 450.1 K (140 psi), which in turn causes the wall superheat, $\Delta T_{superheat} = T_{wall} - T_{sat}$, to be larger in order to achieve the same vapor formation.

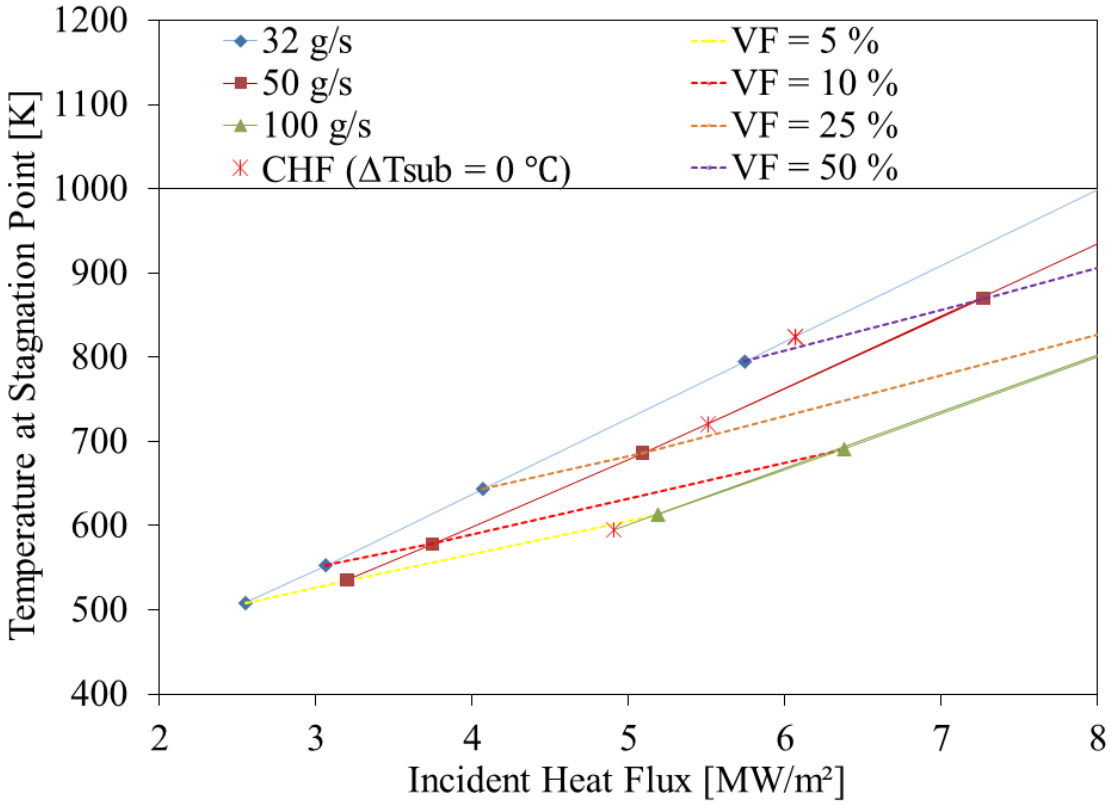

Figure 30. Comparative analysis of the effects of increasing incident heat flux at various mass flow rate values considering the estimate of vapor fraction formation for the Gen 1 sample holder at 140 psi system pressure

When considering the $\dot{m}$ effects in the overall performance, the same pattern was evident for the 140 psi pressure case. Specifically, the IHF needed to achieve a target VF increases with increasing $\dot{m}$. Another trend observed in the comparison of these two pressure cases was related to the CHF behavior. The increase in pressure, from 80 psi to 140 psi, caused a subsequent increase in the CHF and its respective IHF for a fixed $\dot{m}$. Data reported in Table 8 suggest an average increase of 2.44 % in the IHF for a set $\dot{m}$ and increasing *P*. On the other hand, an average decrease of 19.7 % in the IHF was reported for an increase in the mass flow rate from 32 g/s to 100 g/s at a fixed pressure. Essentially, when considering only the CHF as a limiting parameter, an overall decrease in the

allowable IHF for a given P with increasing $\dot{m}$ was observed, in contrast, an apparent increase in the allowable IHF for a fixed $\dot{m}$ with increasing pressure was reported.

In the 200 psi pressure case, depicted in Figure 31, the trends identified are similar to those previously discussed for the 80 psi and 140 psi pressure cases. However, the effect of $\dot{m}$ in the vapor formation is more pronounced than in the previous cases. This behavior is due to its saturation value temperature, $T_{sat,200psi}$ = 470.9 K.

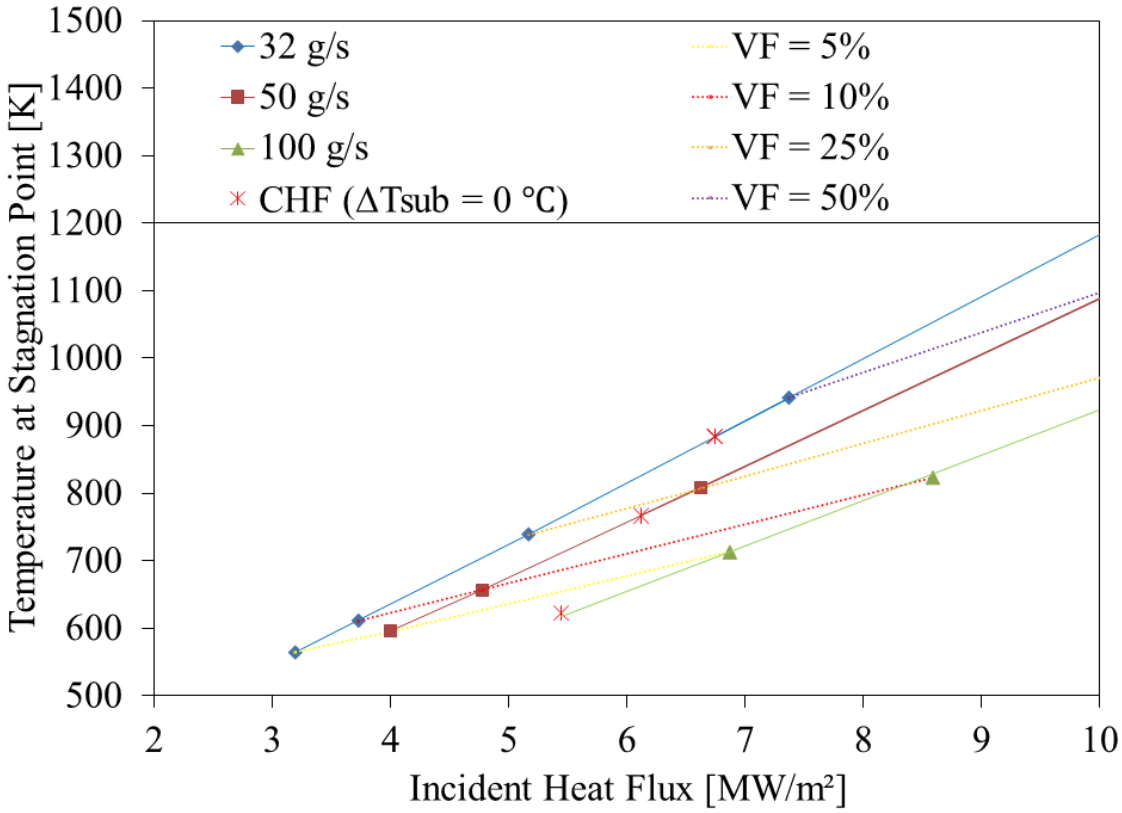

Figure 31. Comparative analysis of the effects of increasing incident heat flux at various mass flow rate values considering the estimate of vapor fraction formation for the Gen 1 sample holder at 200 psi system pressure

Throughout this section the effects of various parameters have been comprehensively evaluated (e.g., pressure, mass flow rate, and incident heat flux) in order to establish safe limits of operation during HHF testing. It was concluded that the melting temperature of Copper is the limiting parameter for the Gen 1 sample holder design (~ 6

MW/m^2). In addition, it was demonstrated that the CHF is not reached at the stagnation point under the current configuration. It was also determined that increasing the mass flow rate caused the allowable IHF value to decrease even though the CHF was increased with this parametric change. On the other hand, it was shown that the allowable IHF increases by 2.44 % with a net increase of 60 psi in pressure for the sub-cooled cases. Nevertheless, there are certain design considerations such as active coolant type and artifact materials, beyond the scope of this thesis, which should be considered in future sample holder designs.

The parametric study conducted on the Gen 2 sample holder is presented in the next section. Further discussion and closure on the parametric study presented for both models is given in the section 4.3.

4.3 Gen 2 Sample Holder Parametric Study

A parametric study was conducted using the numerical model developed for the Gen 2 sample holder. The first part of the analysis is focused on defining the limiting factor for HHF testing considering the materials used in the Gen 2 sample holder fabrication. In the second part of this section, the main goal is to study the effects of various parameters (e.g. mass flow rate, pressure, and incident heat flux) in order to draw conclusions that could serve as guidelines in the design of future sample holders. Also, safe limits for HHF testing under different parametric conditions are provided.

4.3.1 Incident Heat Flux Limit as Defined by Melting Temperature of Cu and Mo Materials

It is imperative to define the limiting factor during HHF testing as it facilitates the establishment of a range of study relevant to the Gen 2 sample holder. For the current model, two parameters are considered and compared; the melting temperatures of the sample holder materials and the CHF. The independent parameter used is the IHF which is increased from one testing interval to the next. The transient testing interval considered for this study consist of an irradiation period (15 seconds) and a dwell period (120 seconds) with a total duration of 135 seconds. The first limiting parameter considered is the melting temperatures of Molybdenum and Copper. Specifically, the IHF threshold at which the melting point of either material would be reached in either the Mo-clamp or the Cu-rod, respectively, is defined.

As considered in the examination of the Gen 1 sample holder, the effects of mass flow rate variation with respect to the melting point are also analyzed for the Gen 2 sample holder. Specifically, three mass flow rate values are considered: 32 g/s, 50 g/s, and 100 g/s. Although a parametric study was conducted considering various system pressure values (80 psi, 140 psi, and 200 psi), no significant difference was observed in the prediction for maximum temperatures in the Mo-holder and Cu-rod. Therefore, a pressure value of 80 psi was considered in the results reported in Figure 32. The resultant behavior of the maximum temperatures of Molybdenum (Mo-clamp) and Copper (Cu-rod), for these three mass flow rate cases, was plotted simultaneously as shown in Figure 32.

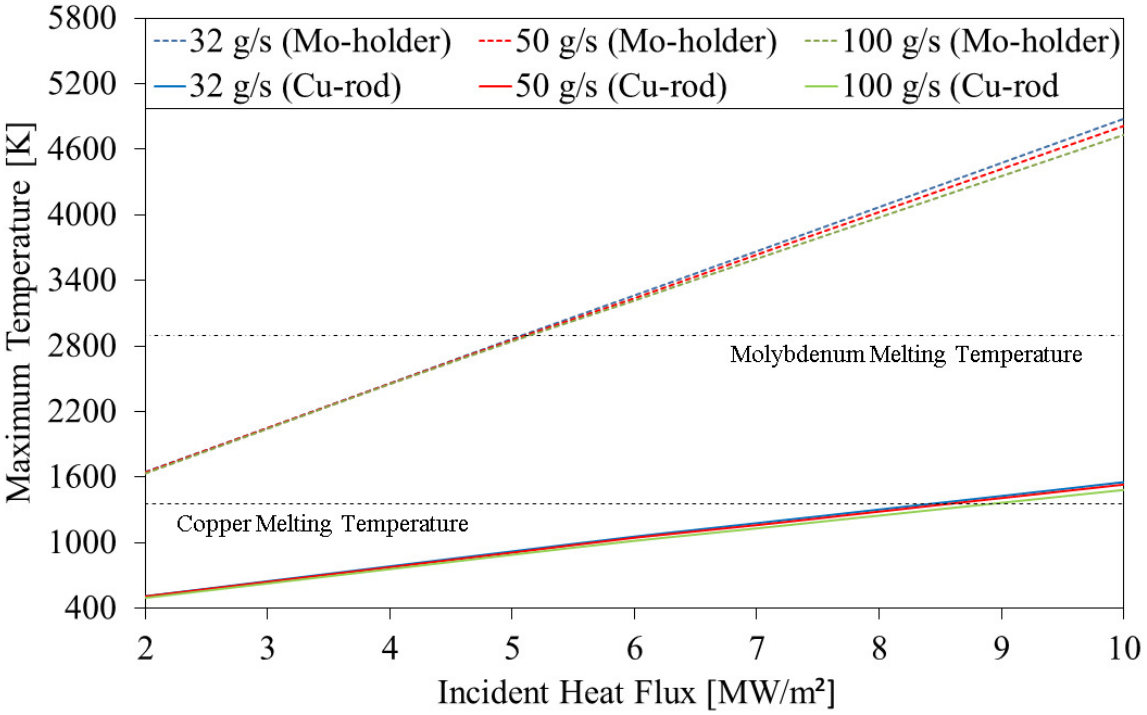

Figure 32. Effects of the incident heat flux on the maximum temperature of the Mo-holder and Cu-rod for Gen 2 sample holder

The results suggest that the melting temperature of Molybdenum is reached within the Mo-clamp piece at an IHF of about 5 MW/m^2 whereas the melting temperature of Copper is reached within the Cu-rod piece at an IHF of about 8.2 MW/m^2 (disregarding Mo-clamp melting effects). In addition, the results indicate a negligible effect of the mass flow rate on the maximum heat flux limit. In other words, the melting temperature of Molybdenum is reached at approximately the same IHF regardless of the coolant mass flow rate value (from 32 g/s to 100 g/s).

A plausible explanation of the behavior observed for the melting temperature of Molybdenum is obtained by closely examining the sample holder head design. In this model, the sample holder head is composed of three pieces; a W-F82H-sample, a Mo-clamp, and a Mo-holder. As observed in Figure 14, the Mo-clamp is clamped to the Mo-holder using three Molybdenum bolts (not considered in the 2D model). Between these two

pieces, the W-F82H-sample is held tightly in place. The reported measurement of the gap between the Mo-clamp and the Mo-holder was 44 μm [47]. Even though the gap is seemingly small, it is sufficient to affect the way heat is conducted along the sample holder head. The separation gap between the two Molybdenum pieces causes the heat to naturally look for alternative pathways to diffuse more easily; hence, a shift in the temperature and heat flux profiles is evident as higher temperature are observed in the middle of the sample holder head. Another consequence of the separation gap is the rapid rise in temperature within the Mo-clamp, which limits HHF testing capabilities, as the melting temperature of Molybdenum is achieved at a lower IHF. A feasible solution may be to decrease the separation gap distance between the two Molybdenum pieces. Figure 33 depicts the effects of separation gap distance on the maximum temperatures within the Mo-clamp and Cu-rod for increasing IHF. This analysis was performed considering only the nominal transient case; a mass flow rate of 32 g/s and a system pressure of 80 psi.

As can be deduced from Figure 33, the decrease in the separation gap distance has a significant impact in extending the IHF range before the melting temperature of molybdenum is reached. When considering a separation gap of 30 μm the Molybdenum melting temperature is still the limiting factor as it is reached at an IHF of about 6.1 MW/m^2. A further decrease from 44 to 15 μm causes the allowable IHF to increase from about 5 MW/m^2 to about 8 MW/m^2. Consequently, the reduction in separation gap distance also affects the allowable IHF for the Cu-rod. The results suggest that for a gap of 15 μm the allowable IHF for the Cu-rod is approximately 7.75 MW/m^2. Thus, for a gap of 15 μm, the limiting factor is the Cooper melting temperature and the maximum allowable IHF is about 7.75 MW/m^2.

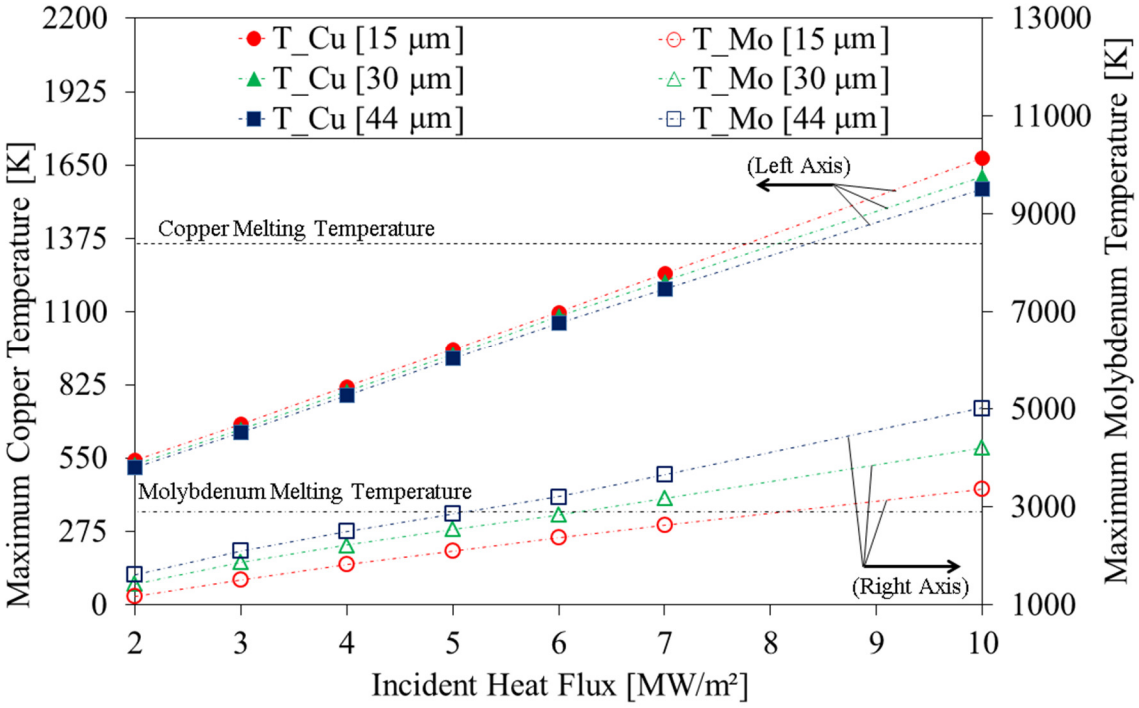

Figure 33. Effects of the incident heat flux in the maximum temperature of the Mo-holder and Cu-rod for varying separation gap distance of the Gen 2 sample holder

The results presented in the separation gap analysis assume uniformity in the gap distance across the Mo-clamp and Mo-holder interphase. However, due to the clamping method and the thermal expansion associated with the heating period, there is a probability that the two Molybdenum pieces are in contact with each other at various locations which may alter significantly the temperature and heat distribution along the sample holder.

Overall, it was concluded that, with the current gap of 44 µm, the limiting factor is the melting temperature of Molybdenum which is reached at an IHF of about 5 MW/m^2 for the nominal transient case. In addition, it was determined that a reduction in the separation gap increases significantly the allowable IHF for the Gen 2 sample holder. An optimal value for the separation gap in this model was estimated to be about 15 µm. In the next section, the attention is shifted towards the evaluation of the CHF for all the parametric cases considered in order to determine whether or not the CHF is the limiting factor.

4.3.2 Incident Heat Flux Limit as Defined by the Critical Heat Flux

The CHF is now considered as the second limiting parameters in the definition of the allowable IHF. In the case of active liquid cooling, it is fundamental to determine the conditions under which the CHF is reached. The CHF is characterized by a rapid increase in wall temperature accompanied by a significant decrease in the heat transfer coefficient along the cooled surface. The common approach for CHF definition is based on experimental work coupled with numerical analysis of the results. The data is fitted to an empirical correlation describing the trend observed experimentally. Predicting the CHF is not an easy task as its definition is influenced by multiple parameters such as geometry, flow regime, pressure, etc. Due to the complex geometry presented by the sample holders, there is no correlation that can accurately predict the CHF for this particular design. Nonetheless, a conservative estimate for the CHF can be obtained by considering the correlation (Eq. 2) proposed by Škéma and Šlančiauskas [25], for a submerged, circular jet of highly sub-cooled water with comparable geometric parameters to those presented by the Gen 2 sample holder. Table 9 lists the ranges of applicability of the correlation for several relevant geometric parameters in the Gen 2 sample holder. For each mass flow rate evaluated, three pressure values are considered (80 psi, 140 psi, and 200 psi).

Table 9. Range of applicability for Škéma and Šlančiauskas correlation in comparison to Gen 2 sample holder parameters

Parameter	Range of applicability of ŠŠ correlation	Gen 2 Sample Holder
Nozzle Diameter '*d*' [mm]	$3 \leq d \leq 18$	9.1
Heater Diameter '*D*' [mm]	$9 \leq D \leq 20$	20
Ratio of Diameters '*D/d*'	$0.5 \leq D/d \leq 6.67$	2.74
Nozzle-to-Surface Spacing '*h/d*'	$2 \leq h/d \leq 4$	0.874
Jet Velocity 'V_j' [m/s]	$1 \leq V_j \leq 35$	5.367
Degree of Subcooling 'ΔT_{sub}' [°C]	$85 \leq \Delta T_{sub} \leq 151$	153

As depicted in Table 9, the experimental setup for which the correlation was developed and that of the sample holder are geometrically similar. As observed in the Gen 1 sample holder, in the Gen 2 sample holder, parametric differences were observed for the nozzle-to–surface spacing (separation distance), the heater geometry, the flow direction, and the heat source mode. A detailed discussion considering the effects of each of these four parameters was provided in section 4.2.2. Overall, it was concluded that considering the effects of separation distance and target geometry would increase the value estimated for the CHF. Therefore, the value predicted by the Škéma and Šlančiauskas correlation is a conservative estimate of the CHF for the Gen 2 sample holder. It was also determined that the flow direction appears to be negligible as the ratio between the nozzle height and nozzle diameter does not exceed five ($z/d < 5$) [6].

In addition, the heat mode under which the Škéma and Šlančiauskas experiments were conducted should also be considered. This correlation was developed for steady-state heating which differs from the transient heating mode used during the HHF testing on the

sample holders. Therefore, steady-state simulations using the Gen 2 sample holder numerical were conducted in order to establish a reasonable comparison when using the Škéma and Šlančiauskas correlation. Nine parametric cases were considered where the mass flow rate and the system pressure were varied (32 g/s, 50 g/s, and 100 g/s at 80 psi, 140 psi, and 200 psi). Figure 34 presents the results from these steady-state simulations. Using the data-fitting tool available in Microsoft® Excel 2010, fitted correlations were obtained that describe the ratio between the heat flux incident on the sample holder and the local heat flux (LHF) at the stagnation point.

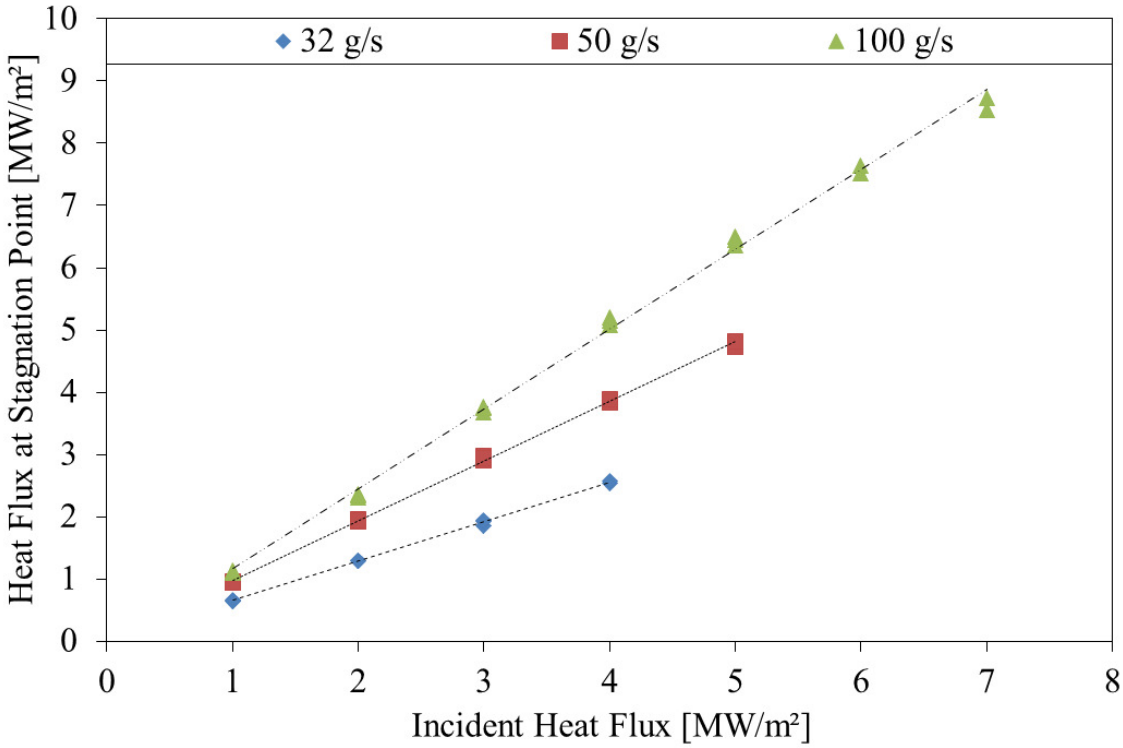

Figure 34. Data fitting for all cases considered in the steady state parametric analysis defining the ratio between the incident heat flux and the local heat flux at the stagnation point for Gen 2 sample holder

As depicted in Figure 34, the data points for the three pressure cases considered at each mass flow rate fall on the top of each other. Hence, the ratio between the IHF and the LHF at the stagnation point appears unaffected by the pressure variation. Trend lines and

fitted-correlations to describe the heat flux ratio are obtained for each of the mass flow rates evaluated. The resulting linearly fitted-correlations and their respective R^2 values used to define the IHF, q''_{IHF}, at which the LHF value, q''_{LHF}, is equal to the CHF for 32 g/s, 50 g/s, and 100 g/s are given by Equations 34, 35, and 36, respectively.

$$q''_{IHF_{32\ g/s}} = \frac{1}{0.6315}\left[q''_{LHF_{32\ g/s}} - 0.0239\right] \qquad R^2 = 0.999 \tag{34}$$

$$q''_{IHF_{50\ g/s}} = \frac{1}{0.9610}\left[q''_{LHF_{50\ g/s}} - 0.0178\right] \qquad R^2 = 0.999 \tag{35}$$

$$q''_{IHF_{100\ g/s}} = \frac{1}{1.2832}\left[q''_{LHF_{100\ g/s}} - 0.1198\right] \qquad R^2 = 0.997 \tag{36}$$

Although utilizing these correlations to find the respective IHF for a critical heat flux value is not a perfect comparison because of the heating mode considered in the experiments, it is still valid as it provides a conservative estimate for the CHF at stagnation. In Table 10, the results for the CHF value, also referred to as LHF,q''_{LHF}, and its corresponding IHF value, q''_{IHF}, are presented for the nine parametric cases. As discussed in the literature review, the CHF value (Eq. 2) is directly affected by the sub-cooling correction factor (Eq.4). Thus, the effects of sub-cooling are also considered and results for the sub-cooled water jet (ΔT_{sub} = 148 °C) and boiling water jet (ΔT_{sub} = 0 °C) cases are provided below.

Table 10. Predictions for the CHF as given by the Škéma and Šlančiauskas correlation for sub-cooled and boiling water jets in the Gen 2 sample holder

Pressure [psi]	Mass Flow Rate [g/s]	Critical Heat Flux (ΔT_{sub} = 0 °C) [MW/m^2]		Critical Heat Flux (ΔT_{sub} = 153 °C) [MW/m^2]	
		q''_{LHF}	q''_{IHF}	q''_{LHF}	q''_{IHF}
80	32	4.63	7.29	16.6	26.2
	50	5.04	5.22	18.1	18.8
	100	5.84	4.65	20.9	16.4
140	32	5.46	8.61	16.9	26.7
	50	5.95	6.17	18.4	19.1
	100	6.89	5.47	21.3	16.7
200	32	6.05	9.55	17.0	26.9
	50	6.59	6.84	18.5	19.3
	100	7.64	6.05	21.5	16.8

As reflected in Table 10 and with the exception of the case with no sub-cooling at 100 g/s and 80 psi, the CHF is not the primary limiting factor for any of the other 8 cases where no sub-cooling considered, nor the 9 cases where sub-cooling is considered. As depicted in Figure 32, the melting temperature of Molybdenum is achieved within the Mo-clamp at an IHF lower than that needed to reach CHF for any of the cases considered. Therefore, the primary limiting factor for the allowable IHF is the melting temperature of Molybdenum as shown in the previous section (~ 5 MW/m^2).

As previously noted for the Gen 1 sample holder, the IHF value displays a similar behavior for the Gen 2 sample holder. For a specific pressure case, as the mass flow rate increases, the corresponding IHF value at which the CHF value is reached at the local stagnation point decreases. In other words, the allowable IHF for 32 g/s is higher than that for 100 g/s even though the CHF value is higher for the 100 g/s mass flow rate case. By examining the effects of the mass flow rate in the entire sample holder system, the trend

observed can be explained. As the mass flow rate increases, there is an inherent increase in the temperature gradient across the solid as the local temperature value at the stagnation point decreases. The lower wall temperatures are characteristic of the improved ability for heat removal caused by the enhancement in the local heat transfer coefficient resultant from the increase in the mass flow rate. Therefore, it is expected for the system to reach CHF at stagnation point more rapidly for lower IHF values when the mass flow rate is increased.

Throughout this section the CHF effects on the Gen 2 sample holder were considered for various parametric condition. Using the Škéma and Šlančiauskas correlation and previous experimental work for jet impingement cooling, presented in the literature review, conservative estimates for the CHF were provided for each of the nine parametric cases considered. It was determined that the CHF is not the limiting parameter for the Gen 2 sample holder. Therefore, it was shown that the melting temperature of the Molybdenum, which is reached at about 5 MW/m^2, is the limiting factor for the allowable IHF to be used during HHF testing of the Gen 2 sample holder. By defining the limiting parameter, the range of applicability for the parametric study can be further evaluated. Hence, the results considering the effects of pressure for the range of relevant IHFs are presented and discussed in the next section.

4.3.3 Effects of Pressure in the Applicable Range of Study

Through the limiting factor analysis, the applicable range of study was determined [0 to 5 MW/m^2]. The parametric analysis is continued by examining the effects of pressure on the thermal performance of the system for this range. The numerical model developed for the Gen 2 sample holder is utilized to evaluate three pressure scenarios: 80 psi, 140 psi, and 200 psi. For each pressure scenario, three mass flow rate values are considered (32 g/s,

50 g/s, and 100 g/s). The inherent increase in the liquid's saturation temperature is the motivation for examining the effects of pressure on the sample holder. Moreover, determining the benefits and the disadvantages associated with an increase in the pressure of the system are fundamental design conclusions that could be used as guidelines for future sample holder. In this analysis, the effects of pressure are first considered individually for each case and then compared to one another. Another parameter considered is the volume fraction (VF) of vapor formed at the stagnation point, as predicted by RPI model within ANSYS™ FLUENT®, which is plotted simultaneously for the three mass flow rate cases. Figure 35 depicts the effect of the incident heat flux for the 3 mass flow rate cases considered at the 80 psi pressure case.

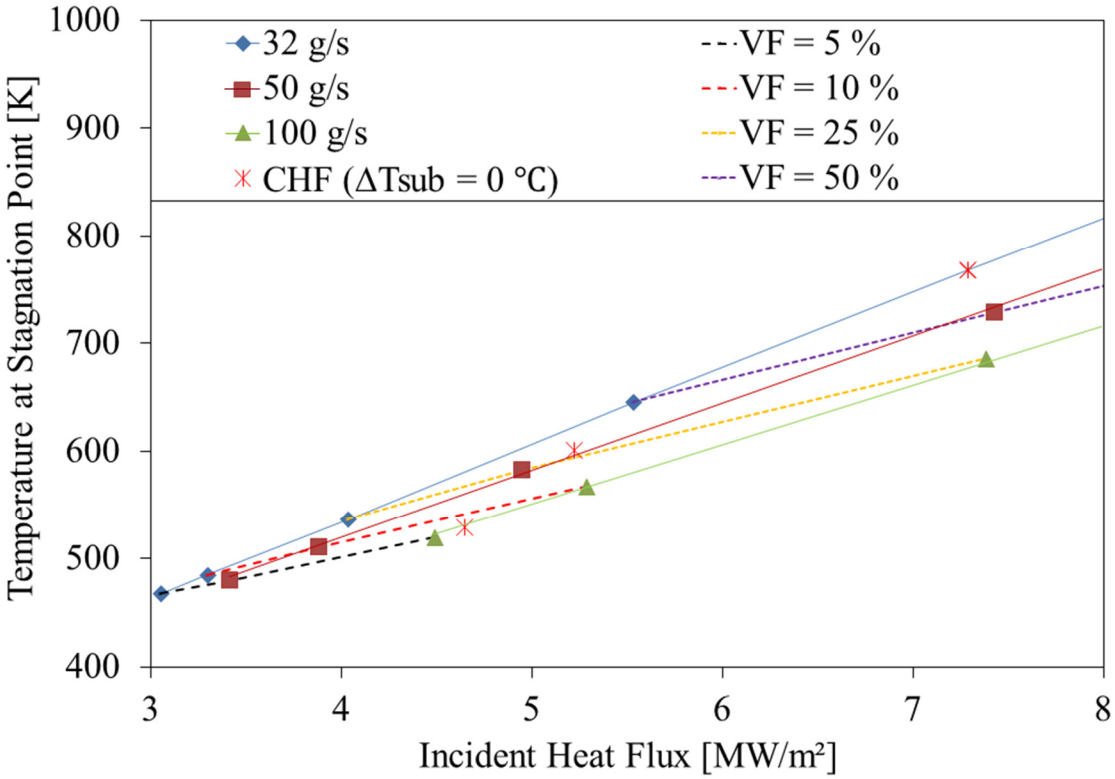

Figure 35. Comparative analysis of the effects of increasing incident heat flux at various mass flow rate values considering the estimate of vapor fraction formation for the Gen 2 sample holder at 80 psi system pressure

The major impact of increasing the mass flow rate is reflected in the formation of vapor in reference to the incident heat flux. For instance, when considering a VF of 5 % (going from 32 g/s to 100 g/s) , the incident heat flux needed to achieve such vapor formation increases from 3.05 MW/m^2 to 4.49 MW/m^2. As mentioned in the analysis performed for the Gen 1 sample holder, bubble blanketing causing blockage of flow is an issue that must be considered, especially, in narrow channel flow. Although the size of the annular channels of the sample holder design has been doubled in the Gen 2 sample holder (from 0.8 mm to 1.6 mm), blockage of the flow due to bubble blanketing should be avoided. Bubble blanketing diminishes the system's ability to remove heat via convective cooling causing a significant increase in temperature of the solid components which may result in total system failure. In order to determine safe limits of vapor formation for various parametric scenarios, experiments should be conducted to determine target VFs and their associated operating parameters. The data obtained from these experiments can be used to further validate the numerical model for the Gen 2 sample holder. Once validated, a diagram such as the one presented in Figure 35 could be used as tool for defining the IHF for a given mass flow rate and target VF.

The results for the 140 psi pressure case are presented in Figure 36. The main difference associated with the increase in pressure is the reduction on the vapor formation for a given incident heat flux, that is, when comparing against the results presented in Figure 35 for the 80 psi pressure case. This behavior is a result of the inherent increase in the saturation temperature, from 435.3 K (80 psi) to 450.1 K (140 psi), which in turn causes the wall superheat to be higher in order to achieve the same vapor formation.

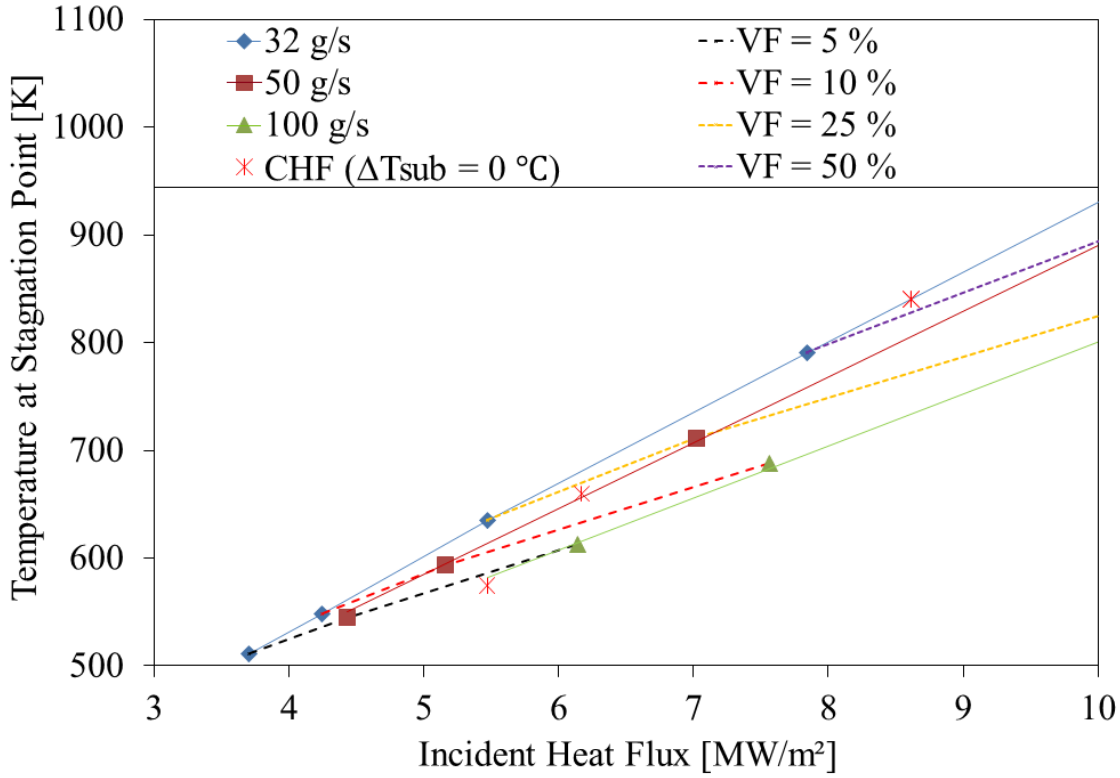

Figure 36. Comparative analysis of the effects of increasing incident heat flux at various mass flow rate values considering the estimate of vapor fraction formation for the Gen 2 sample holder at 140 psi system pressure

When considering the mass flow rate effects on the overall performance, the same pattern was evident for the 140 psi pressure case. Specifically, the incident heat flux needed to achieve a target VF increases with increasing mass flow rate. Another trend observed when comparing pressures cases is the increase in the CHF and its respective IHF for three mass flow rate cases. Data reported in Table 10 suggest an average increase of 1.85 % in the IHF for increasing pressure and a set mass flow rate. On the other hand, an average decrease in the IHF of about 37.4 % was reported for an increase in the mass flow rate (from 32 g/s to 100 g/s) at a fixed pressure. Basically, when considering only the CHF as a limiting parameter, an overall decrease in the allowable IHF for a given pressure with increasing mass flow rate was observed, in contrast, an apparent increase in the allowable IHF for a fixed mass flow rate with increasing pressure was reported.

The results found in the incident heat flux analysis of the 200 psi pressure case are presented in Figure 37.

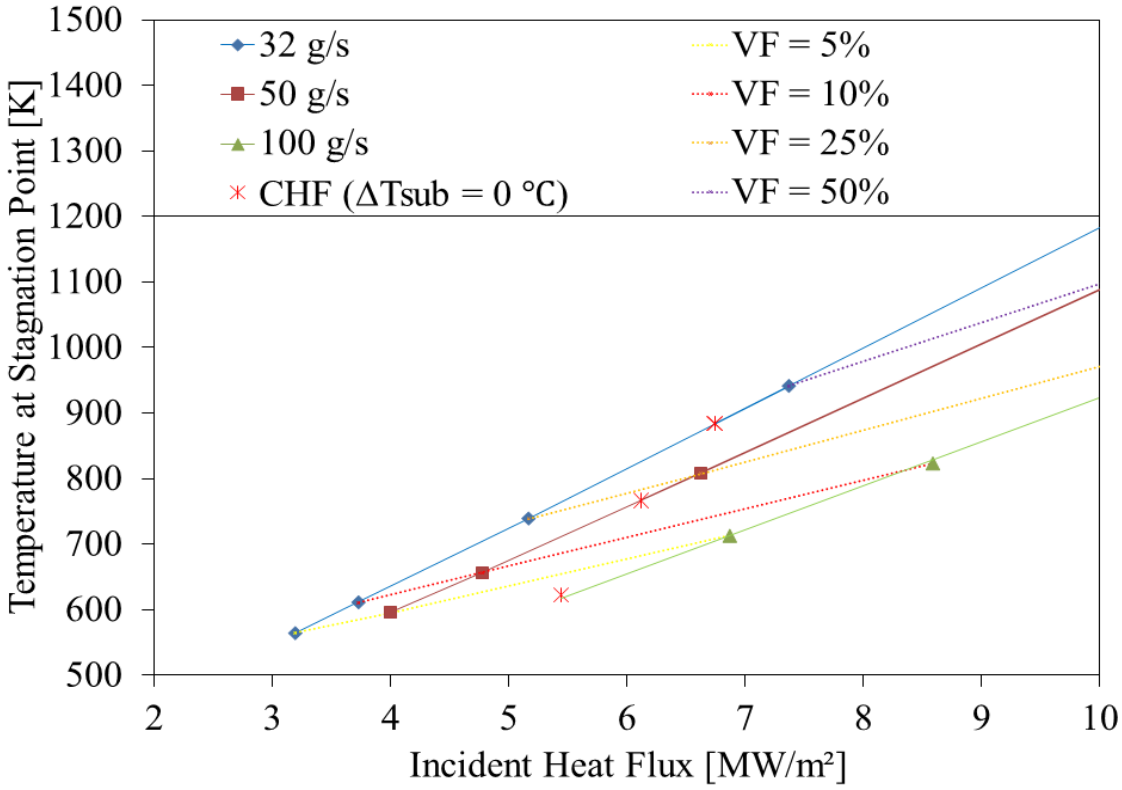

Figure 37. Comparative analysis of the effects of increasing incident heat flux at various mass flow rate values considering the estimate of vapor fraction formation for the Gen 2 sample holder at 200 psi system pressure

As depicted in Figure 37, the trends identified are similar to those previously discussed for the 80 psi and 140 psi pressure cases. However, the effect of mass flow rate on the vapor formation is more prominent than in the previous pressure cases. This behavior is associated to its saturation temperature value, $T_{sat,200psi}$ = 470.9 K.

Throughout this section the effects of various parameters (e.g., pressure, mass flow rate, and incident heat flux) have been evaluated with the purpose of establishing safe limits of operation during for HHF testing using the Gen 2 sample holder. It was concluded that the melting temperature of Molybdenum is the limiting factor for this holder design (~ 5

MW/m^2). In addition, it was demonstrated that the CHF is not reached at the stagnation point under the current configuration. It was also determined that increasing the mass flow rate caused the allowable IHF value to decrease even though the CHF was increased with this parametric change. On the other hand, it was shown a 1.85% increase in the maximum allowable IHF with a net increase of 60 psi in the pressure for the sub-cooled cases. Further discussion and closure on the parametric study presented for both models is given in the next section.

4.4 Gen 1 and Gen 2 Sample Holder Designs Comparison

In this section the impact of the geometric differences between the Gen 1 sample holder and the Gen 2 sample holder are examined in order to evaluate the advantages and disadvantages associated to each modification. Since both sample holder models were analyzed for the same parametric cases, a thermal performance comparison can be performed. In the following sections, various geometric modifications are considered along with their effects on the overall sample holder performance. Even though isolating a specific parameter to evaluate its impact can be presumptuous, simulation results along with the reviewed literature are used in conjunction to interpret the trends observed and provide a perspective for the physical phenomena involved.

4.4.1 Cu-rod Thermal Mass Consideration

When comparing the two sample holder models, it was evident the significant difference in the Cu-rod design and size. Specifically, the thermal mass of the Cu-rod in the Gen 2 sample holder is about 6.2 times larger than that of the Gen 1 sample holder

(from 1.419×10^{-5} m^3 to 1.419×10^{-5} m^3). The impact of this modification is apparent when comparing the maximum temperatures achieved in the Cu-rod with increasing IHF. The significant increase in the size of the Cu-rod improves the conduction through the solid body while decreasing the overall attained temperature due to its greater thermal capacity. As shown in Figures 23 and 29, the mean temperature difference, for peak values in the Cu-rod, was approximately 217 K lower for the Gen 2 sample holder. Consequently, a 40 % increase in the allowable IHF in the Cu-rod (from 6 MW/m^2 to 8.4 MW/m^2) was recorded for the Gen 2 sample holder. Another inherent benefit of increasing the Cu-rod size is manifested in the temperatures predicted along the cooled surface. Since a greater portion of the energy is diffused along the Cu-rod, the temperatures recorded along the cooled surface are lower for the Gen 2 sample holder. Overall, it was concluded that the increase in the size of the Cu-rod presents a significant enhancement in the thermal performance of the sample holder, therefore, this design modification should be considered in future sample holder designs.

4.4.2 Sample Holder Head Design Consideration

The most obvious design modification was presented by the sample holder head in the Gen 2 sample holder which is composed of three pieces: Mo-clamp, Mo-holder, and W-F82H-sample. It was concluded that the effect of the separation gap between the Mo-clamp and Mo-holder significantly affects the ability to remove heat from the sample holder. For instance, when the separation gap was decreased from 44 μm to 15 μm, reaching the melting temperature of molybdenum within the Mo-clamp was no longer the limiting factor. Also, there was an increase of about 55 % in the allowable IHF for the Gen 2 sample holder (from 5 MW/m^2 to 7.75 MW/m^2).

Therefore, unless the separation gap is decreased in the Gen 2 sample holder design, the allowable IHF is much lower than that of the Gen 1 sample holder. Overall, it was observed that using two pieces rather than one in the sample holder head design diminishes the ability for diffusing the energy along the sample holder head via conduction. From this perspective, it could be argued that the coupling between the Mo-holder and the Cu-rod is more efficient for the Gen1 sample holder as the allowable IHF reached is higher than that of Gen 2 sample holder. Nevertheless, if the separation distance is decreased, the Gen 2 sample holder would have a more efficient coupling between Mo-holder and Cu-rod.

4.4.3 Cu-rod Internal Dimensions Consideration

Another design modification in the Gen 2 sample holder was the increase on the internal dimensions for the Cu-rod and SS-cartridge. The best way to understand the overall impact in the thermal performance is by comparing the Re number against the average heat transfer coefficient along the cooled surface for the three mass flow rate cases considered. Each of the data 3 points plotted in Figure 38 for each sample holder model represents a specific mass flow rate case. The results are plotted in terms of the Re number in order to account for geometric effects. As depicted in Figure 38, the results suggest that the Gen 1 sample holder and Gen 2 sample holder are not dynamically similar. In other words, there is a significant difference between the two sample holders in their ability to remove heat under similar conditions, specifically, the results suggest that the Gen 1 sample holder contains a more adequate internal geometric configuration that allows it to remove heat via convective heat transfer more efficiently.

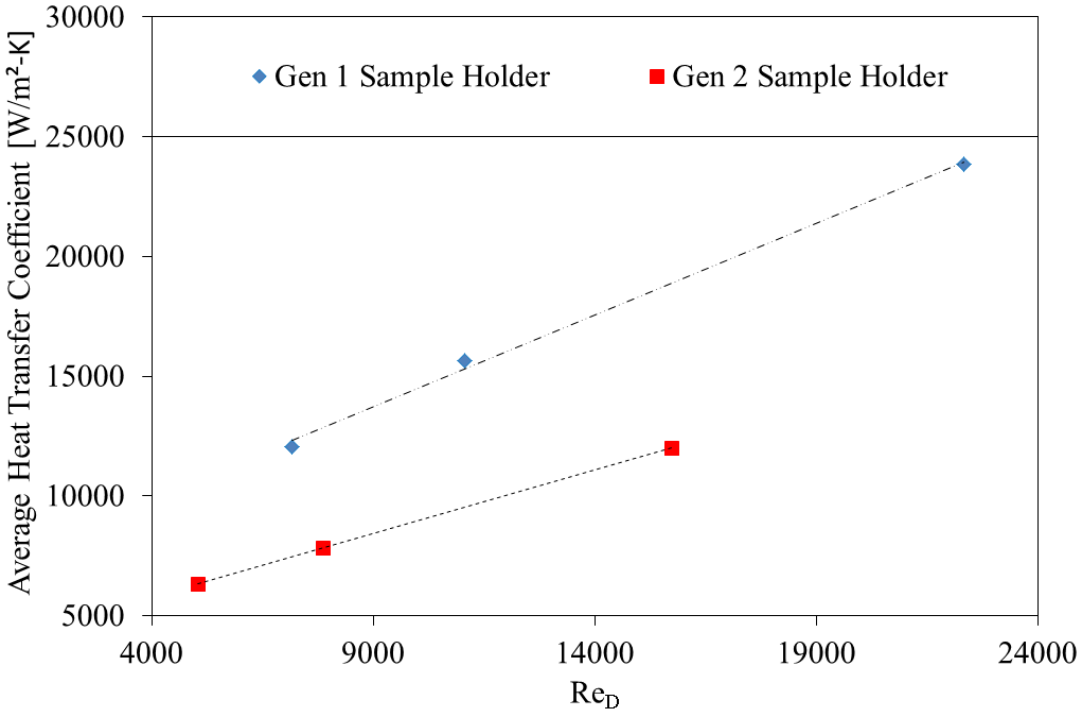

Figure 38. Sample holder designs comparison in the consideration of hydrodynamic effects with respect to heat removal capacity

It was clearly observed that the mass flow rate effect was the same on both sample holders, with the convective cooling capacity being increased with increasing Reynolds number. Even though the convective cooling capacity was lower for the Gen 2 sample holder, the overall cooling performance may be considered better as more heat is conducted along the Cu-rod and less is being removed at the cooled surface. Therefore, the temperatures along the cooled surface are lower causing the vapor formation, for all parametric cases considered, to be lower than for Gen 1 sample holder. This temperature trend can be used to gain insight for decreasing the possibility of bubble blanketing at the entry of the narrow annular channels. During the separation gap analysis, the average temperature along the cooled surface increased slightly (~ 18 K) for the nominal transient case (32 g/s at 80 psi) where the separation gap was decreased from 44 μm to 15 μm. Although higher temperatures along the cooled surface were recorded for the 15 μm

separation distance, the predicted vapor formation was still lower than that recorded for the Gen 1 sample holder under the same IHF. In addition, the allowable IHF was improved by 55 % with the decrease in separation distance.

Throughout this section the main design differences between the two sample holder models were discussed. It was concluded that the increased size of the Cu-rod presents a significant enhancement in the thermal performance of the sample holder. In addition, it was shown that the coupling between the Mo-holder and the Cu-rod is more efficient for the Gen1 sample holder. Finally, it was determined that the Gen 1 sample holder contains a more adequate internal geometric configuration that allows it to remove heat via convective heat transfer more efficiently. Although it seems as if the Gen 1 sample holder is the more adequate design of the configurations analyzed, it was concluded that with a reduction in the separation gap for the Gen 2 sample holder, its thermal performance would exceed that of the Gen 1 sample holder. Nevertheless, it is imperative to mention that both of the designs considered for HHF testing present limiting factors that bound the allowable IHF to values below those desired to achieve for HHF testing at the IMTS facility. Therefore, careful consideration of both sample holders characteristics should be taken in the design of future sample holders.

A summary of the research findings, conclusions, and suggestions for future sample holder design considerations and research are summarized in chapter 5.

CHAPTER 5: CONCLUSIONS AND RECOMMENDATIONS

This chapter summarizes the conclusions drawn from the previous chapters, discusses the major contributions of this research, and offers recommendations for future work. Two sample holder designs were analyzed in this work: the Gen 1 sample holder and Gen 2 sample holder. The objectives of this research were to:

- Develop numerical models characterizing the sample holders in order to determine safe limits for HHF testing at the IMTS facility.
- Use the numerical models developed to conduct a parametric analysis over a wide range of pressures, coolant flow rates, and incident heat fluxes in order to evaluate their thermal performance under a variety of parametric conditions.

5.1 Research Findings:

5.1.1 Limiting Parameter for Gen 1 and Gen 2 Sample Holders

A 2D axisymmetric numerical model was constructed for each water-cooled sample holder design using the CFD software package ANSYS™ FLUENT®. The numerical models predictions were compared against experimental temperature measurements obtained from the IMTS facility. Using these numerical models, a limiting parameter analysis was conducted to determine the allowable IHF limit for HHF testing under a variety of coolant mass flow rates and pressure conditions. Specifically, three mass flow rate cases were considered; 32 g/s, 50 g/s, and 100 g/s. In addition, the effects of mass flow rate variation were studied for three pressure scenarios (80 psi, 140 psi, and 200 psi). The independent parameter used, the incident heat flux (IHF), was increased from one testing

interval to the next. The transient testing interval considered for this study consisted of an irradiation period (15 seconds) and a dwell period (120 seconds) with a total duration of 135 seconds. The two limiting parameters considered were the maximum temperature within each of the sample holder components and the critical heat flux. These two parameters were compared for different values of the allowable IHF. The limiting parameter analysis results, for all parametric cases considered for the Gen 1 sample holder, suggested that:

- the maximum temperature achieved within the Cu-rod is the limiting parameter for HHF testing using the Gen 1 sample holder. It was found that the allowable IHF is approximately 6 MW/m^2 as the Cu-rod reaches its melting point at this IHF.
- a small increase in the allowable IHF was observed, about 0.5 MW/m^2, when increasing the coolant mass flow rate from 32 g/s to 100 g/s.
- the effects of pressure on the maximum temperature within the sample holder components was observed to be negligible for the range of pressure values considered.
- the CHF is not a limiting parameter for any of the sub-cooled parametric cases considered as predicted by the Škéma and Šlančiauskas correlation.
- the system reaches CHF at the stagnation point more rapidly for lower IHF values when the mass flow rate is increased. Nevertheless, CHF is not the limiting phenomenon in setting the maximum IHF.

As previously mentioned, the same type of analysis was conducted for both sample holder models. The limiting parameter analysis results, for all parametric cases considering the Gen 2 sample holder, suggested that:

- the maximum temperature achieved within the Mo-clamp is the limiting parameter for HHF testing using the Gen 2 sample holder. It was concluded that the allowable IHF is approximately 5 MW/m^2. At this IHF value, the Mo-clamp reaches its melting point.
- no significant increase in the allowable IHF was observed when evaluating effects of the coolant mass flow rate variation on the maximum temperature.
- the effects of pressure on the maximum temperature within the sample holder components was observed to be negligible for the range of pressure values considered.
- the CHF is not a limiting parameter for any of the sub-cooled parametric cases considered. That is, for the CHF values predicted by the Škéma and Šlančiauskas correlation.
- when mass flow rate is increased, the system reaches CHF at the stagnation point more rapidly for lower IHF values.
- the maximum heat flux depends on the assumed contact resistance between the cooling rod components. Better control of machining and assembly is needed to minimize the contact resistance.

Although the assumptions associated with each of the numerical models and the uncertainties related to the experimental data suggest that further validation of both models

would be necessary, the conclusions drawn from the limiting parameter analysis are likely to remain unchanged as the level of reliability on the ANSYS™ FLUENT® software is rather good when solving conduction problems as the one presented in the prediction of maximum temperatures within the sample holders solid components [43, 51, 52].

It was also concluded that the Škéma and Šlančiauskas correlation provides a conservative estimate for CHF as the parametric differences between the geometry for which the correlation was developed and the geometry presented by the sample holders are reflected positively, enhancing the cooling performance of the sample holders. Therefore, an inherent safety factor is associated with the use of the Škéma and Šlančiauskas correlation in the prediction of the CHF for both sample holders. Nevertheless, as noted earlier, CHF is not the limiting phenomenon for establishing the maximum allowable heat flux for either of the sample holder designs examined.

5.1.2 Parametric Study for Gen 1 and Gen 2 Sample Holders

Using the results obtained from the limiting parameter analysis, an applicable range of study was determined for each sample holder design. Numerical simulations were performed using ANSYS™ FLUENT® 14.0 to conduct a parametric study considering the mass flow rate, system pressure, and incident heat flux. In addition, a separation gap analysis was conducted for the Gen 2 sample holder. The ranges of mass flow rates and pressures used during the parametric study were the same as those used for the limiting parameter analysis. The independent parameter, the IHF, was increased between transient intervals for a set parametric case to determine the safe limit for HHF testing. The transient testing interval considered for this study was the same as the one considered in the limiting parameter analysis. The numerical model was partially validated using experimentally

measured values for the temperature in the solid components. For the Gen 1 sample holder, its 2D numerical model predicted:

- in the applicable range of study, increasing the mass flow rate is reflected in the extent of vapor formation (i.e. maximum void fraction) in reference to the IHF. For instance, when increasing the mass flow rate from 32 g/s to 100 g/s. For a vapor volume fraction of 5 %, the IHF needed to achieve such void fraction increases from 2.11 MW/m^2 to 3.71 MW/m^2.
- an average decrease of 19.7 % in the allowable IHF results across the range of mass flow rates considered, that is, when considering only the CHF as a limiting parameter.
- when considering the CHF as the only limiting parameter, an average increase of 2.44 % in the allowable IHF results from a net increase of 60 psi in pressure for a fixed mass flow rate. In addition, as expected, a reduction in the maximum void fraction for a fixed IHF was observed with the increase in pressure.

The results from the 2D simulations for the Gen 2 sample holder model displayed a similar trend as that observed on the simulations for the first model. An analysis considering the effects of the separation gap between the Mo-clamp and Mo-holder was conducted during the parametric analysis of the Gen 2 sample holder. The 2D numerical model constructed for the Gen 2 sample holder predicted:

- the major impact of increasing the mass flow rate is reflected in the formation of vapor in reference to the IHF. For instance, when increasing the mass flow rate

from 32 g/s to 100 g/s, considering a vapor fraction of 5 %, the IHF needed to achieve such vapor formation increases from 3.05 MW/m^2 to 4.49 MW/m^2.

- an average decrease of 37.4 % in the allowable IHF results across the range of mass flow rates considered, that is, when considering only the CHF as a limiting parameter.

- when considering the CHF as the only limiting parameter, an average increase of 1.85 % in the allowable IHF results from a net increase of 60 psi in pressure for a fixed mass flow rate. In addition, a reduction on the vapor formation for a fixed IHF was observed with the increase in pressure.

- the decrease in the separation gap from 44 μm to 15 μm causes the maximum temperature within the Cu-rod to become the limiting parameter which in turn increases the allowable IHF limit by 55 % (from 5 MW/m^2 to 7.75 MW/m^2).

5.1.3 Effects of Geometric Designs for Gen 1 and Gen 2 Sample Holders

In this section the advantages and disadvantages associated with the main design modifications between the two sample holders models are considered in order to evaluate their impact in the overall thermal performance of each sample holder. The design modifications considered are: an increase in the Cu-rod thermal mass, the sample holder head design, and the Cu-rod internal dimensions. The conclusion drawn from each modification indicate that:

- an increase in the Cu-rod thermal mass in the Gen 2 sample holder presents a significant enhancement in the thermal performance of the sample holder,

therefore, this design modification should be retained in future sample holder designs.

- the coupling between the Mo-holder and the Cu-rod is more efficient for the Gen1 sample holder since the allowable IHF limit, dictated by the maximum temperature within the solid components, is higher than that of Gen 2 sample holder.
- there is a significant difference between the two sample holders in their ability to remove heat under similar conditions, specifically, the results suggest that the Gen 1 sample holder contains a more adequate internal geometric configuration that allows it to remove heat via convective heat transfer more efficiently.

Although it seems as if the Gen 1 sample holder were the more adequate design of the configurations analyzed, it was concluded that with a reduction in the separation gap for the Gen 2 sample holder, its thermal performance exceeds that of the Gen 1 sample holder. Therefore, careful consideration must be given to this suggested design modification for future sample holders. Nevertheless, it is imperative to mention that both of the designs considered for HHF testing present limiting factors that bound the allowable IHFs to values below those desired to achieve for HHF testing at the IMTS facility.

5.2 Major Contributions

The thermal performance of two sample holder designs used during HHF testing were numerically investigated in this thesis. The numerical assessment conducted on the sample holder designs is the first of its kind. Therefore, the numerical models developed

are valuable tools to the research work conducted at the IMTS facility as it facilitates the quantification of safety limits for HHF testing. The contributions of this work includes:

- reference charts defining the limiting parameter for each sample holder model and its associated allowable IHFs considering various parametric scenarios (e.g., pressure, mass flow rate).
- allowable IHF charts that estimate the maximum incident heat flux each sample holder can accommodate under various mass flow rates, pressures, and vapor volume fractions constraints.
- a numerical model developed for each sample holder design that can be used to estimate thermal performance for a various parametric conditions, that is, considering the effect of the assumptions made during each model development.

Although the numerical models developed are useful tools in the evaluation of each sample holder model, further validation of each model would be fundamental in the thermal performance assessment and conclusions drawn for future studies.

5.3 Recommendations for Future Work

In terms of future work, the following suggestions and recommendations would complement and extend this masters research.

- Given that no uncertainties related to the thermocouple readings, nor calibration, were provided in the literature for the experimental work conducted during HHF testing at the IMTS facility, it is important to conduct experiments where all uncertainty measurements related to the experimental setup are recorded and

documented for each sample holder model. Providing such information would allow for better interpretation of simulation results and further validation of each numerical model.

- Increasing the pressure of the system during HHF testing may be beneficial to the overall thermal performance of the sample holders. In addition, increasing the mass flow rate may further decrease the possibilities for bubble blanketing at the narrow annular channels, that is, while considering the limit on the allowable IHF imposed by the CHF.

- Given that the limiting parameter for both sample holder models was the material selection, the current allowable IHFs values are well below those desired to achieve for HHF testing at the IMTS facility. Therefore, it is imperative to consider not only other materials with higher melting points for the sample holder components (e.g., Tungsten alloys) but also a complete redesign of the sample holder for future iterations.

- Given the observed effects of thermal resistance on the results of the current numerical model, it is suggested that the effect of thermal resistance to be further investigated. Explicitly, developing experimental processes to measure the gap distance for all surfaces at the interface of the Mo-holder and the Cu-rod may be useful for the refinement of the numerical models. The inclusion of better estimates of the thermal resistances in the numerical models would significantly enhance accuracy of the simulations results and characterization of experimental trends.

- Conduct experimental work to develop a new correlation for the prediction of the CHF, specific to the geometry presented by the sample holders, based on mass flow rate and pressure related parameters. Such correlation may be used to extrapolate to a variety of operating conditions.
- Developing specific guidelines for developing safety factors. Even though the design has to be below the melting temperature of its components materials (e.g., Copper, Molybdenum, etc.), in reality, the designer should keep the maximum temperatures well below the melting temperatures. Stress analyses taking into account changes in the material properties with temperature should be performed.
- Validate the numerical model predictions using a different software package (e.g., OpenFOAM®) to ensure the validity of the code, specially, when the boiling model is included.
- Accounting for losses within the model due to radiation heat transfer.

APPENDIX A: DIMENSIONAL DRAWINGS

Dimensional drawings for the Gen 1 sample holder thermocouple locations, all dimensions given in SI units (mm) [46]:

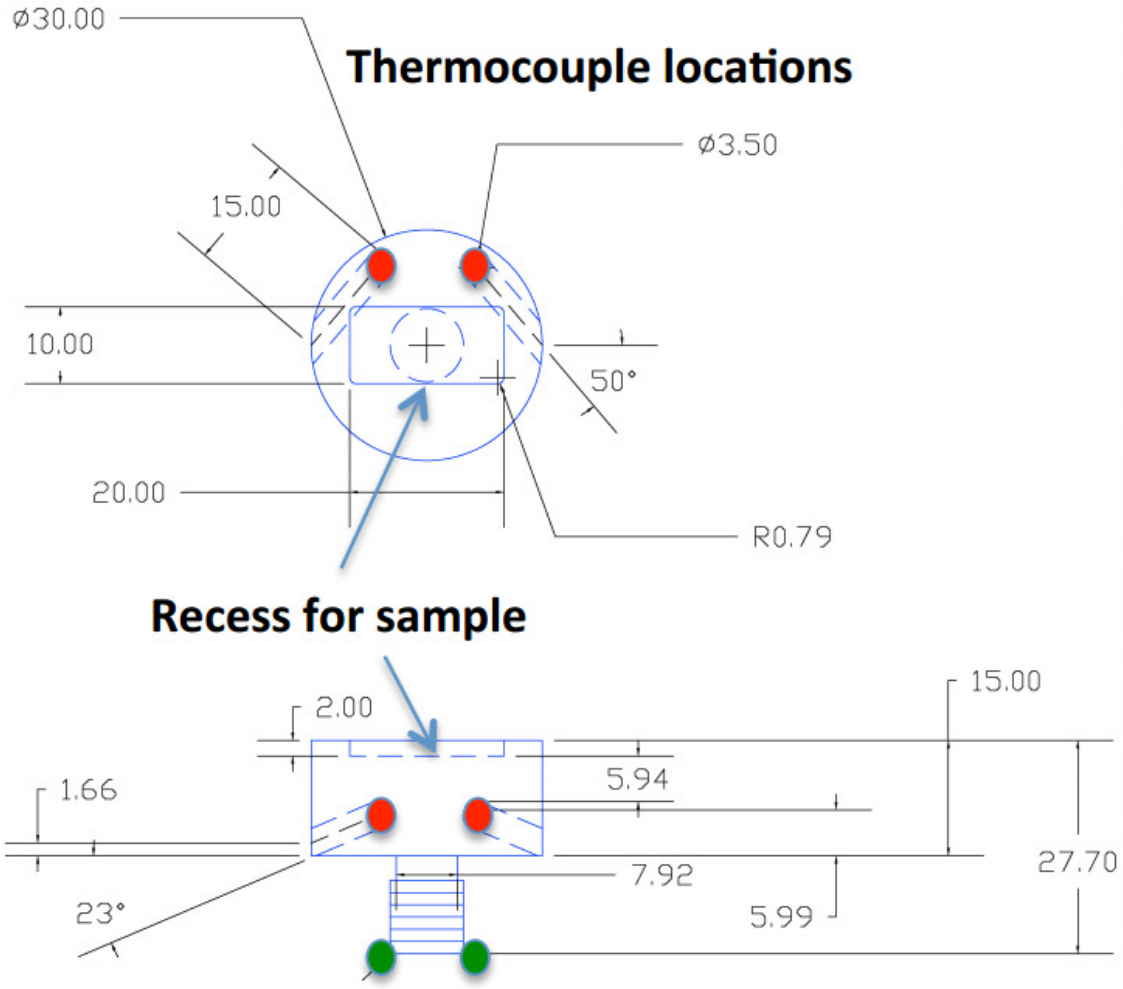

Gen 1 sample holder dimensional drawing with all measurement specified in SI units (m):

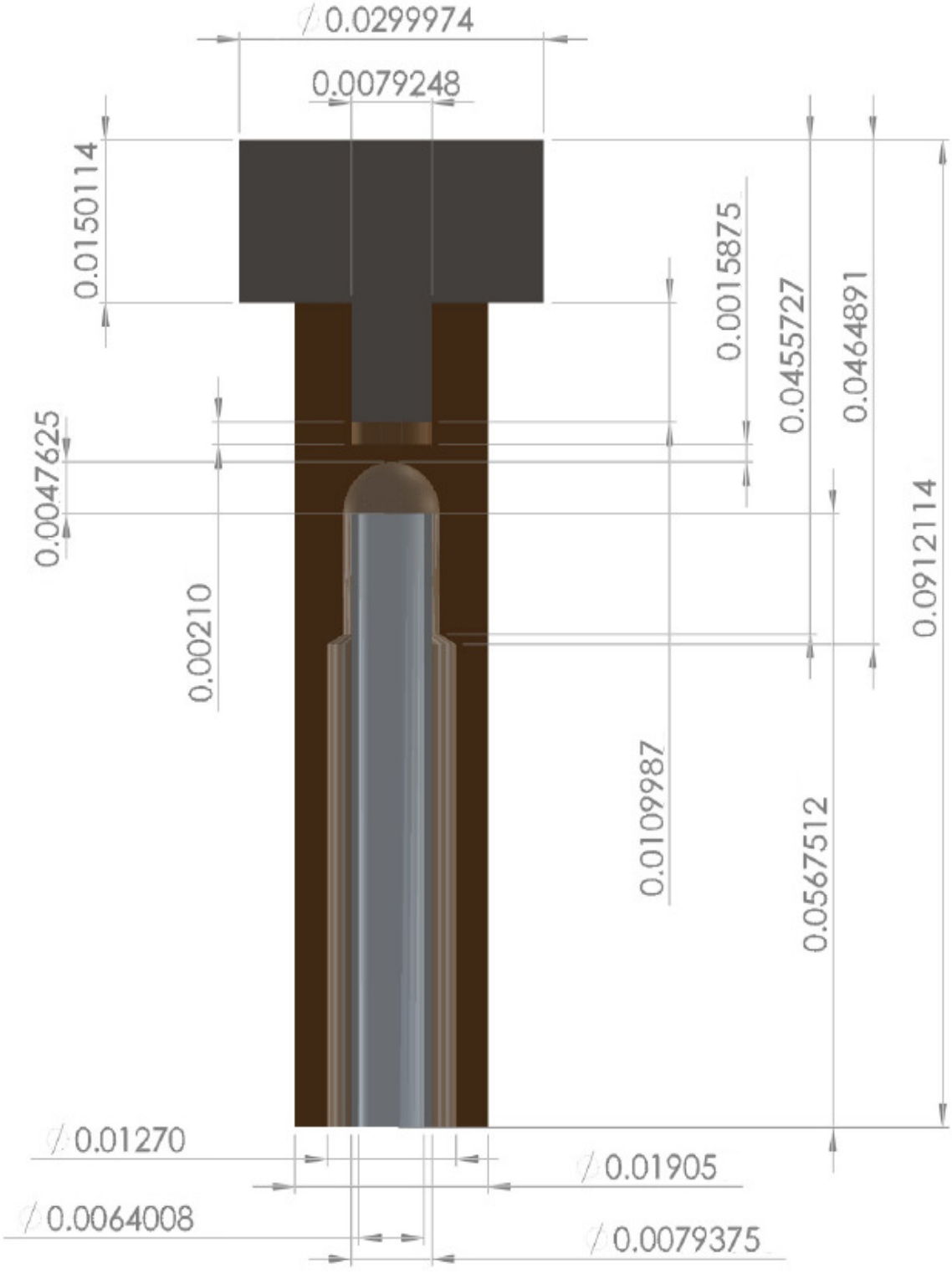

Dimensional drawings for the Gen 1 sample holder thermocouple locations, all dimensions given in British units (inches) [47]:

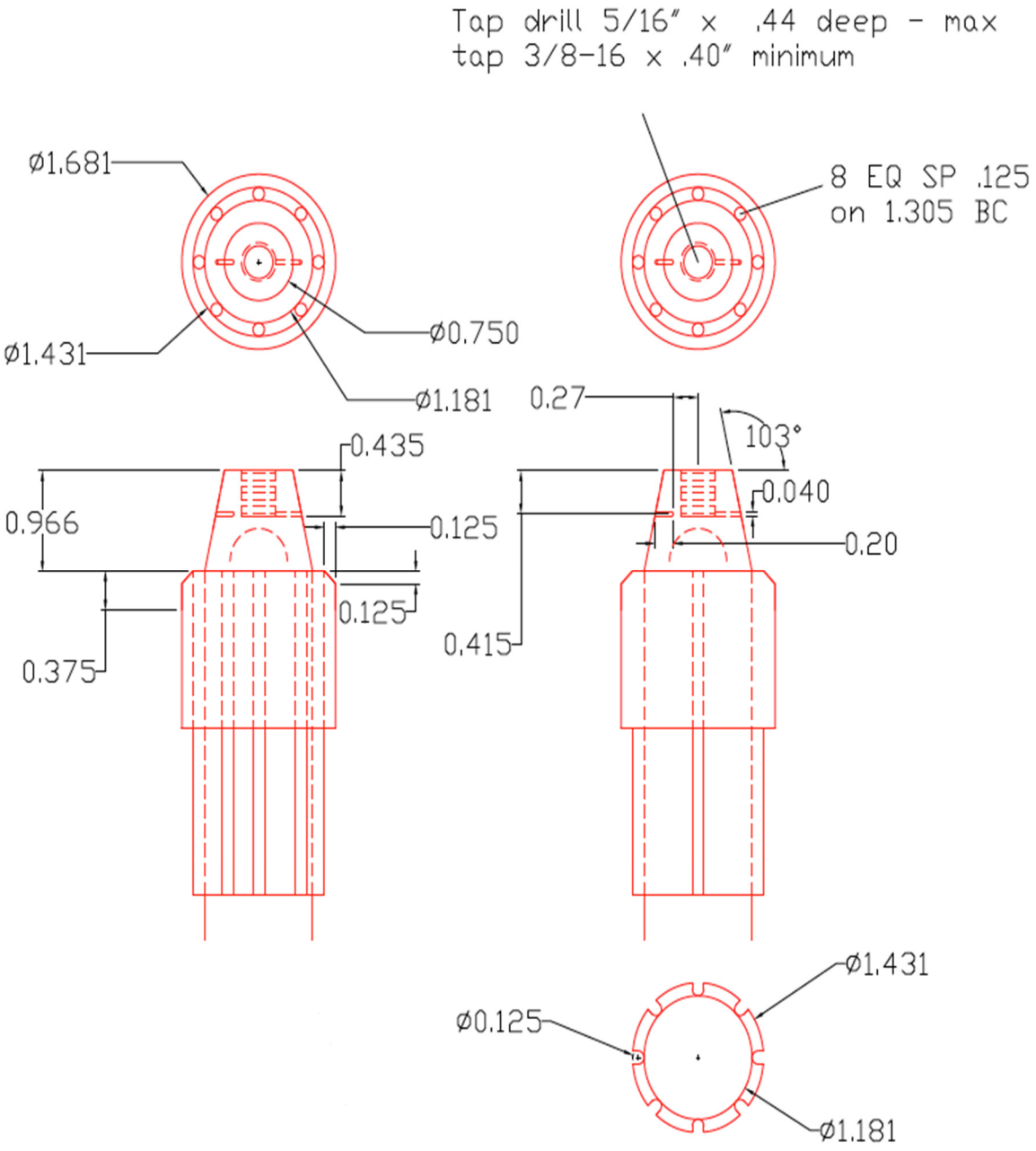

Gen 2 sample holder dimensional drawing with all measurement specified in SI units (m):

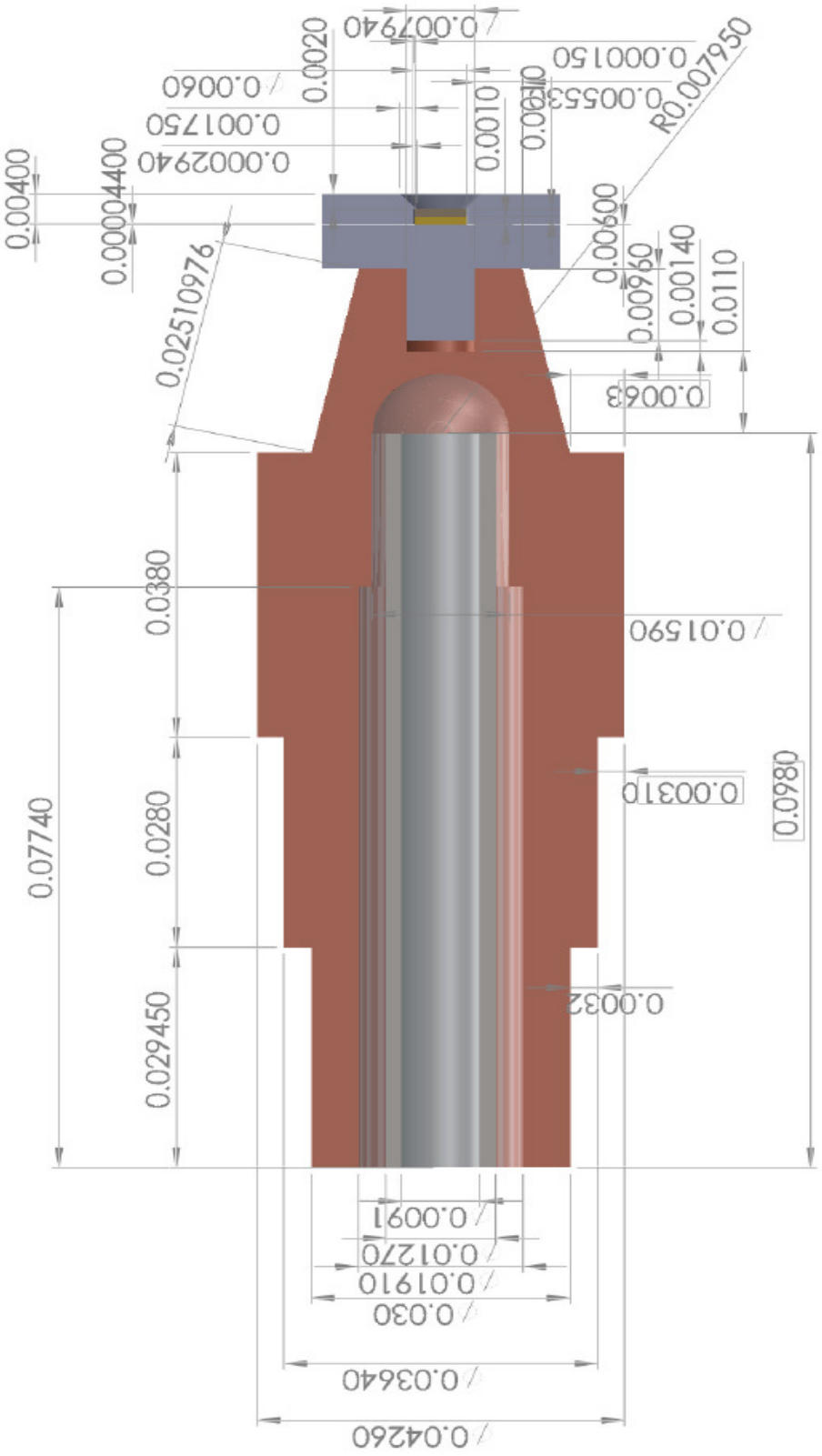

APPENDIX B: MATERIAL PROPERTIES

Many of the materials in this work are evaluated over a wide range of temperatures. As such, it is imperative to include temperature dependent properties in the calculations. The properties for the coolants and the solid materials used in this work were compiled from a number of different sources in the literature and are summarized below.

B.1 Coolant Properties

Water was the active coolant used during HHF testing at the IMTS. Three pressure cases were considered: 80 psi, 140 psi, and 200 psi. Therefore, properties were evaluated based on their temperature and pressure. In the case of vapor, properties were evaluated only based on their temperature.

The properties for water and vapor, each of the phases identified, are included in Table 11 and Table 12, respectively. The Engineering Equation Solver (EES) software was used to evaluate the physical properties for all the parametric conditions considered.

Table 11. Temperature dependent properties for water [55]

T (K)	551580 Pa (80 psi)			965266 Pa (140 psi)			1378951 Pa (200 psi)		
	c_P (J/kg·K)	μ (μPa·s)	k (W/m·K)	c_P (J/kg·K)	μ (μPa·s)	k (W/m·K)	c_P (J/kg·K)	μ (μPa·s)	k (W/m·K)
273	4217	1787	0.5614	4215	1786	0.5616	4213	1785	0.5619
300	4179	853.7	0.6105	4178	853.7	0.6107	4177	853.6	0.6109
350	4193	368.9	0.6683	4193	369.0	0.6685	4192	369.1	0.6687
400	4255	218.7	0.6838	4254	218.8	0.6841	4252	218.9	0.6843
450	2254	15.07	0.03359	4393	153.0	0.6746	4391	153.1	0.6749
500	2115	17.16	0.03728	2265	170.6	0.03868	2449	16.96	0.04018
550	2078	19.26	0.04186	2158	19.20	0.04272	2247	19.14	0.04363
600	2076	21.37	0.04699	2125	21.33	0.04759	2177	21.30	0.0482
650	2090	23.47	0.05252	2123	23.45	0.05296	2157	23.43	0.05342
700	2111	25.56	0.05835	2135	25.55	0.0587	2159	25.55	0.05907

Table 12. Temperature dependent properties for vapor [55]

T (K)	c_P (J/kg·K)	μ (μPa·s)	k (W/m·K)
273	1863	8.958	0.01673
300	1868	9.929	0.01861
350	1881	11.78	0.02241
400	1899	13.67	0.02657
450	1923	15.6	0.03107
500	1950	17.56	0.03588
550	1980	19.53	0.04099
600	2012	21.53	0.04636
650	2046	23.53	0.05199
700	2081	25.53	0.05784

B.2 Test Section Material Properties

For the Gen 1 sample holder, three test section materials were included in this work: Molybdenum, SS304L stainless steel, and C10100 copper alloy. Since transient experiments and simulations were performed, the two properties evaluated for each test sample holder were the thermal conductivity and specific heat. For these three materials, discrete thermal conductivity data and discrete specific heat data were obtained from the literature and linear-piecewise functions were created within ANSYS™ FLUENT®. The data for the Molybdenum, SS304L stainless steel, and the C10100 copper alloy are provided in Table 13, Table 14, and Table 15, respectively.

Table 13. Temperature dependent properties for Molybdedum [53, 54]

T (K)	k (W/m·K)	T (K)	c_P (J/kg·K)
273.2	136.8	250	221.8
373.2	137.2	300	248.1
473.2	131.0	400	259.8
573.2	123.0	500	263.2
623.2	119.0	600	267.4
861	122.0	800	276.1
977.6	115.4	1000	287.9
1144.3	108.9	1200	301.7
1473.2	89.0	1600	339.7

1673.2	84.0	2000	388.3
1873.2	80.0	2400	456.1
2073.2	77.5	2800	581.6
2473.2	74.0	2860	606.7

Table 14. Temperature dependent properties for SS304L [49]

T (K)	k (W/m·K)	T (K)	c_P (J/kg·K)
300	14.9	300	477
400	16.6	400	515
600	19.8	600	557
800	22.6	800	582
1000	25.4	1000	611

Table 14. Temperature dependent properties for C10100 copper alloy [49]

T (K)	k (W/m·K)	T (K)	c_P (J/kg·K)
300	391.1	300	393.5
400	387	400	397
600	379	600	417
800	366	800	433
1000	352	1000	451

For the Gen 2 sample holder, five test section materials were included in this work: Molybdenum, SS304L stainless steel, C10100 copper alloy, W tungsten, and F82H steel. For these five materials, discrete thermal conductivity data and discrete specific heat data were obtained from the literature and linear-piecewise functions were created within ANSYS™ FLUENT®. The data for the F82H steel and W Tungsten in Table 16, and Table 17, respectively.

Table 16. Temperature dependent properties for F82H steel [50]

T (K)	k (W/m·K)	c_P (J/kg·K)
273	31.35	466.8
300	31.59	458.1
400	32.39	474.2
500	32.97	522.6
600	33.28	567.2
700	33.26	601
800	32.88	645.5
900	32.08	750.7
1000	30.81	995.4
1100	29.01	1486.9
1143.2	28.07	1808.3

Table 17. Temperature dependent properties for W Tungsten [53, 54]

T (K)	k (W/m·K)	T (K)	c_P (J/kg·K)
273.2	166.3	273.2	133.8
300	161.7	373.2	135.9
400	148.3	473.2	137.9
500	138.7	573.2	139.9
877.2	120.8	810.9	142.3
1173.2	115.0	1088.7	158.9
1373.2	107.0	1366.5	188.3
1773.2	99.6	1644.3	205.1
1973.2	96.2	1922.0	205.1
2173.2	94.1	2199.8	205.1
2563.2	92.5	2477.6	196.6
2978.2	92.5	2755.4	192.5
3223.2	87.5	3033.1	502.1

B.3 Separation Gaps Material Properties

For the separation gaps between the Mo-clamp and Mo-holder, Mo-holder and Cu-rod insertion, air was the material used. Table 18 shows the data used to developed linear piecewise functions within ANSYS™ FLUENT® for the relevant thermo-physical properties.

Table 18. Temperature dependent properties for air [49]

T (K)	k (W/m·K)	c_P (J/kg·K)
250	0.0223	1006
300	0.0263	1007
400	0.0338	1014
500	0.0407	1030
600	0.0469	1051
800	0.0573	1099
1000	0.0667	1141
1200	0.0763	1175
1400	0.0910	1207
1600	0.106	1248
1800	0.120	1286
2000	0.137	1337
2200	0.160	1417
2400	0.196	1558
2500	0.222	1665
3000	0.486	2726

APPENDIX C: USER DEFINED FUNCTION

The user defined function (UDF) used as an input file is provided below. This file defines the properties of the material composing the sample holders in the numerical models developed within ANSYS™ FLUENT®.

(

(air-real fluid

(chemical-formula . #f)

(density (constant . 1.1614))

(specific-heat (polynomial piecewise-linear (250 . 1006) (300 . 1007) (400 . 1014) (500 . 1030) (600 . 1051) (700 . 1075) (800 . 1099) ((900 . 1121) (1000 . 1141) (1100 . 1159) (1200 . 1175) (1300 . 1189) (1400 . 1207) (1500 . 1230) (1600 . 1248) (1700 . 1267) (1800 . 1286) (1900 . 1307) (2000 . 1337) (2200 . 1417) (2400 . 1558) (2500 . 1665) (3000 . 2726)))

(thermal-conductivity (polynomial piecewise-linear (250 . 0.0223) (300 . 0.0263) (400 . 0.0338) (500 . 0.0407) (600 . 0.0469) (700 . 0.0524) (800 . 0.0573) (900 . 0.062) (1000 . 0.0667) (1100 . 0.0715) (1200 . 0.0763) (1300 . 0.082) (1400 . 0.091) (1500 . 0.1) (1600 . 0.106) (1700 . 0.113) (1800 . 0.12) (1900 . 0.128) (2000 . 0.137) (2200 . 0.16) (2400 . 0.196) (2500 . 0.222) (3000 . 0.486)))

(viscosity (polynomial piecewise-linear (250 . 1.596e-05) (300 . 1.846e-05) (400 . 2.301e-05) (500 . 2.701e-05) (600 . 3.058e-05) (700 . 3.388e-05) (800 . 3.698e-05) (900 . 3.981e-05) (1000 . 4.244e-05) (1100 . 4.49e-05) (1200 . 4.73e-05) (1300 . 4.96e-05) (1400 . 5.3e-05) (1500 . 5.57e-05) (1600 . 5.84e-05) (1700 . 6.11e-05) (1800 . 6.37e-05) (1900 .

6.63e-05) (2000 . 6.89e-05) (2200 . 7.4e-05) (2400 . 7.92e-05) (2500 . 8.18e-05) (3000 . 9.55e-05)))

(molecular-weight (constant . 28.966))

)

(F82H-Steel solid

(chemical-formula . #f)

(density (constant . 7871))

(specific-heat (polynomial piecewise-linear (273 . 466.8) (300 . 458.1) (350 . 458.8) (400 . 474.2) (450 . 497.3) (500 . 522.6) (550 . 546.5) (600 . 567.2) (650 . 584.8) (700 . 601.0) (750 . 619.5) (800 . 645.5) (850 . 686.3) (900 . 750.7) (950 . 849.6) (1000 . 995.4) (1050 . 1202.5) (1100 . 1486.9) (1143.2 . 1808.3)))

(thermal-conductivity (polynomial piecewise-linear (273 . 31.3525) (300 . 31.5975) (350 . 32.0201) (400 . 32.3939) (450 . 32.7126) (500 . 32.97) (550 . 33.1599) (600 . 33.2761) (650 . 33.3122) (700 . 33.2623) (750 . 33.1199) (800 . 32.8789) (850 . 32.5330) (900 . 32.0761) (950 . 31.502) (1000 . 30.8043) (1050 . 29.9769) (1100 . 29.0136) (1143.2 . 28.0682)))

)

(AISI-304 solid

(chemical-formula . #f)

(density (constant . 7900))

(specific-heat (polynomial piecewise-linear (300 . 477) (400 . 515) (600 . 557) (800 . 582) (1000 . 611)))

(thermal-conductivity (polynomial piecewise-linear (300 . 14.9) (400 . 16.6) (600 . 19.8) (800 . 22.6) (1000 . 25.4)))

)

(Cooper-C-10100 solid

(chemical-formula . #f)

(density (constant . 8940.61))

(specific-heat (constant . 393.5))

(thermal-conductivity (constant . 391.1))

)

(Molybdenum-Mo solid

(chemical-formula . #f)

(density (constant . 10220))

(specific-heat (polynomial piecewise-linear (250 . 221.8) (400 . 259.8) (600 . 267.4) (800 . 276.1) (1200 . 301.7) (1600 . 339.7) (2400 . 456.1) (2860 . 606.7)))

(thermal-conductivity (polynomial piecewise-linear (273 . 136.8) (473 . 131) (623 . 119) (861 . 122)(1144 . 108.9) (1673 . 84) (2073 . 77.5) (2473 . 74)))

)

(Tungsten solid

(chemical-formula . W)

(density (constant . 19300))

(specific-heat (polynomial piecewise-linear (100 . 87) (200 . 122) (300 . 132) (400 . 137) (600 . 142) (800 . 145) (1000 . 148) (1200 . 152) (1500 . 157) (2000 . 167) (2500 . 176)))

(thermal-conductivity (polynomial piecewise-linear (100 . 208) (200 . 186) (300 . 174) (400 . 159) (600 . 137) (800 . 125) (1000 . 118) (1200 . 113) (1500 . 107) (2000 . 100) (2500 . 95)))

)

APPENDIX D: DIAGRAMS FOR TEMPERATURE AND HEAT TRANSFER COEFFICIENT DISTRIBUTION

Gen 1 sample holder - Cycle 2 (2.43 MW/m^2 incident heat flux):

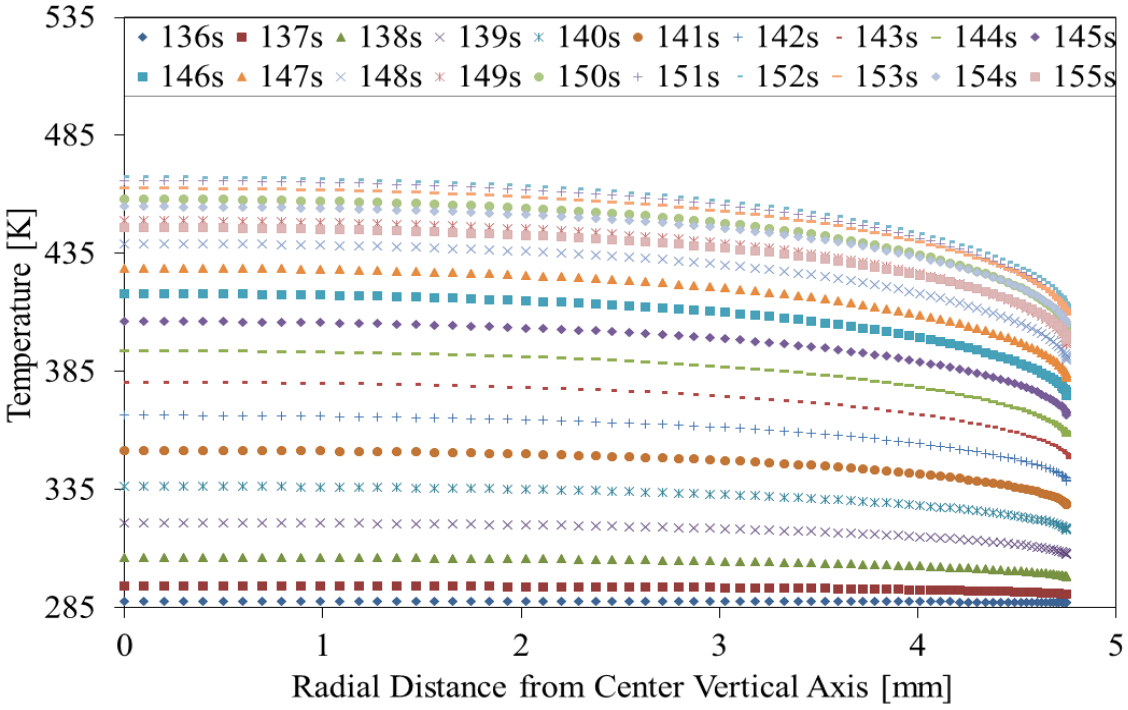

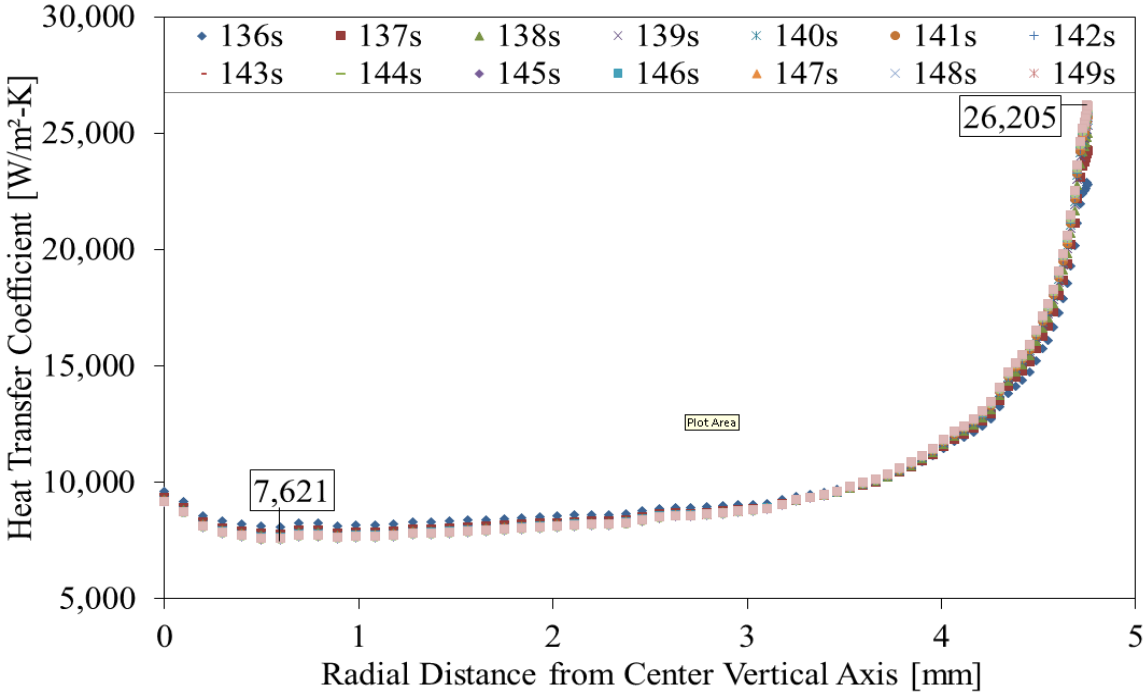

Gen 1 sample holder - Cycle 3 (2.30 MW/m^2 incident heat flux):

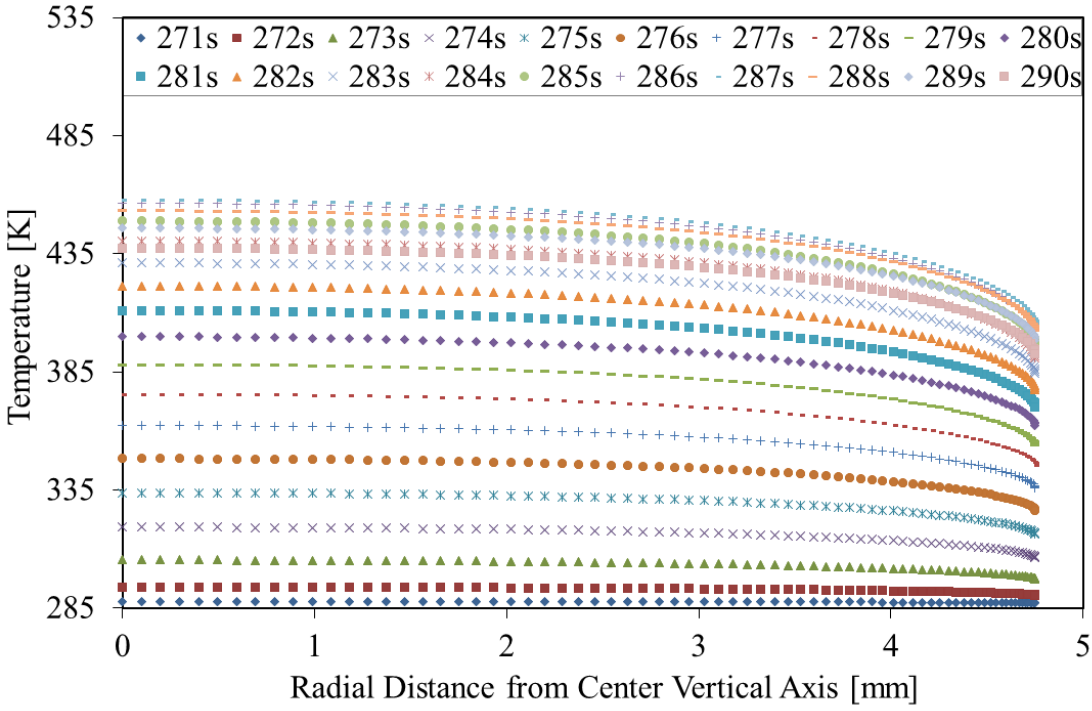

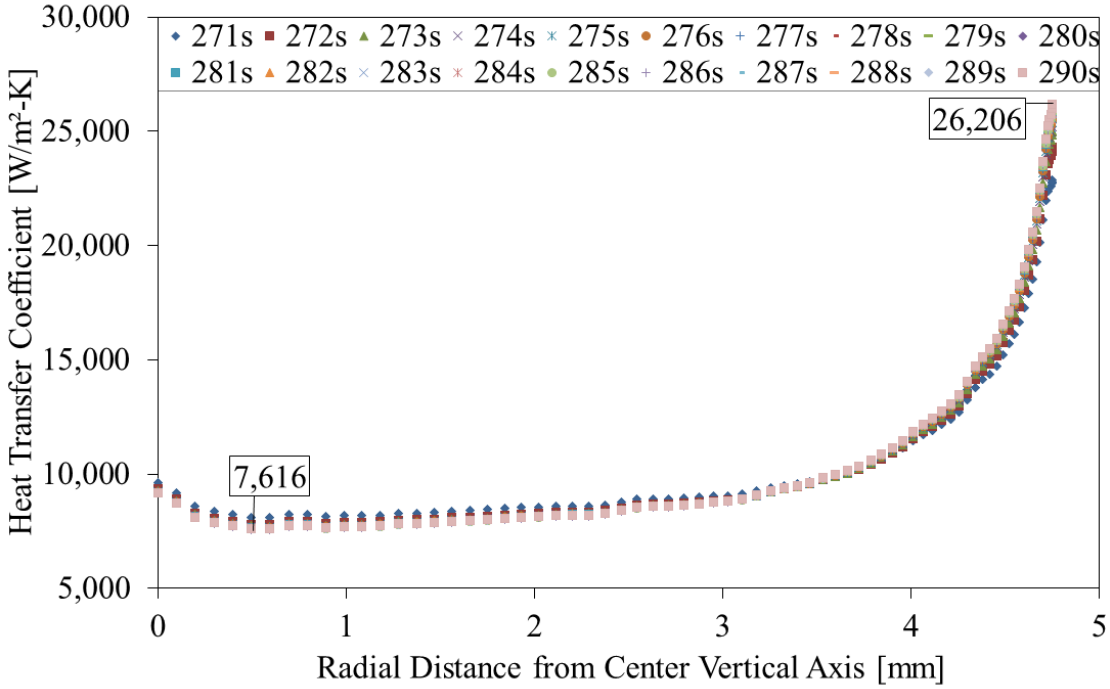

Gen 1 sample holder - Cycle 4 & 5 (2.17 MW/m^2 incident heat flux):

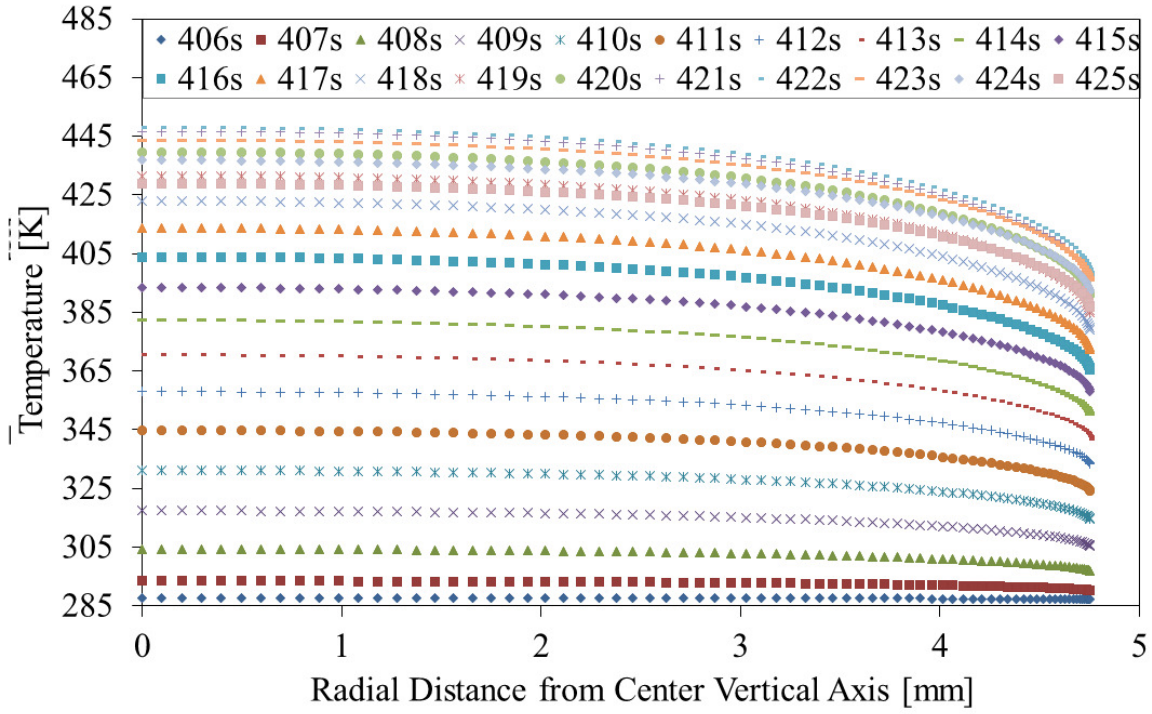

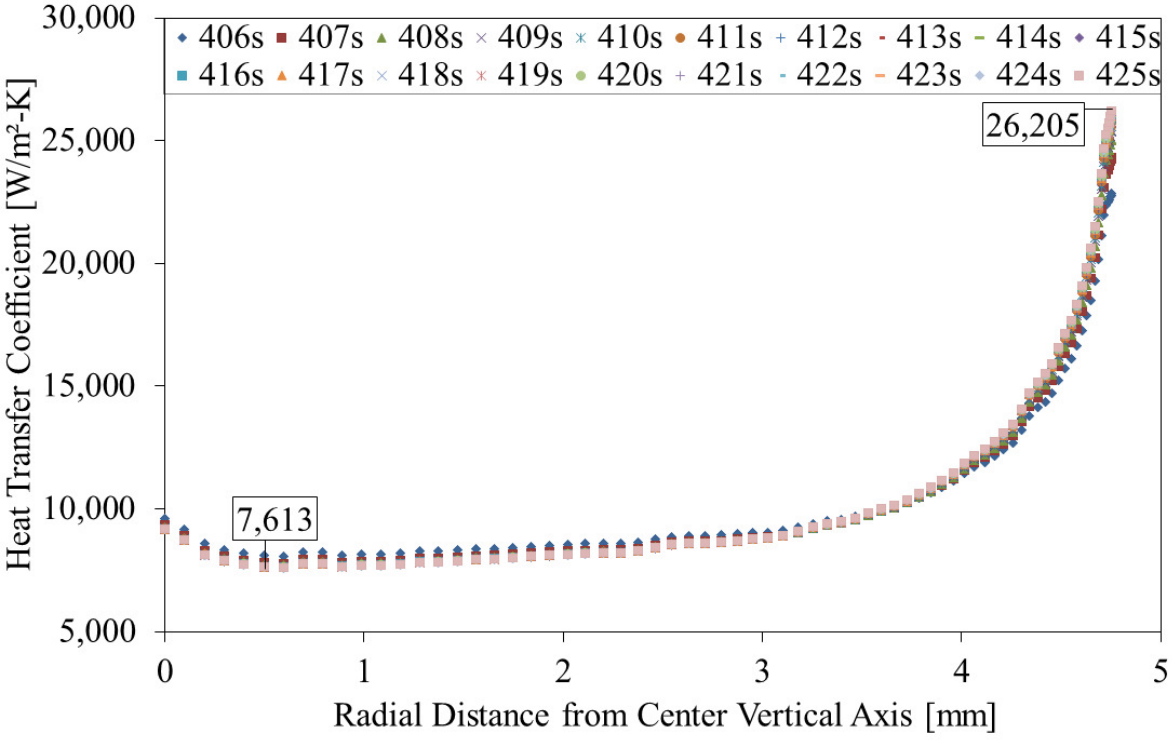

Gen 2 sample holder - Cycle 2 & 3 (1.51 MW/m^2 incident heat flux):

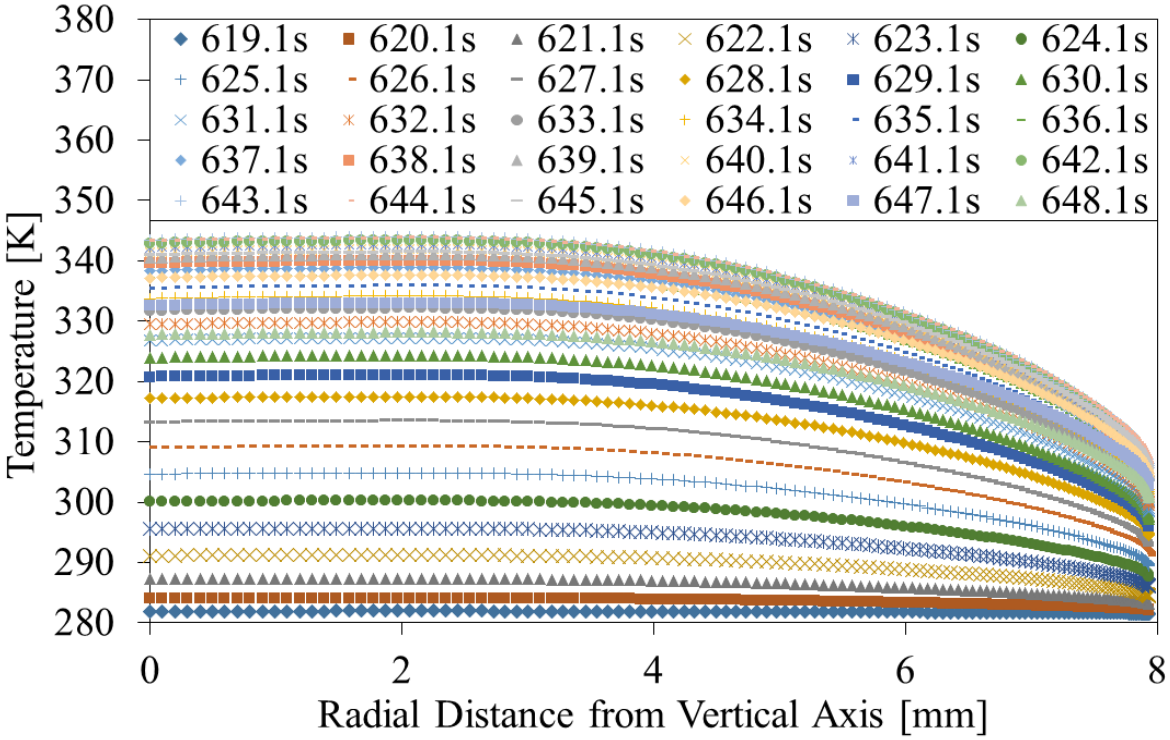

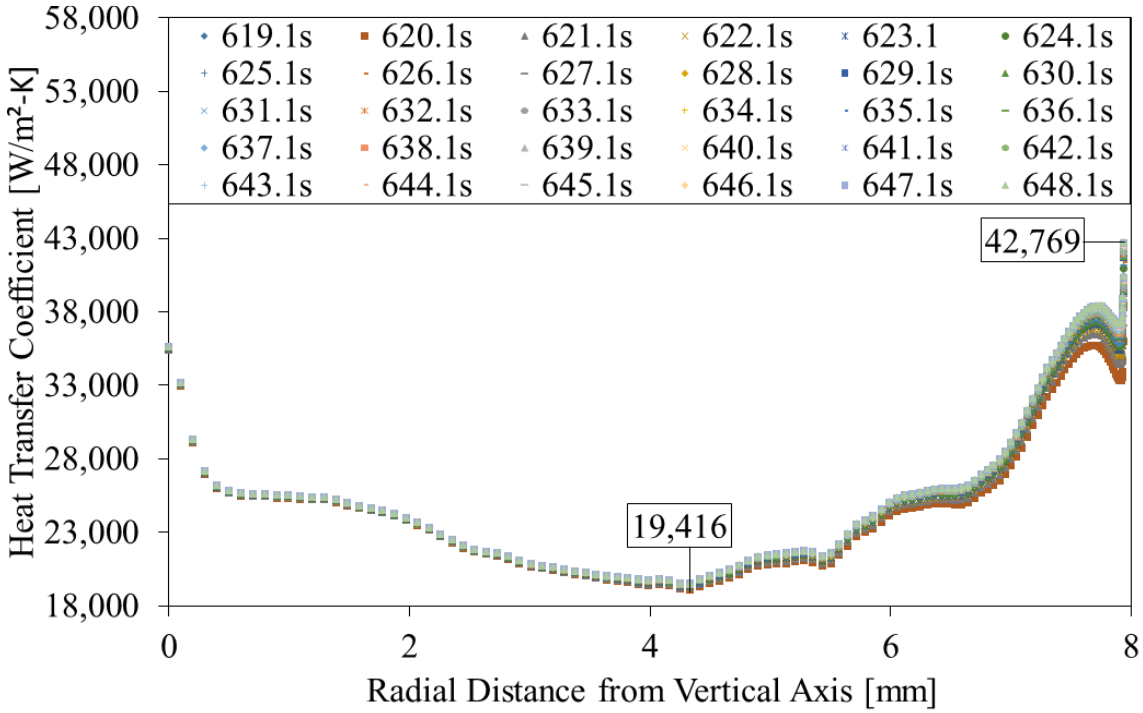

Gen 2 sample holder - Cycle 4 -6 (1.42 MW/m^2 incident heat flux):

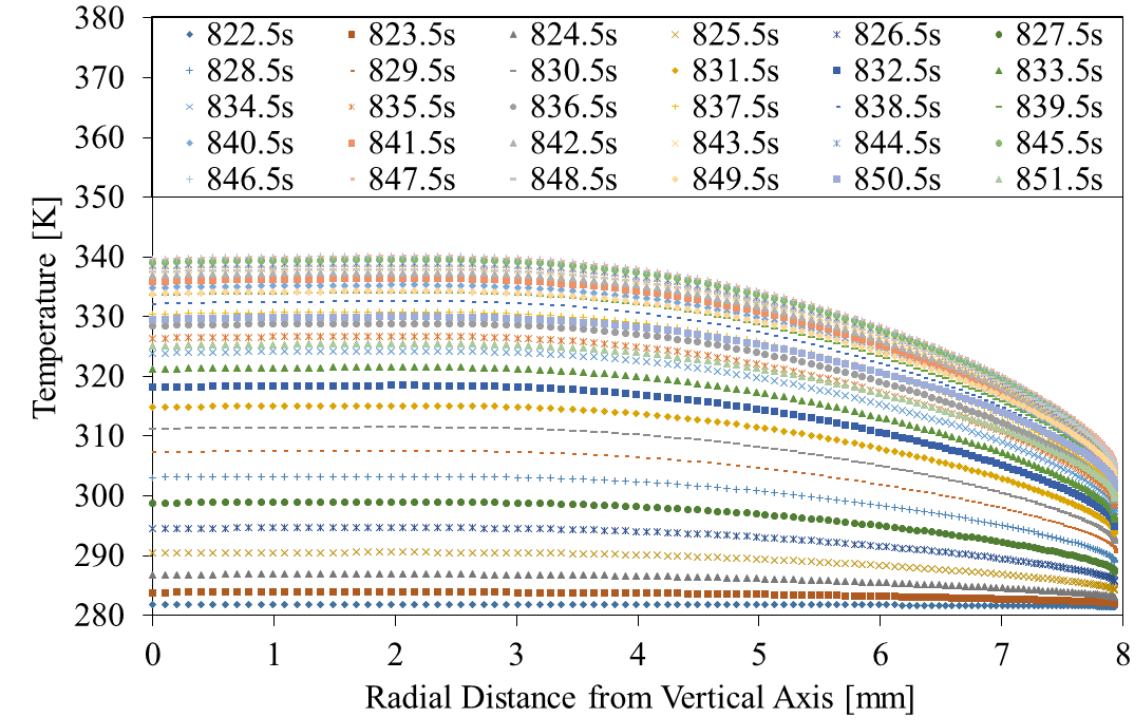

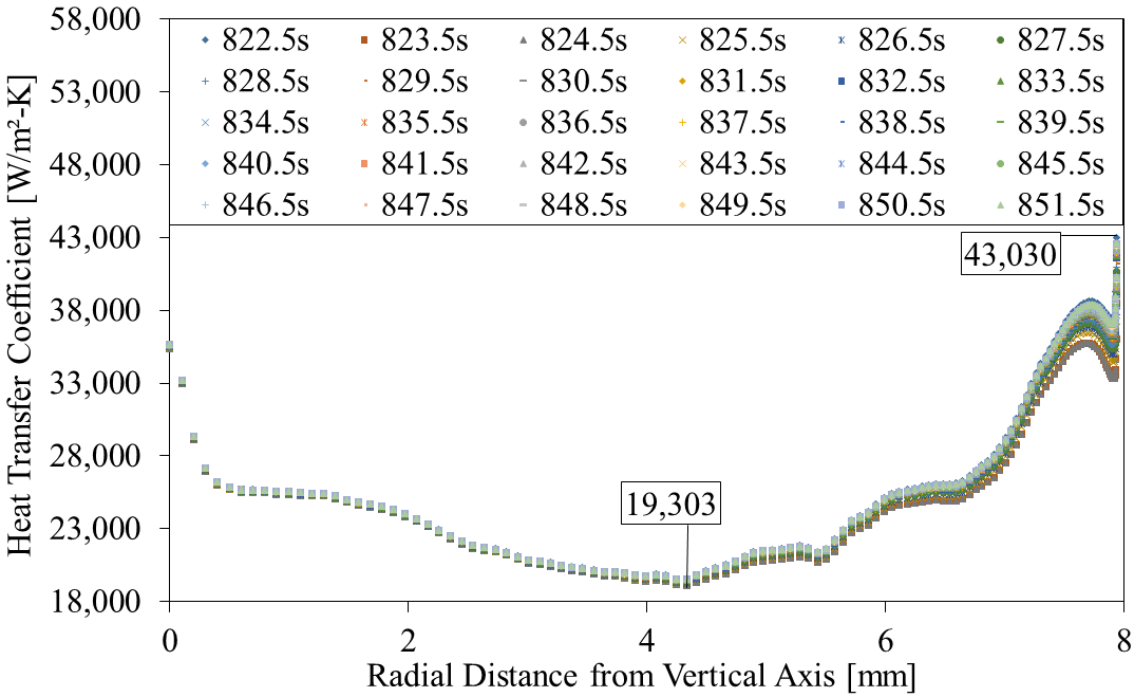

REFERENCES

[1] L. Schrattenholzer, A roadmap to a sustainable global energy system, *Proceedings of the International Energy Workshop*, Paris, June, 2004.

[2] ITER Organization. (2014) ITER.org. [Online]. http://www.iter.org

[3] W. M. Stacey, " *Fusion: An introduction to the physics and technology of magnetic confinement fusion*," John Wiley &Sons, 1984.

[4] T. Hirai, K. Ezato and P. Majerus, "ITER relevant high heat flux testing on plasmas facing surfaces," *Mater. Trans,* Vol. 46, pp. 412, 2005.

[5] A. S. Sabau, E. Ohriner, J. Kiggans, D. Harper, L. Snead and C. Schaich, "Facility for high-heat flux testing of irradiated fusion materials and components using infrared plasma arc lamps," *Physica Scripta*, T159, 2014.

[6] D. H. Wolf, F. P. Incropera and R. Viskanta, "Jet Impingement Boiling," *Advances in Heat Transfer* (Edited by J. P. Hartnett et al.), Vol. 23, pp. 1–132. Academic Press, New York, 1993.

[7] R.W. Bowring, "Physical model based on bubble detachment and calculation of steam voidage in the subcooled region of a heated channel," *OECD Halden Reactor Project Report HPR-10*, 1962.

[8] H. Miyazaki and E. Silberman, "Flow and heat transfer on a flat plate normal to a two-dimensional laminar jet issuing from a nozzle of finite height," *Int. J. Heat Mass Transfer,* Vol. 15, pp. 2097-2107, 1972.

[9] H. Martin, "Heat and mass transfer between impinging gas jets and solid surfaces," *Adv. Heat Transfer* (T. F. Irvine, Jr. and J. P. Hartnett, eds), Vol. 13, pp. 1-60, Academic Press, New York, 1977.

[10] S.J. Downs and E. H. James, "Jet impingement heat transfer - a literature survey," ASME Paper no. 87-HT-35, 1987.

[11] S. Polat, B. Huang, A. S. Mujumdar and W. J. Douglas, "Numerical flow and heat transfer under impinging jets: a review," *Annual Review of Numerical Fluid Mechanics and Heat Transfer* (C. L. Tien and T. C. Chawla, eds.), Vol. 2, pp. 157-197. Hemisphere, New York, 1989.

[12] D. T. Vader, F. P. Incropera and R. Viskanta, "Convection nucletae boiling on a heated surface cooled by an impinging, planar jet of water," *J. Heat Transfer*, Vol. 114, pp. 152-160, 1992.

[13] J. Kokado, N. Hatta, H. Takuda, J. Harada and N. Yasuhira, "An analysis of film boiling phenomena of subcooled water spreading radially on a hot steel plate," *Arch. Eisenhüttenwes*, Vol. 55, pp. 113-118, 1984.

[14] C. F. Ma and A. E. Bergles, "Jet impingement nucleate boiling," *Int. J. Heat Mass Transfer,* Vol. 29, pp. 1095-1101, 1986.

[15] H. Anglart, H., "Modelling of Vapour Generation at Wall in Subcooled Boiling Two-Phase Flow," *1st CFDS Int. User Conf.*, Eynsham Hall, Oxford, UK, 1993.

[16] H. Anglart, O. Nylund, N. Kurul, and M.Z. Podowski, "CFD prediction of flow and phase distribution in fuel assemblies with spacers". *NURETH-7*, Saratoga Springs, New York, 1995. Nucl. Eng. Des. 177, 215–228, 1997.

[17] Y. Katto and M. Kunihiro, "Study of the mechanism of burn-out in boiling system of high burn-out heat flux," *Bull. JSME,* Vol 16, pp. 1357-1366, 1973.

[18] C. F. Ma and A. E. Bergles, "Boiling jet impingement cooling of simulated microelectronic chips," In *Heat Transfer in Electronic Equipment* - 1983 (S. Oktay and A. Bar-Cohen, eds.), HTD. Vol. 28, pp. 5-12, 1983.

[19] M. Monde and Y. Katto, "Burn-out in a high heat-flux boiling system with an impinging jet," *Int. J. Heat Mass Transfe*r, Vol. 21, pp. 295-305, 1978.

[20] T. Kamata, S. Kumagai, and T, Takeyama, "Boiling heat transfer to an impinging jet spurted into a narrow space (Part I, space with an open end)," *Trans. JSME*, Vol 53B, pp. 183-187, 1988.

[21] T. Kamata, S. Kumagai, and T, Takeyama, "Boiling heat transfer to an impinging jet spurted into a narrow space (Part II, space with a limited end)," *Trans. JSME*, Vol 53B, pp. 188-192, 1988.

[22] T. Aihara, J. K. Kim, K. Suzuki and K. Kasahara, "Boiling heat transfer of a micro-impinging jet of liquid nitrogen in a very slender cryoprobe," *Int. J. Heat Mass Transfer*, Vol. 36, pp. 169-175, 1993.

[23] M. Ishimaru, J. K. Kim, T. Aihara and T. Shimoyama, "Boiling heat transfer characteristics due to a micro-impinging jet of LN_2," *Proceedings of the 28th National Heat Transfer Symposium of Japan*, pp. 730-732, 1991.

[24] A. Alajbegovic, N. Kurul, M. Z. Podowski, D. A. Drew, and R. T. Lahey, "A CFD Analysis of Multi-Dimensional Phenomena in Two-Phase Flow Using a Two-Fluid Model," *ANS Proc. of the 1996 National Heat Transfer Conference*, Houston, Texas, 1996.

[25] R. K. Škéma and A. A. Šlančiauskas, "Critical heat fluxes at jet-cooled flat surfaces," *Heat Transfer in Electronic and Microelectronic Equipment* (AA. E, Bergles, ed.), pp. 621-626, Hemisphere, New York, 1990.

[26] S. S. Kutateladze, *Heat Transfer in Condensation and Boiling*, U.S. AEC Report AEC-tr-3770, 1952.

[27] Y. Miyasaka, S. Inada and Y. Owase, "Critical heat flux and subcooled nucleate boiling in a transient region between a two-dimensional water jet and a heated surface," *J. Chem. Eng. Jpn.*, Vol. 13, pp. 29-35, 1980.

[28] D. G. Andrews and P. K. M. Rao, "Peak heat fluxes on thin horizontal ribbons in submerged water jets," *Can. J. Chem. Eng.*, Vol. 52, pp. 323-330, 1974.

[29] D. Wang, E. Yu and A. Przekwas, "A computational study of two phase jet impingement cooling of an electronic chip," *Fifteenth IEEE Semi-therm Symposium, IEEE*, pp. 10–15, 1999.

[30] N. Seiler, O. Simonin, S. Mimouni, P. Gardin and J.M. Seiler, "Modeling and computation of heat exchanges in the configuration of an impinging jet on a hot plate," *International Conference on Supercomputing in Nuclear Applications*, Paris, France, pp. 1–13, 2003.

[31] N. Kurul and M. Z. Podowski, "On the modeling of multidimensional effects in boiling channels," *Proceedings of the 27th National Heat Transfer Conference*, Minneapolis, Minnesota, USA, 1991.

[32] J. Lavieville, E. Quemerais, S. Mimouni, M. Boucker and N. Mechitoua, "NEPTUNE CFD V1.0 Theory Manual," *EDF*, 2005.

[33] N. Kurul, M.Z. Podowski, "Multidimensional effects in forced convection subcooled boiling," *Ninth International Heat Transfer Conference*, Jerusalem, Israel, 1-BO-04., pp. 21–26, 1990.

[34] R.M. Podowski, D.A. Drew, R.T.J. Lahey and M.Z. Podowski, "A mechanistic model of the ebullition cycle in forced convection subcooled boiling," *Eighth International Topical Meeting on Nuclear Reactor Thermal-Hydraulics*, Kyoto, Japan, Vol. 3, pp. 1535–1542, 1997.

[35] R. Cole, "A Photographic Study of Pool Boiling in the Region of the Critical Heat Flux ". *AlChE J*. 6. 533-542. 1960.

[36] V. H. Del Valle and D. B. R. Kenning, "Subcooled flow boiling at high heat flux," *International Journal of Heat and Mass Transfer*, Vol. 28, pp. 1907-1920, 1985.

[37] D.B.R. Kenning and H.T. Victor, "Fully-developed nucleate boiling: overlap of areas of influence and interference between bubble sites," *Int. J. Heat Mass Transfer*, Vol. 24, pp. 1025–1032, 1981.

[38] H.C. Unal, "Maximum bubble diameter, maximum bubble-growth time and bubble-growth rate during the subcooled nucleate flow boiling of water up to 17.7M N/m2," *Int. J. Heat Mass Transfer*, Vol. 19, pp. 643–649, 1976.

[39] M. Lemmert and L. M. Chawla, "Influence of flow velocity on surface boiling heat transfer coefficient," *Heat Transfer Boiling* (E. Hahne and U. Grigull, eds), Academic Press and Hemisphere, New York, NY, USA, 1977.

[40] R. M. Podowski, R. T. Lahey, D. A. Drew, and M. Z. Podowski, "Mechanistic Multidimensional Modeling of Forced-Convection Boiling Heat Transfer," *Proc. Eighth Int. Topical Meeting on Nuclear Reactor Thermal-Hydraulics (NURETH-8)*, Kyoto, Japan, vol.3, 1997.

[41] A.A. Troshko and Y.A. Hassan, "A two-equation turbulence model of turbulent bubbly flows," *Int. J. Multiphase Flow*, Vol. 27, pp.1965–2000, 2001.

[42] K.O. Pasamehmetoglu, "Numerical modeling of a nucleate boiling surface," *Numer. Heat Transfer Part A*, Vol. 25, pp. 703–719, 1994.

[43] S. Narumanchi, A. Troshko, D. Bharathan and V. Hassani, "Numerical simulations of nucleate boiling in impinging jets: Applications in power electronics cooling," *In ternational Journal of Heat and Mass Transfer*, Vol. 51, pp. 1-12, 2008.

[44] D.W. Zhou and C.F. Ma, "Local jet impingement boiling heat transfer with R113," *Heat Mass Transfer*, Vol. 40, pp. 539–549, 2004.

[45] A. S. Sabau, E. Ohriner, Y. Katoh and L. Snead, "High-heat flux testing using plasma arc of low-level irradiated materials," *Fusion Reactor Materials Program* DOE/ER-0313/52, Vol. 52, pp. 1-6, June 2012.

[46] A. S. Sabau, Private communications, November 21, 2013.

[47] A. S. Sabau, Private communications, April 3, 2014.

[48] (2014, June) FLUENT Theory Guide - 4. Turbulence. ANSYS 14.0 Help.

[49] Frank P. Incropera, David P. DeWitt, Theodore L. Bergman, and Adrienne S. Lavine, *Fundamentals of Heat and Mass Transfer*, 6th ed. United States of America: John Wiley & Sons, 2007.

[50] A. A. F. Tavasoli, J. W. Rensman, M. Schirra, and K. Shiba, "Material Design Data for Reduced Activation Martensitic Steel Type F82H," *Fusion Engineering and Design*, pp. 617-628, 2002.

[51] M. Z. Podowski, "Toward Mechanistic Modeling of Boiling Heat Transfer," *Nuclear Engineering and Technology*, vol. 44 (8), pp. 889-896, 2012.

[52] R. Zhang, T. Cong, W. Tian, S. Qiu, and G. Su, "Prediction of CHF in Vertical Heated Tubes Based on CFD Methodology," *Progress in Nuclear Energy*, vol. 78, pp. 196-200, 2014.

[53] Y. S. Touloukian, R. W. Powell, C. Y. Ho, and P. G. Klemens, *Thermophysical Properties of Matter Volume 1: Thermal Conductivity - Metallic Elements and Alloys,* United States of America: IFI/Plenum, 1970.

[54] Y. S. Touloukian and E. H. Buyco, *Thermophysical Properties of Matter - The TPRC Data Series -Volume 4: Specific Heat - Metallic Elements and Alloys,* United States of America: IFI/Plenum, 1971.

[55] Klein, S. A. *Engineering Equation Solver*. Computer software. *www.fchart.com*. Vers. 9.721. F-Chart Software, 15 Aug. 2013.

[56] M. Z. Podowski, "Multidimensional Modeling of Two-Phase Flow and Heat Transfer," *Int. Journal of Numerical Methods for Heat & Fluid Flow*, vol. 18, Issue 3/4, 2008.

[57] M. Z. Podowski and R. M. Podowski, "Mechanistic Multidimensional Modeling of Forced-Convection Boiling Heat Transfer," *Science and Technology of Nuclear Installations*, Article ID 387020.

[58] Z. Rouhani, "Void Measurements in The Regions of Subcooled Boiling and Low Quality Boiling," *AE-239*, 1966.

[59] G. G. Bartolomei and V. M. Chanturiya, "Experimental Study of True Void Fraction When Boiling Sucooled Water in Vertical Tubes," *Thermal Engineering*, vol. 14 (2), pp. 123-128, 1967.

[60] R. Hino and T. Ueda, "Studies on Heat Transfer and Flow Characteristics in Subcooled Flow Boiling - Part 1. Boiling Characteristics," *Int. J. Multiphase Flow*, vol. 11, pp. 269-281, 1985.

[61] P. Saha, "Thermally Induced Two-Phase Flow Instabilities, Including the Effect of Thermal Nonequelibrium Between the Phases," *PhD Thesis*, Georgia Institute of Technology, 1974.

[62] D. B. Spalding, "A General Purpose Computer Program for Multi-Dimensional One and Two-Phase Flow," *Mathematics and Computers in Simulation*, North Holland Press, vol. 23, 1981.

[63] G. C. Park, M. Z. Podowski, M. Becker and R. T. Lahey, "The Development of a Closed Form Analytical Model for the Stability Analysisof Nuclear-Coupled Density-Wave Oscillations in BWRs," *Nucl. Engr. & Design*, vol. 92, pp. 253-281, 1986.

VITA

Carlos H. Charry León was born in Bogota, Colombia on December 15, 1983 to Flor León and Luis Charry. After graduating from Centro Don Bosco High School in 1999, he attended the Georgia Institute of Technology and graduated in 2013 with Bachelor of Science degree in Nuclear and Radiological Engineering (highest honors). He then continued at Georgia Institute of Technology in 2013, where he began pursuing a master's degree in Mechanical Engineering.

This thesis was typed by Carlos H. Charry León